UNIVERSITY OF CALIFORNIA, SAN DIEGO

Cyclotron Line and Wind studies of Galactic High Mass X-ray Binaries

A dissertation submitted in partial satisfaction of the
requirements for the degree
Doctor of Philosophy

in

Physics

by

Slawomir Suchy

Committee in charge:

Richard E. Rothschild, Chair
George M. Fuller
Kurt Marti
Hans Paar
Katja Pottschmidt
Kevin Quest

2011

The dissertation of Slawomir Suchy is approved, and it is acceptable in quality and form for publication on microfilm and electronically:

_____

_____

_____

_____

_____

_____
Chair

University of California, San Diego

2011

DEDICATION

To my parents

TABLE OF CONTENTS

ACKNOWLEDGEMENTS

First of all I want to thank my advisor Richard E. Rothschild for his support and his guidance in this work. He always came up with the wildest ideas and very good questions, challenging me to push myself forward. A very big thank you also to Katja Pottschmidt and Jörn Wilms, who always were available when my program crashed or something else didn't work out, and who never spared a marker on my paper drafts. Also a big thanks to Liz Rivers, Paul Hemphil, Alex Markowitz, and Mirko Krumpe from the X-ray group at CASS, who always were there when I ran into programing or english problems.

I want to thank mom and stepdad, who always believed in me and pushed me forward when I was near to give up. My dad and stepmom for the great time I always have when visiting them and for all of their support. A very special thanks to my soon to be wife, Sarah, who supported me throughout the last year and always was there for me, especially in the last few months. And to Kira, who is one of the best trained Labradors I know, and who always had a kiss for me when I felt sad or overwhelmed.

I would like to thank the people at CASS. Dana Johnson, who always was there when I had a question about the university proceedings. Tom Gasaway, who always was available helping me with some programming issues or just simply to talk. Ron Quillin, the Jack of all Trades and always there when you needed something soldered or taken apart. Paul Yeatman, who was always there in the first few years when our computer misbehaved. Pete James, who kept the computers running. Fred Duttweiler, who never stressed out about anything, and George Huszar, who always had a nice word and/or a small snack for the late hours at work.

A special thanks goes to the gang at the 3 o'clock tea time, especially Wendell Misch, Marc Rafelski, JJ Cherry, Liz Rivers, George Fuller, Kim Greist, and Tom Murphy. Tea time was always a great platform to exchange news and theories, and sometime the one or other physics problem.

A very big thank you for the people in Bamberg and Tübingen, where I always felt welcome and who were amazing when I was visiting. A special thanks

from this group goes to Victoria Grinberg (the sister I never had) and Felix Fürst (the best sailing buddy I had) some of the best flat mates I had in my time here.

A big thank you also for the Wednesday evening Magic: The Gathering playgroup: Wendell, Ian, Liz, Nathan, Nick, and Hao. It was great to come back into the game and find such a great gaming group to bounce Ideas off.

Chapter 4 is a reprint of the published publication: Suchy, Slawomir; Pottschmidt, Katja; Wilms, Jrn; Kreykenbohm, Ingo; Schnherr, Gabriele; Kretschmar, Peter; McBride, Vanessa; Caballero, Isabel; Rothschild, Richard E.; Grinberg, Victoria, "Pulse Phase-resolved Analysis of the High-Mass X-Ray Binary Centaurus X-3 over Two Binary Orbits ", The Astrophysical Journal, 2008, 675, 1478.

Chapter 5 is a reprint of the published publication: Suchy, Slawomir; Pottschmidt, Katja; Rothschild, Richard E.; Wilms, Jrn; Frst, Felix; Barragan, Laura; Caballero, Isabel; Grinberg, Victoria; Kreykenbohm, Ingo; Doroshenko, Victor; Santangelo, Andrea; Staubert, Rdiger; Terada, Yukikatsu; Iwakari, Wataru; Makishima, Kazuo, "Suzaku Observations of the HMXB 1A 1118-61", The Astrophysical Journal, 2011, Vol. 733, 15

The material in Chapter 6 was accepted for publication in the following publication: Suchy, Slawomir; Fuerst, Felix; Pottschmidt, Katja; Caballero, Isabel; Kreykenbohm, Ingo; Wilms, Joern; Markowitz, Alex; Rothschild, Richard E.,"Broadband spectroscopy using two Suzaku observation of the HMXB GX 301-2", The Astrophysical Journal, 2011, accepted.

VITA

2011	PhD University of California, San Diego (USA)
2009	C.Phii University of California, San Diego (USA)
2008	M.Sci. University of California, San Diego (USA)
2004	Dipl. Phys. University of Tübingen (Germany)

PUBLICATIONS

DeCesar, M.E., Boyd, P.T., Pottschmidt, K., Wilms, J., **Suchy, S.**, Miller, M.C., 2010, ***"The Be/X-ray binary Swift J1626−5156 as a cyclotron line source"***, Ap. J., in prep.

Martin-Carillo, A., Kirsch, M.G.F., Caballero, I., Freyberg, M.J., Ibarra, A., Kendziorra, E., Lammers, U., Mukerjee, K, Schönherr, G., Stuhlinger, M., Saxton, R.D., Staubert, R., **Suchy, S.**, Wellbrock, A., Webb, N., Guainazzi, M., ***"The relative and absolute timing accuracy of the pn-camera on XMM-Newton, from X-ray pulsations of the Crab and other pulsars"***, 2011, A&A, submitted

Suchy, S., Fürst, F., Pottschmidt, K., Caballero, I., Kreykenbohm, I., Wilms, J., Marko-witz, A., Rothschild, R.E. ***"Broadband spectroscopy using two Suzaku observations of the HMXB GX 301−2 "***, 2011, ApJ, accepted

Fürst, F., **Suchy, S.**, Kreykenbohm, I., Barragan, L., Wilms, J., Pottschmidt, K., Caballero, I., Kretschmar, P., Ferrigno, C., Rothschild, R. E. ***"Study of the many fluorescent lines and the absorption variability in GX 301-2 with XMM-Newton"***, A&A, 535, 9

Böck, M., Grinberg, V., Pottschmidt, K., Hanke, M., Nowak, M. A., Markoff, S. B., Uttley, P., Rodriguez, J., Pooley, G. G., **Suchy**, S., Rothschild, R. E., Wilms, J. ***"Spectro-timing analysis of Cygnus X-1 during a fast state transition"***, A&A, 533, 8

Rothschild, R. E., Markowitz, A., Rivers, E., **Suchy**, S., Pottschmidt, K., Kadler, M., Müller, C., Wilms, J., 2011, ***"Twelve and a Half Years of Observations of Centaurus a with the Rossi X-Ray Timing Explorer"***, Ap.J., 733, 23

Suchy, S., Pottschmidt, K., Rothschild, R.E., Wilms, J., Barragan, L., Caballero, I., Grinberg, V., Fürst, F., Kreykenbohm, I., Doroshenko, V., Santangelo, A., Staubert, R., Terada, Y., Iwakari, W., Makashima, K., 2010, ***"Suzaku observations of the HMXB 1A 1118−61"***, Ap.J., 733, 15

Staubert, R., Pottschmidt, K., Doroshenko, V., Wilms, J., **Suchy, S.**, Rothschild, R., Santangelo, A., ***"Finding a 24-day orbital period for the X-ray binary 1A 1118-616"***, 2011, A&A, 527, 7

Fürst, F., Kreykenbohm, I., **Suchy, S.**, Barragan, L., Wilms, J., Rothschild, R. E., Pottschmidt, K. ***"4U 1909+07: a well-hidden pearl"***, 2011, A&A, 525, 73

Doroshenko, V., **Suchy, S.**, Santangelo, A., Staubert, R., Kreykenbohm, I., Rothschild, R., Pottschmidt, K., Wilms, J., 2010, ***"RXTE observations of the 1A 1118−61 in an outburst, and the discovery of a cyclotron line"***, A&A, 515, L1

Rivers, E., Markowitz, A., Pottschmidt, K., Roth, S., Barragan, L., Fürst, F., **Suchy, S.**, Kreykenbohm, I., Wilms, J., Rothschild, R.E., 2010, ***"A comprehensive spectral analysis of the X-ray pulsar 4U 1907+09 from two observations with the Suzaku X-ray observatory"***, Ap. J., 709, 179

Suchy, S., Pottschmidt, K., Wilms, J., Kreykenbohm, I., Schönherr, G., Kretschmar, P., McBride, V., Caballero, I., Rothschild, R.E., Grinberg, V., 2008, ***"Pulse phase resolved analysis of the high mass X-ray binary Centaurus X-3 over two binary orbits"***, Ap. J., 675, 1487

Caballero, I., Santangelo, A., Kretschmar, P., Staubert, R., Postnov, K., Klochkov, D., Camero-Arranz, A., Finger, M.H., Kreykenbohm, I., Pottschmidt, K., Rothschild, R.E., **Suchy, S.**, Wilms, J., Wilson, C.A., 2008, ***"The pre-outburst flare of A 0535+262 during the August/September 2005 outburst"***, A&A, 480, L17

Caballero, I., Kretschmar, P., Santangelo, A., Staubert, R., Camero, A., Ferrigno, C., Klochkov, D., Kreykenbohm, I., Pottschmidt, K., Rothschild, R.E., Segreto, A., **Suchy, S.**, Wilms, J., 2007, ***"1A 0535+262 in the August/September 2005 outburst observed by RXTE and INTEGRAL"***, A&A, 465, L21

Pottschmidt, K., Kreykenbohm, I., Wilms, J., Coburn, W., Rothschild, R.E., Kretschmar, P., McBride, V., **Suchy, S.**, Staubert, R., 2005, ***"RXTE Discovery of Multiple Cyclotron Lines During the 2004 December Outburst of V 0332+53"***, Ap. J. Lett., 634, L97

PROCEEDINGS, PROPOSALS, ETC.

Kreykenbohm, I, Fürst, F., Kühnel, M., Müller, S., Barragan, L., Wilms, J., Pottschmidt, K., **Suchy, S.**, Rothschild, R. E. ***"A scarcely known accreting X-ray pulsar"***, AIPC, 1379, 111

Caballero, I., Kretschmar, P., Pottschmidt, K., Santangelo, A., Wilms, J., Kreykenbohm, I., Ferrigno, C., **Suchy, S.**, Rothschild, R., Finger, M., Postnov, K., McBride, V., Domingo, A., Schönherr, G., Klochkov, D., Staubert, R., Camero-Arranz, A., 2010 ***"New outburst of A 0535+26 observed with INTEGRAL and RXTE"***, AIPC, 1248, 147

Schönherr, G., Wilms, J., Kretschmar, P., Kreykenbohm, I., Pottschmidt, K., **Suchy, S.**, Caballero, I., Rothschild, R., Santangelo, A., Staubert, R., 2010, ***"The Magnetic Field of Neutron Stars: What Can Cyclotron Lines Tell Us?"***, AIPC, 1248, 67

Kretschmar, P., Kreykenbom, I., Wilms, J., Hanke, M., Stuhlinger, M., Pollock A. M. T., Staubert, R., Kendziorra, E., Rothschild, R., **Suchy, S.**, 2008, ***"Scanning the Egress of Vela X−1"***, 7th INTEGRAL Workshop, 120

Suchy, S., Pelling, M.R.,Tomsick, J.A., Matteson, J.L., Rothschild, R.E., 2006, ***"Laboratory testing of the HEXIS hard X-ray imager balloon telescope"***, SPIE, 6266, 65

Rothschild, R.E., Tomsick, J.A., Matteson, J.L., Pelling, M.R., **Suchy, S.**, 2006, ***"CZT Detector and HXI development at CASS/ UCSD"***, AIPC, 840, 107

Kendziorra, E., Schanz, T., **Suchy, S.**, Distratis, G., 2006, ***"Event pre processor for the CZT detector on MIRAX"*** AIPC, 840, 117

Suchy, S., Schanz, T., Kendziorra, E., Distratis, G., Heindl, W.A., Wilms, J., Braga, J., Santiago, V., Staubert, R., Rothschild, R.E., 2004, ***"Event pre processor for the CdZnTe-strip detector on MIRAX"***, SPIE, 5501, 312

ABSTRACT OF THE DISSERTATION

Cyclotron Line and Wind studies of Galactic High Mass X-ray Binaries

by

Slawomir Suchy

Doctor of Philosophy in Physics

University of California, San Diego, 2011

Richard E. Rothschild, Chair

High mass X-ray binaries are rotating neutron stars with very strong magnetic fields that channel accreting matter from their companion star onto the magnetic poles with subsequent collimated X-ray emission. The stars are fed either by a strong stellar wind of the optical companion or by an accretion disk, where material follows the magnetic field lines, emitting X-rays throughout this process either in the accretion column or directly from the neutron star surface. The fast rotation and the narrow collimation of the X-ray emission creates an observed pulsation, forming the concept of a pulsar. Some of the key questions of these thesis are the emission processes above the magnetic pole, including the influence of the magnetic field, the formation of the X-ray beam, and the structure of the stellar

wind. An important process is the effect of the teraGauss magnetic field. Cyclotron resonance scattering creates spectral features similar to broad absorption lines (CRSFs or cyclotron lines) that are directly related to the magnetic field. The discovery of cyclotron lines ~ 35 years ago allowes for the only direct method to measure the magnetic field strength in neutron star systems. Variations in the line parameters throughout the pulse phase, and a dependence in the observed luminosity can also aid in the understanding of these processes.

In this thesis I present the results of phase averaged and phase resolved analysis of the three high mass X-ray binaries Cen X-3, 1A 1118−61, and GX 301−2. The data used for this work were obtained with NASA's *Rossi X-ray Timing Explorer* and the Japanese *Suzaku* mission. Both satellites are ideal to cover the broad energy band, where CRSFs occur and are necessary for understanding the continuum as a whole. In the process of investigating the 3 sources, I discovered a CRSF at ~ 55 keV in the transient binary 1A 1118−61, which indicates one of the strongest magnetic fields known in these objects. I used the variations of the CRSF in GX 301−2 throughout its pulse phase to develop a simple dipole model of the relationship between the magnetic moment vector and the spin axis of the neutron star. In Cen X-3 I use a similar model to demonstrate that the magnetic field most likely includes higher orders than just the simple dipole.

The use of a wind model in high mass X-ray binaries can give information about the type of accretion, disk or wind, and the structure of the wind by measuring the amount of the material in the line of sight versus orbital phase. In Cen X-3, I used a simple spherical wind model throughout the two binary orbits and found that the observed absorption column densities are not consistent with pure wind accretion, and that either an accretion wake or a disk are needed to be consistent with the data. Similar results were observed in GX 301−2, where the neutron star may have passed through an accretion stream, increasing the observed amount of absorbed material.

Chapter 1

Introduction

Astronomy is one of the oldest sciences in human history, stretching from ancient Egypt and possibly earlier, to the modern ages. With an age of only ~ 50 years, X-ray astronomy, however, is one of the younger divisions in the very diverse field of modern astronomy.

X-rays are produced in extreme environments of galactic and extragalactic objects and can be used to study the conditions and behavior of matter in these environments. This dissertation is a study of behavior of matter close to neutron stars, where these extreme conditions, i.e., large magnetic fields (B 10^{12} G), high temperatures, strong gravitation, and intense radiation, occur. In this work, I used data obtained by two X-ray satellites, NASA's *Rossi X-ray Timing Explorer (RXTE)* and the Japanese/US mission *Suzaku* (also known as *Astro E-2*), to study the continuum originating from high mass X-ray binaries (HMXBs), containing X-ray pulsars for different luminosities and states. In particular, I studied the cyclotron resonance scattering feature (CRSF) in rotating neutron stars, which allows us to learn about magnetic fields as well as the production and transport of radiation in these extreme regions.

1.1 Brief history of X-ray astronomy

X-rays are produced in extremely hot gases, where the temperature reaches millions of degrees. In 1948, Thomas Burnight discovered X-ray radiation from

the Sun using a high altitude balloon (see Keller, 1995, for historical review). Ricardo Giacconi discovered the first extrasolar X-ray source in Scorpius, Sco X-1, 14 years later, in the attempt to measure fluorescence X-rays produced on the moon surface (Giacconi et al., 1962). The discovery of sources outside of the solar systems producing X-rays opened up a new field, adding a new energy band to study stars and galaxies: X-ray astronomy was born.

Since the earth's atmosphere is opaque to X-rays, the first discoveries were performed with high altitude balloons and sounding rockets, which transported the instruments to the upper parts of the atmosphere. These methods only allow for very short observation times of a few minutes to a few hours, and cover only small parts of the sky. The first dedicated X-ray satellite, *UHURU*, was launched in 1970 (Giacconi et al., 1971b) and discovered over 300 unique X-ray sources, providing the first X-ray catalog of the sky (Forman et al., 1978). The first all sky survey was performed by the High Energy Astronomy Observatory (HEAO-1) in the 0.2 keV-10 MeV energy band, resulting in the measurement of the X-ray background in the 3-50 keV energy band (Marshall et al., 1980). The next big step was the *HEAO-2* mission (also called *Einstein*), which was launched in 1978 (Giacconi et al., 1979). This mission provided the first X-ray imaging capabilities and allowed a detailed study of extended sources, such as supernova remnants and X-ray jets in galaxies. The German *Röntgensatellit (ROSAT)* was launched in 1990 (Trümper, 1982) and created the first in-depth low energy all sky survey in the 1-2 keV energy range, resulting in the discovery of over 120,000 new sources. Up to this day, it is one of the most complete surveys in the $0.1 - 2$ keV energy range. In late 1995, the *RXTE* mission was launched, followed in 1996 by *BeppoSAX*. Both X-ray astronomy missions had broad band spectral coverage from ~ 1 to over 100 keV, with very good timing resolution in the case of *RXTE* and excellent low energy sensitivity for *BeppoSAX*. These missions detected Gamma Ray Burst afterglows and discovered kilohertz quasi-periodic oscillations in black holes and low mass X-ray binaries (LMXBs). In addition they observed transient pulsars over a broad range of luminosities, helping to understand accretion theories.

In 1999, two large instruments, the US *Chandra* X-ray observatory (Weis-

skopf et al., 2000) and the European Xray Multi-Mirror Mission *XMM-Newton* (Jansen & Parmar, 2001), were launched. Both satellites provided unprecedented imaging capabilities and high resolution spectroscopy, where *Chandra* achieves sub-arcsecond spatial resolution and *XMM-Newton* has a larger photon collecting area, enabling deep observations of faint and distance sources. In 2002 the *INTErnational Gamma-Ray Astrophysics Laboratory* (*INTEGRAL*) was launched (Winkler et al., 2003). The coded mask instruments onboard *INTEGRAL* provide a very large field of view, allowing monitoring of multiple sources at the same time, while sacrificing sensitivity due to high background counting rates. With the large energy range of $\sim 3\,\mathrm{keV}$ up to $10\,\mathrm{MeV}$ for the combination of all instruments, it is an excellent mission for monitoring individual bright X-ray sources. In December 2004, the US launched the *Swift Gamma-Ray Burst Mission* (Gehrels et al., 2004) to study gamma-ray bursts and their afterglows. With the large Burst Alert Telescope (BAT), *Swift* can cover $\sim 1/6$ of the sky at once, detect bursts and point the satellite for follow up observations with the two other instruments. In addition, the position of a detected burst is relayed to the ground and can be used in follow up observations with ground based telescopes. The Japanese *Suzaku* satellite (Mitsuda et al., 2007), was launched in 2005. Onboard was the first space X-ray micro-calorimeter (XRS), which would have allowed an unprecedented energy resolution in the soft X-ray band. Unfortunately the XRS cooling system failed shortly after the launch and no scientific data could be gathered. Nevertheless, the two remaining instruments perform excellent observations and are discussed later in this work. The *Fermi Gamma-Ray Space Telescope* (Ritz, 2007) was launched in June 2008 and consists of two instruments, the large area telescope (LAT) to study the flux from high energy cosmic Gamma-Rays and the Gamma Ray Burst Monitor (GBM) to study Gamma-Ray bursts. With its very large field of view, both instruments can monitor a large portion of the sky throughout one day.

The two satellites used in this thesis, *RXTE* and *Suzaku* will be introduced in more detail in chapter 2.

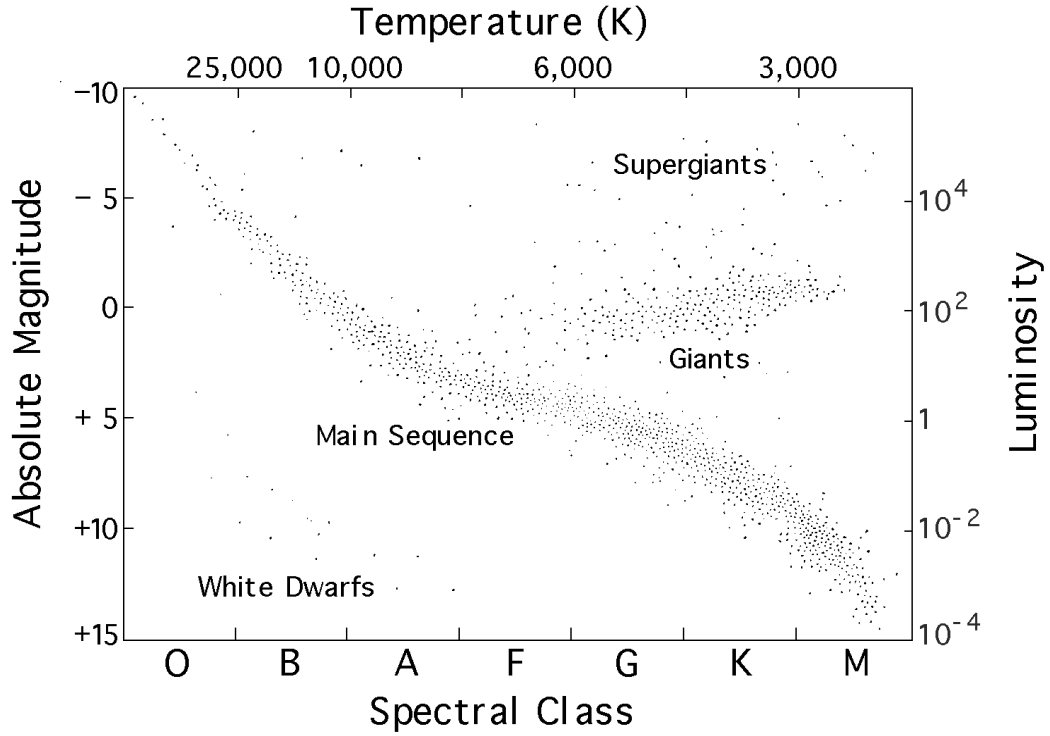

Figure 1.1 The Hertzsprung-Russel diagram showing the temperature and luminosity distribution of different stars. The main sequence is the region where a star is in hydrostatic equilibrium and spends the majority of its lifetime. From the "Live from *RXTE* Project" website[1].

1.2 Stellar evolution

To study the physical conditions in an accreting binary, it is necessary to understand the origin of such systems. This sections summarizes the evolution of single and binary stars and describes especially the difference in their evolutionary end stage.

1.2.1 Isolated stars

In its life cycle of millions to billions of years, an isolated star evolves through many different stages. Progenitors, or so-called protostars, are formed in high density regions of interstellar medium or in molecular clouds. Nearby supernova explosions of older stars may supply these regions with additional material

which can trigger a gravitational collapse of the region, forming a protostar. The protostar continues to accrete the surrounding material for $\sim 10^{5-7}$ years, heating up during this process, until the temperature of the system is high enough so that the thermal radiation pressure stops the accretion process. The protostar collapses further until the temperature in its core reaches $\sim 10^7\,\mathrm{K}$ and the density is high enough to enable fusion of hydrogen to helium, releasing a large amount of energy. The increased radiation from the core dissipates the dust in the outer layers and a new star is born.

The evolution of a star can be visualized in a Herzsprung-Russel (H-R) diagram (Hertzsprung, 1911; Rosenberg, 1910), which shows the distribution of the absolute visual magnitude of a star over its temperature (Fig. 1.1). Most stars spend the majority of their lifetime on a diagonal line in the H-R diagram, the so-called main sequence, where they are in hydrostatic equilibrium. A star of about one solar mass ($M_\odot$) spends $\sim$ 10 billion years on the main sequence. During this time, which corresponds to the hydrogen nuclear burning phase, their temperature and luminosity do not change significantly and the star evolves only little. This phase is significantly shorter for stars with larger mass, where due to higher temperatures in the stellar interior, the fusion process is accelerated. When the hydrogen of the fusion process is depleted, the star reaches the end of this nuclear burning phase, and the radiation pressure in its core declines. The core of the star contracts. The hydrogen continues to burn in an outer layer, whereas the pressure and temperature in the collapsing core increase. For heavier stars, i.e., where the inner core reaches a temperature of $\sim 10^8\,\mathrm{K}$, the helium in the inner core ignites and starts a second nuclear burning process, where the helium burns into carbon and oxygen (Ray, 2004). The increased pressure from the helium burning in the core expands the outer hydrogen shell of the star, decreasing the surface luminosity and transforming the star into a Red Giant. During this process the star leaves hydrostatic equilibrium and moves on the Giant branch in the H-R diagram. Depending on the mass of the collapsing core, different scenarios can occur for the evolving star. Figure 1.2 shows the evolutionary tracks for theoretical model stars of different masses:

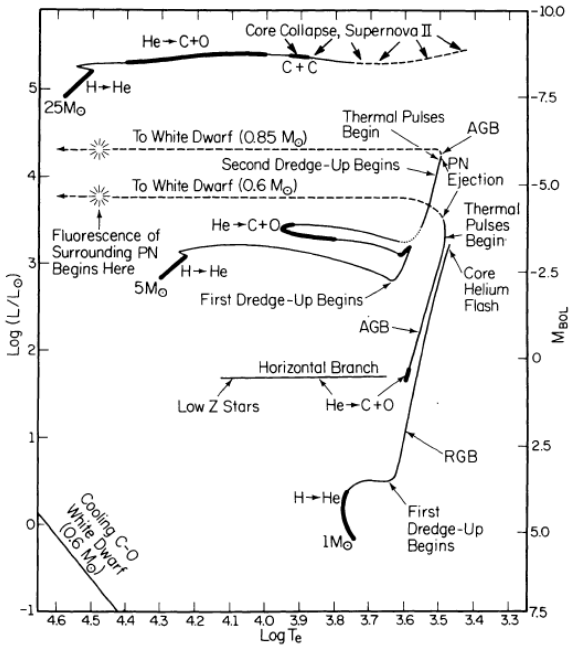

Figure 1.2 Tracks in the Hertzsprung-Russel diagram for theoretical models of stars with a mass of $1\,M_\odot$, $5\,M_\odot$, and $25\,M_\odot$ after they left the main sequence. From Iben (1991)

- For a low mass star, $< 1.4\,M_\odot$ the core collapses until a density of $\rho \sim 10^6\,\mathrm{g\,cm^{-3}}$ is reached. At this density the electron gas becomes degenerate and ignites the created helium throughout the core all at once. The star ejects its outer layer in a Helium-Flash leaving a core mass of $\sim 0.5\,M_\odot$ behind. The collapse of the remaining mass continues until electron degeneracy is able to counteract the gravity and a white dwarf is formed. A white dwarf is the hot remainder of a low mass star, where the fusion process has stopped and the star is only supported by the electron degeneracy pressure.

- A star with a mass of $2 - 5\,M_\odot$ is large enough to ignite continuous helium burning to create a carbon-oxygen core, but is not massive enough to start carbon burning in its core. The hydrogen shell continues to burn and expands to form a Red Giant. The helium burning process is very unstable and goes through a series of heating and cooling events, where the emitted energy ejects part of the outer hydrogen and helium shell. These events form a planetary nebula around the center of the remaining carbon-oxygen white

dwarf.

- For large initial stellar mass ($\sim 25\,M_{\odot}$) the carbon-oxygen core will be dense and hot enough to ignite. The burning core produces heavier elements which continue to collapse. For high enough temperatures and densities, this fusion process continues until the core consists mostly of iron. If the gravitational pressure of the core exceeds the degenerate electron pressure, the electrons are "pressed" into the protons (inverse β decay) and the electron pressure decreases. This sudden collapse of the core releases large amount of energy on a very short time scale, creating a supernova, where the outer layers of the star are mostly ejected and the remains of the core are massive enough to collapse to a neutron star or a black hole.

1.2.2 Binary systems

Of all the stars in the Milky Way only 2/3 are classified as single stars (Lada, 2006), leaving $\sim 1/3$ of all systems to multiple star systems, where two or more stars orbit a common center of mass. Although the evolution of the individual stars in such a system is up to a point very similar to the evolution of an isolated star, the introduction of a second massive object does increase the complexity of the system.

Mass transfer from one star to the other and tidal heating, where the radiation of one star heats the surface of his companion, make theoretical modeling much more complicated than the simple spherical model of an isolated star. To discuss matter transfer within a binary system, the gravitational potential of both bodies has to be taken into consideration. In the co-rotating frame such a potential can be described as:

$$\Phi(r) = -\frac{GM_1}{\vec{r}-\vec{r_1}} - \frac{GM_2}{\vec{r}-\vec{r_2}} - \frac{1}{2}(\vec{\omega}\times\vec{r})^2 \tag{1.1}$$

This potential includes the two stellar masses M_1 and M_2, the two positions of the stars $\vec{r_1}$ and $\vec{r_2}$, and the position, $\vec{r}$, at which the field is calculated. In addition, the angular velocity, ω, describes the rotation of the system and G is the Gravitational constant. Figure 1.3 shows a three-dimensional representation of such a potential,

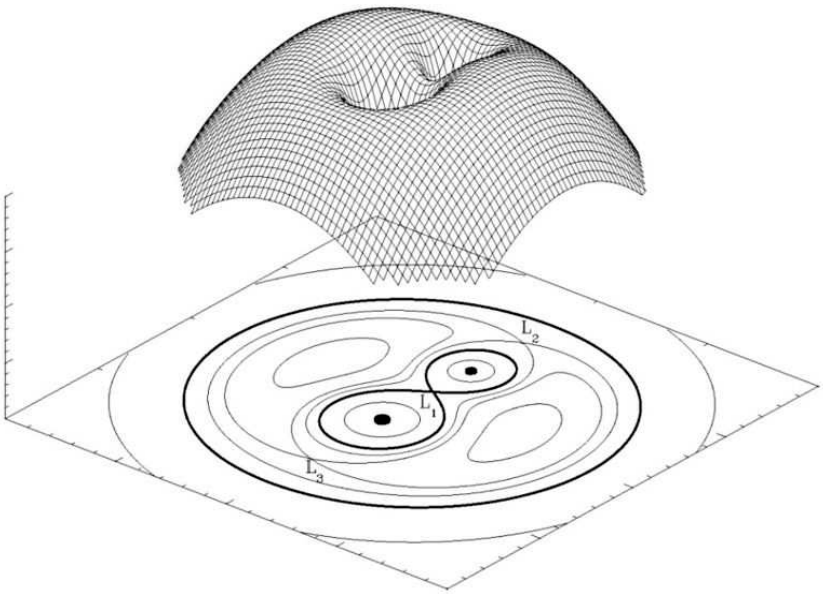

Figure 1.3 Roche Potential for a binary system with two different masses. The projection shows the equipotential lines and three of the five Lagrange points are marked. Matter beyond the Roche Surface (the bold line trough L1) is not gravitationally bound to one specific star and can be easily accreted.

where the equipotential contours are projected onto a plane. The bold line in the projection of the potential lines indicates the Roche surface, the innermost equipotential surface that is shared by both stars. The Roche surface goes through the first of five so-called Lagrange points, which are semi-stable positions in the potential well where gravitational forces nullify each other and where a body can stay for long periods of time if not disturbed. These Lagrange points can be found in all two body systems, e.g., the Sun-Earth system, and are therefore of special interest to position satellites in quasi-stable orbits.

Stars in binary systems have different stellar masses and where the primary star, defined by its higher mass, will evolve faster. When the primary star reaches the Red Giant phase, it expands until it reaches the Roche surface, which limits the size of the star. If the star evolves beyond the Roche lobe into a common envelope phase, its stellar material is not gravitationally bound and can either drift away or be accreted onto the less massive secondary star, which accelerates the evolution of the secondary star. Depending on the evolutionary phase and the remaining

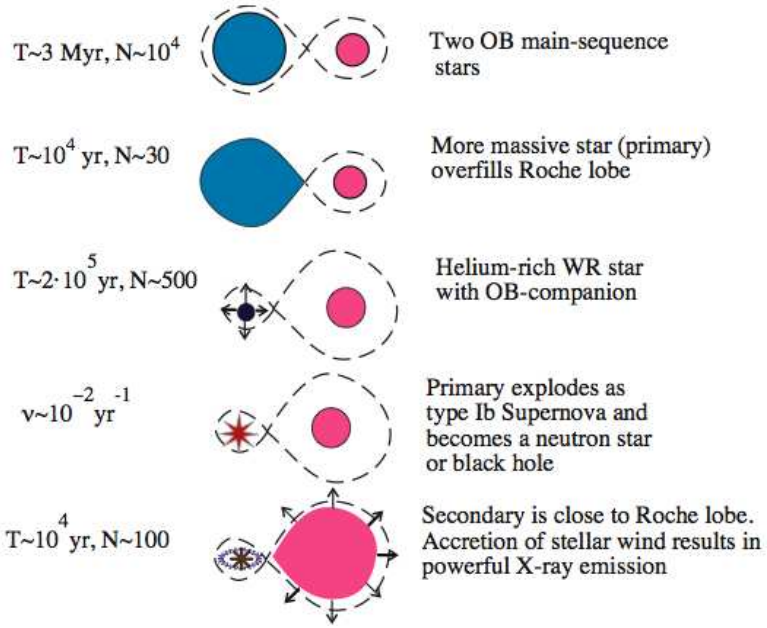

Figure 1.4 Formation of a compact object in a binary system. T indicates the average time spent in a specific phase. ν is the frequency of supernova events in our galaxy. N is the approximate numbers of binaries in this phase in our Galaxy. Based on Postnov & Yungelson (2006)

mass of the primary star, different scenarios can occur:

For a low mass binary system, the primary star expands beyond its Roche surface and transfers the outer layers onto the secondary star. The remaining core of the primary star evolves into an Oxygen/Neon white dwarf, a Helium white dwarf, or a Hydrogen white dwarf (Iben & Tutukov, 1985), depending on how massive the star was initially and how much of its outer layer was lost.

For higher mass binary systems ($> 25M_{\odot}$), the evolution occurs more violently (Figure 1.4): the bigger primary star, can lose a large portion of its mass due to Roche lobe overflow. When the outer envelope is transfered to the secondary star, the star shrinks below the size of the Roche surface and the mass transfer stops. The primary star evolves further with its remaining mass, and if massive enough, can explode in a supernova, leaving a compact object, either a neutron star or a black hole, behind. Such a supernova explosion can result in a very eccentric orbit of the neutron star, as observed in Be binary systems. The secondary star, which is now the more massive of the two, evolves faster and expands until it

reaches the Roche surface. Matter will now transfer from the secondary star onto the compact object via Roche lobe overflow or via wind accretion, depending on the strength of the winds in the secondary star (see below).

A special branch in binary star evolution is the creation of cataclysmic variables (CVs). For a very close binary system, tidal forces between the two stellar objects can create a locked rotation between the primary and secondary star. The primary star evolves as described above, creating a white dwarf, with a mass below the Chandrasekhar limit of $1.4\,M_{\odot}$. The secondary star will fill its Roche surface while retaining hydrogen in its core, and transfers material, which consists mostly of hydrogen, onto the primary star (Iben, 1991). The accreted material accumulates on the white dwarf surface and, for sufficient density and temperature, the hydrogen layer is ignited, rapidly burning the hydrogen into helium. If the accretion process pushes the primary mass over the Chandrasekhar limit, the ignition can trigger a runaway carbon burning which results in a type I supernova explosion (Starrfield et al., 1985), destroying the white dwarf. A detailed discussion of cataclysmic variables can be found in Córdova (1995) and Iben (1991).

1.2.3 Pulsars

The existence of neutron stars was first proposed by Baade & Zwicky (1934) who predicted that the gravitational binding energy of a star would be sufficient to power a supernova, transforming parts of its collapsing core mass into energy and ejecting the outer layers. The remaining core matter would then condense to form a compact object, the neutron star.

In 1967, Jocelyn Bell and Anthony Hewish discovered regular radio pulses with a period of 1.33 s when observing the source CP 1919 (Hewish et al., 1968). At first, this discovery was believed to be of artificial origin and the source was even called LGM−1 ("Little Green Men") for a brief period of time. With the discovery of multiple pulsating sources with different periods, the idea that these sources were artificial was quickly discarded. It became clear that the pulsations were consistent with the rotation period of these objects, making neutron stars

the most likely objects. A few years later, Giacconi et al. (1971b) discovered X-ray pulsations at 4.8 s in Cen X-3, showing that compact objects in X-ray binary systems show pulsations.

With a radius of $\sim 10\,\mathrm{km}$, a neutron star is significantly smaller than its progenitor but still holds a majority of its original angular momentum. This implies a very high initial angular velocity of the neutron star, resulting in pulse periods between multiple hundreds of seconds and down to 1 ms.

The observed pulsations are caused by the directed emission from ionized material falling along the magnetic field lines onto the magnetic poles of the neutron star (binary pulsars Taylor, 1981) or by an intense magnetic dipole radiation, due to a misalignment of the magnetic field and the rotation axis (radio pulsars, Pacini, 1967). Due to the small surface area of the neutron star, the magnetic field density close to the surface is significantly increased ($B \approx 10^{12}\,\mathrm{G}$) in comparison to the magnetic field of the predecessor star and constrained to the $\sim 1\,\mathrm{km}$ size magnetic poles. The misalignment of the magnetic axis to the spin axis creates the so-called 'lighthouse' effect, where the beam of the X-ray emission rotates with the neutron star and is only observable when directed towards Earth. The observed pulse profiles in different energy bands can be used to establish a geometry of the system. For single peaked profiles, it is very likely that only one magnetic pole of a single dipole field is observed, whereas more complex and/or asymmetric profiles indicate the existence of a higher order magnetic field. In addition, light bending effects due to gravitation can make the second pole, which is located behind the horizon of the neutron star, visible (Kraus et al., 1995). Also, the individual magnetic poles can be misaligned and an offset has to be taken into account.

Long monitoring observations of individual pulsars, showed a small (on the order of $10^{-13}\,\mathrm{s/s}$) systematic change in the pulse periods. Using radio and X-ray observations, these pulse periods can be monitored very precisely and then be used to further define the nature of the pulsars.

In isolated neutron stars the pulse period decreases because of the loss of rotational energy due to the magnetic dipole radiation. In the monitoring of such systems, sudden spin-ups in the pulse period have been observed (Espinoza et al.,

2011). These 'glitches' only persist for a few days, before the pulsar continues its normal spin-down. These changes in the pulse period are believed to be an indication for the existence of a superfluid in the interior of the star (Baym et al., 1969b), where the 'glitch' occurs when a sudden transfer of angular momentum between the core and the outer crust takes place.

In binary systems, the accreted material plays a major role in the spin period evolution. In Roche Lobe overflow systems (see section 1.2.4 for details), an accretion disk builds up, and the magnetic field of the pulsar couples to the Keplerian angular velocity of the inner disk radius. The neutron star spins up or down, until the spin period is equal to the Kepler period in the part of the coupled disk. This can be observed as a generally monotonous increase (or decrease) of the pulse period on long time scales. For wind accretion systems, the pulse evolution depends heavily on the amount and direction of the accreted matter. Such an evolution is in general more random and the pulse period is varying stochastically around an average value.

1.2.4 Accretion mechanisms

Neutron stars and black holes are some of the brightest persistent galactic sources in the X-ray energy band, although they do not have any internal processes which could create such high luminosities. Accretion is the only possible energy source able to create sufficient energy for such systems. This section describes the energy gain from accretion and discusses the different accretion scenarios in binary systems.

Accretion of external mass in a gravitational potential can be one of the most efficient ways to produce large amounts of energy, enough to be able to explain the observed luminosities in neutron star and black hole systems. The energy of a free falling particle onto a neutron star is given by:

$$\Delta E_{\mathrm{acc}} = \frac{G M_{\mathrm{NS}} m}{R_{\mathrm{NS}}} - \frac{G M \mathrm{NS} m}{R_{\mathrm{init}}} \tag{1.2}$$

where R_{NS} is the radius ($\sim 10\,\mathrm{km}$) and M is the mass of the neutron star ($\sim 1.4\,M_{\odot}$). For a particle with a mass of $m = 1\,\mathrm{g}$ starting outside of the gravita-

tional potential ($R_{\rm init} = \infty$) the obtained energy gain due to accretion is $\Delta E_{\rm Acc} = 1.86 \times 10^{20}$ erg. In comparison, the fusion of 4 hydrogen nuclei into 1 helium nucleus releases ~ 26.72 MeV (4.3×10^{-5} erg), resulting in a total energy gain of $\sim 6 \times 10^{18}$ erg per 1 g mass. The energy gained from accretion is, however, highly dependent on the size of the system. It is very efficient for neutron stars with their large mass and a small radius of ~ 10 km, and even more efficient for black holes, where the size is determined by the Schwarzschild-radius (typically ~ 3 km for a mass of $1\,M_{\odot}$). In comparison, main sequence stars can have radii which are many orders of magnitude larger than the neutron star radius, making the energy gain from accretion neglectable compared to the energy created by the hydrogen fusion process.

In binary systems, where one star evolved into a neutron star or black hole, the majority of the accretion material comes from the optical companion. In such systems, three possible scenarios can occur, which are highly dependent on the orbital geometry and the mass of the optical companion.

Roche Lobe Overflow

Roche Lobe overflow is the primary accretion mechanism in low mass (optical companion $<10M_{\odot}$) X-ray binaries (LMXBs) and/or late type stars, where the donor star is not massive enough to possess a strong stellar wind. The Roche potential (Fig. 1.3) and its significance in transferring matter from one star to another was introduced earlier. When a star exceeds its Roche surface, material outside of the surface is no longer gravitationally bound to the star and can be easily accreted onto the compact object. Due to the rotation of the donor star and the orbital motion, the accreted material has a large initial angular momentum and therefore cannot directly fall onto the compact object. A gravitationally bound disk is formed (Fig. 1.5), where some of the material can lose its angular momentum due to magneto-hydrodynamical interaction with other material, and slowly migrate inwards. The density at smaller radii increases with time, increasing the loss of angular momentum and the temperature in the inner parts of the disk. This is often observed as one or multiple black body components in the spectrum,

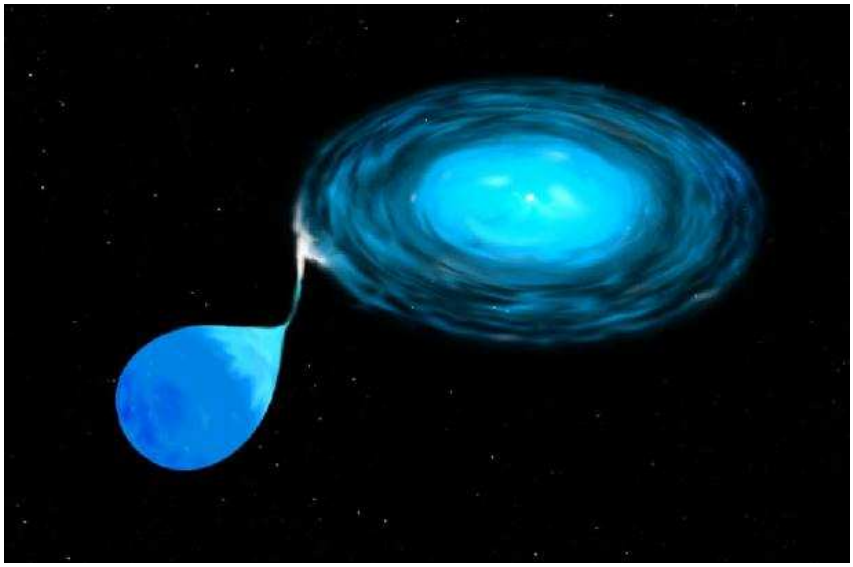

Figure 1.5 Matter is transfered via Roche Lobe overflow from the optical companion to the compact object (center of disk) in a binary system. Due to the initial angular momentum of the transferring matter, an accretions disk is formed, feeding slowly the accretion onto the compact object. Credit: P. Marenfeld and NOAO/AURA/NSF

forming the typical power law shape in binaries. The internal structure of such disks varies from simple thin disks, suggested by Shakura (1973), to more complex phenomena, such as the warped thin disks, which have been suggested, e.g., for the case of Her X-1 (Schandl & Meyer, 1994). A detailed description of different disk geometries and radiation processes can be found in Wilms (1998), Pottschmidt (2002), and references therein. An indication of the existence of a disk is the existence of a monotonic change in the pulse period over a long time scale where the magnetic field of the compact object couples to parts of the disk, slowing or accelerating the spin of the primary until it reaches the Kepler period of the disk (as has already been described in section 1.2.3).

Wind accretion

The primary accretion mechanism in high mass X-ray binaries (HMXBs) is thought to be accretion from the stellar wind of the companion, usually an O– or B–type star (e.g., Davidson & Ostriker, 1973). Material from the companion

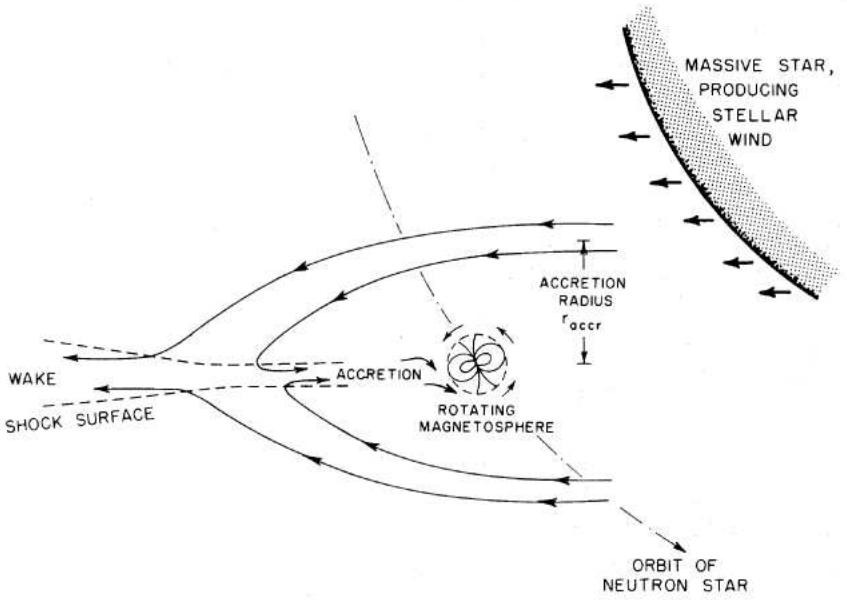

Figure 1.6 Bondi-Hoyle accretion from the stellar wind onto the neutron star. Often the accreted wind creates a shock surface in the wake of the compact object, before it gets captured by the magnetosphere. No or only a small disk is created around the compact object in such a case.

star is radiatively accelerated to up to the order of 2000 km/s (Castor et al., 1975) and a small portion is captured by the gravitational field of the neutron star (Bondi-Hoyle accretion, Fig. 1.6). Once captured, the material falls inward until the influence of the magnetic field forces the matter to be channeled onto the magnetic poles. Bondi-Hoyle accretion is highly dependent on the relative velocity of the neutron star with respect to the wind ($\sim v^{-3}$, from Bondi & Hoyle, 1944), therefore it is of importance to determine the velocity difference between the stellar wind and the orbiting neutron star. Orbital solutions provide the neutron star's velocity and stellar wind theory can provide the theoretical wind velocity, which then can be compared with observations. The observed X-ray luminosity is directly dependent on the amount of gas accreted onto the neutron star and can vary rapidly due to the complexity of the stellar wind and possible clumping of material. HMXB light curves generally exhibit strong fluctuations and flaring on time scales not correlated to the orbit, which are interpreted as due to the variations in the wind. Sudden jumps in the pulse period are also observed on

time scales of weeks, especially during high activity.

The wind in HMXBs is most likely accelerated by elemental absorption lines in the wind material in so-called line driven wind acceleration, where elemental lines absorb optical (or UV) photons from the star and re-emit new photons isotropically. The momentum gain drives the wind outwards, where the moving material can capture a photon with slightly lesser wavelength due to redshift. One of the first and simplest models for this wind acceleration is the spherical Castro, Abott, and Klein (CAK) model (Castor et al., 1975), where the wind profile is calculated as a function of distance from the companion star:

$$v(r) = v_{\rm inf}(1 - \frac{R_{\rm OC}}{r})^{\beta} \tag{1.3}$$

where $v_{\rm inf}$ is the terminal velocity and $R_{\rm OC}$ is the radius of the optical companion, and β describes the acceleration of the wind, where for $\beta = 0$ the wind is accelerated immediately to the terminal velocity. With the velocity profile a density profile of the wind can be calculated and compared to the observed absorption throughout the orbit. In reality, many sources cannot be fully described with a simple CAK model and additional contributions, such as shocks in the radiative driven wind, have to be introduced to achieve acceptable results in comparison with the data. Section 4 and 6 discuss applications of wind models to the binary systems Cen X-3 and GX 301−2.

Be-Binaries

Be-Binaries are binaries where the optical companion is a fast rotating B-type star with an extended envelope or a gaseous disk at its equator (Fig. 1.7). The spectra of these stars show highly variable emission lines (the 'e' part of Be-stars) which are formed in the envelope or disk. A detailed discussion of classical Be-stars can be found in Porter & Rivinius (2003). The compact object in such a system is usually in a very eccentric orbit around the Be star. The eccentricity of the orbit stems from the orbital disruption in the supernova explosion of the compact object, and is also very dependent on the amount of mass transfered to the optical companion. This highly eccentric orbit is also the reason that the

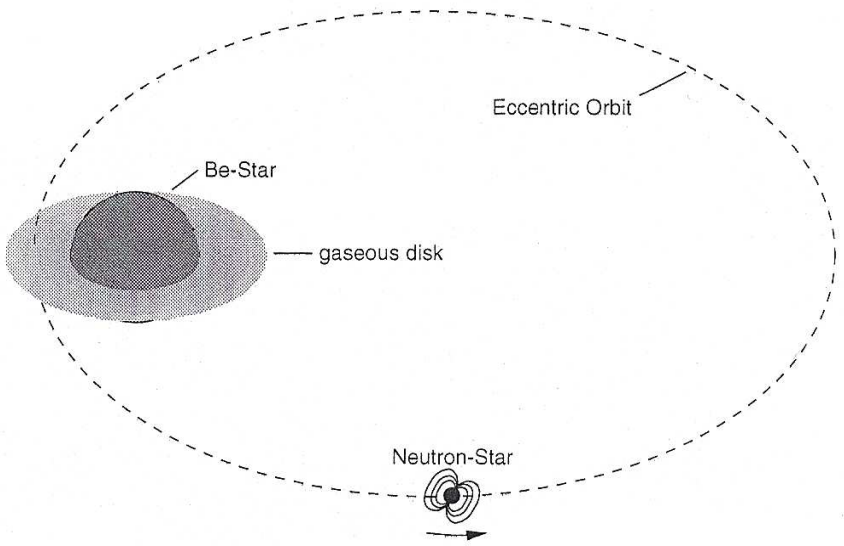

Figure 1.7 Schematic view of a Be-Binary system where the neutron star is on an eccentric orbit and passes through the outer layers of the optical companion during periastron. From Kretschmar (1996)

majority of these sources are transient in nature. When the compact object is far away from the optical companion, only a small amount of material is accreted and the source flux is reduced in the X-ray band, often below the sensitivity of modern satellites. When the companion approaches periastron, it goes through the outer layer of the envelope or the disk of the Be-type star and gravitationally binds some of the material it encounters. The bound material can create a small accretion disk around the compact object and material is accreted via the magnetic field lines onto the neutron star. This process increases the luminosity significantly. The source will brighten in X-rays for a fraction of the binary orbit, in general a few days. When the neutron star leaves the region of enhanced accretion, the bound material depletes rapidly, and the X-ray luminosity decreases until the system becomes dim again. In general it remains in a low luminosity state until the neutron star approaches its companion on the next orbit and the same sequence repeats.

Such outbursts are very periodic and can often be predicted reasonably well. EXO 2030+375 (see, e.g., Parmar et al., 1989a,b; Klochkov et al., 2008a, and references therein) and A 0535+26 (Caballero et al., 2007, 2008) are two prime examples

of Be-Binary systems with slightly different properties. Whereas EXO 2030+375 can be observed throughout its whole $\sim$ 46 day orbit and brightens significantly throughout its periastron passage, A 0535+26 is below the detection threshold of most existing instruments throughout large parts of its 111 day orbit and flares primarily before its periastron passage. Due to geometrical constrains, as well as activity levels of the optical companion, not every outburst has the same intensity, and often a source can be quiet for multiple orbits. In addition to the regular periastron flares in A 0535+26, this source also experiences rare and unpredictable giant outbursts (see Caballero et al., 2008, for references), which are independent of the position along the orbit. During the time of the outburst, the emission lines in the optical companion disappear (Haigh et al., 1999), indicating a loss of its extended envelope so that significantly less material was accreted onto the neutron star.

1A1118 is a peculiar Be-binary with only three observed outbursts up to date. Section 5 analyzes the obtained *Suzaku* data of this source and discusses a possible orbital period.

Chapter 2

Instruments

The atmosphere of the Earth is opaque in X-ray wavelengths, making it impossible to observe X-ray emission from extra-terrestrial sources from the ground. Three methods are commonly used to lift the instruments to the top of and beyond the atmosphere: high altitude balloons, sounding rockets and satellites.

High altitude balloons can lift detector payloads to a height of more then 40 km above the densest part of the atmosphere. Such balloon flights can last from a few hours (Harrison et al., 2000) to multiple days (Boggs et al., 1998), and are often used as a cost effective way to test and space-qualify new detectors before implementation in satellites. Although the height is sufficient to detect extraterrestrial X-rays above ~ 20 keV, the short exposure times and the remaining atmosphere reduce the effectivity, allowing only the brightest sources to be observed.

Sounding rockets can transport instruments to an altitude of over 100 km, where the atmospheric influence can be fully neglected. Sounding rockets were used in the pioneer era of X-ray astronomy, e.g, in the experiment leading to the discovery of the first extra-solar X-ray source Sco X-1 (Giacconi et al., 1962), and still are in use mainly for testing individual detectors[1]. The strong limitation of sounding rockets is the short time of only a few minutes that the instruments are above the atmosphere.

The largest source of scientific X-ray data nowadays are satellites with mis-

[1] http://sites.wff.nasa.gov/code810/missions.html

sion lifetimes of multiple years. Although much more expensive than high altitude balloons or sounding rockets, satellites allow for much longer observation times, since they observe independent of the daytime, atmospheric conditions, and can achieve multiple scientific goals.

Each satellite mission has its own strengths and weaknesses, where the long mission times allow for reoccurring observations of individual sources. Most satellites have a limited field of view (FOV), e.g., 1° (*RXTE*, PCA and HEXE) and 25' and 4.5° (*Suzaku*, XIS and HXD above 60 keV, respectively), allowing a detailed study of individual sources and regions in the sky. Other instruments, such as *Swift*/BAT or *Fermi*, have large FOV covering a large portion of the sky simultaneously, searching for unpredictable events, e.g., Gamma-ray bursts, which can occur in any direction. Such events can only be observed by accident with satellites with limited FOV, e.g., the discovery of the X-ray outburst during the birth of a supernova (Soderberg et al., 2008). The monitoring capability of satellites also allows observations of changes in individual sources on long time scales, e.g., outbursts in transient sources or state changes in black hole binaries. In addition, long term monitoring of pulse periods can help to understand the pulse evolution in pulsars.

In this thesis, I use data from two of these satellites, *RXTE* and *Suzaku*, to study matter accreted on HMXBs. The following sections describe the individual satellites in detail and give a short overview of major events during the missions.

2.1 Rossi X-ray Timing Explorer

The *Rossi X-ray Timing Explorer* (RXTE) was launched on 1995 December 30 with a Delta II rocket from the Kennedy Space Flight Center into a low earth orbit (LEO) with an altitude of $\sim$ 580 km and an inclination of 23° (see `http://rxte.gsfc.nsa.gov/`). Since its launch, the altitude decreased to $<$ 500 km (e.g., Fig. 26 in Jahoda et al., 2006). The large inclination causes half of the satellite orbits per day to pass through parts of the South Atlantic Anomaly (SAA), a region above the South Atlantic Ocean and parts of Brazil, where high

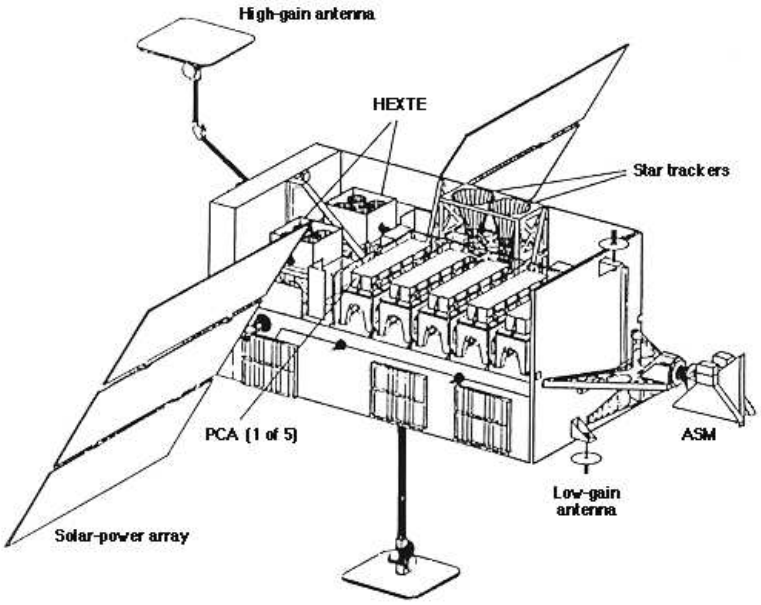

Figure 2.1 Schematic view of the RXTE spacecraft with the main instruments labeled. The PCA and the two HEXTE detectors are pointing instruments. The ASM is the located on the right and has a large, unobstructed view of the sky. The two star trackers are used to position the satellite. From Bradt et al. (1993).

energy particles can penetrate deeper into the earth's atmosphere (see, e.g., Fürst et al., 2009, and references therein). The instruments' high voltages have to be turned off or reduced during the passages through the SAA to protect the detectors from damage due to the high particle fluxes. The *RXTE* solar panel rotation and satellite roll allow *RXTE* to observe any point on the sky at any time of the year. A 30° radius around the Sun defines a solar exclusion region in which pointed observations are not allowed due to thermal and instrument safety considerations.

Originally the mission was scheduled for only 2 years, but was so successful that the mission was extended several times and recently celebrated its 15th year of operation, making it the longest running X-ray satellite mission to date. Three scientific instruments are found on *RXTE* (see Fig. 2.1): The two pointing instruments are the Proportional Counter Array (PCA) and the High Energy X-ray Timing Experiment (HEXTE), which are both co-aligned and used to observe individual sources as proposed by the scientific community. The All Sky Monitor (ASM) scans the sky throughout each orbit and monitors X-ray sources for a

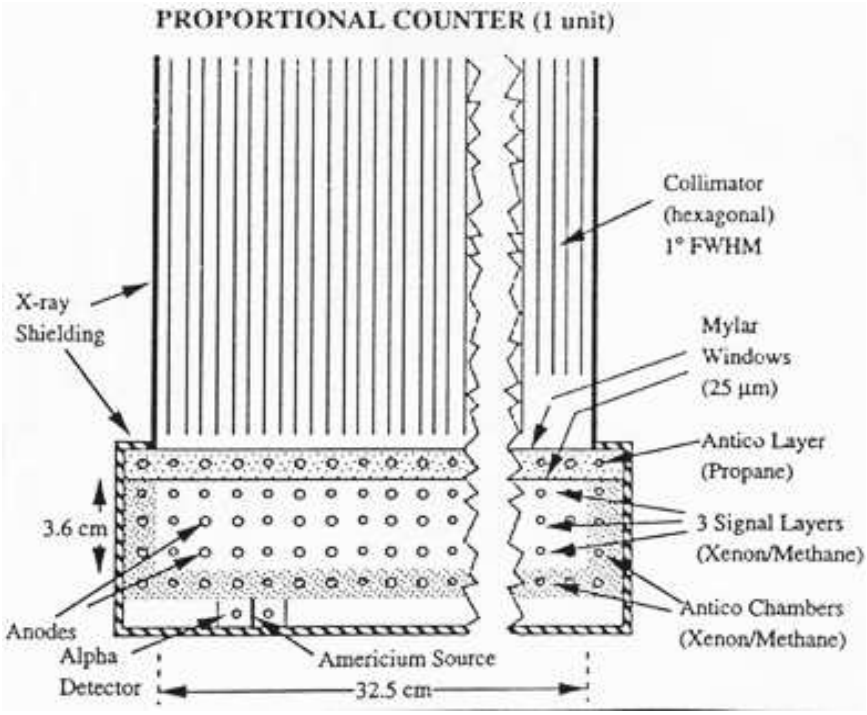

Figure 2.2 Schematic view of one of five PCU indicating the different parts of the instrument. From Bradt et al. (1993).

changing level of activity, e.g., an outburst of an X-ray transient.

2.1.1 Proportional Counter Array

The PCA was developed in the Laboratory for High Energy Astrophyiscs at Goddard Space Flight Center, and consists of five individual, co-aligned gas proportional counter units (PCU 0-4), each consisting of two chambers, a thin Propane layer on top and a larger Xenon/Methane chamber below (see Fig. 2.2). Five layers of anodes are distributed throughout the detector, where the top layer is embedded in the Propane layer and acts as an anti-coincidence shield for cosmic rays. The lowest anode layer, as well as the outermost anodes in the Xenon/Methane chamber also act as veto counters and are used to filter out unwanted photons and high energy particles entering the detectors from the side. Surrounding each of the anodes is an array of grounded cathode wires that define $1.3\,\mathrm{cm}\times1.3\,\mathrm{cm}\times1\,\mathrm{m}$ cells. Each PCU has a tagged ^{241}Am source for continuous calibration purposes.

With an effective area of $\sim 1300\,\mathrm{cm}^2$ for each of the PCUs, the PCA has one of the largest collecting areas in the X-ray band (Jahoda et al., 1996). The nominal energy range goes from 2 to 60 keV, with an energy resolution of 18% at 6 keV.

Proportional counters work on the premise that incident photons are photoelectriclcy absorbed by a Xenon atom and the emergent electron is accelerated towards the high voltage anodes. On the way they collide with more gas molecules, creating an electron cascade. The charge collected by individual anodes is amplified and processed in the on-board electronics. The Methane in the gas mixture functions as quenching gas, absorbing photons created in the electron cascade without getting ionized. This reduces the charge collection time, and thus also decreases the recovery time for subsequent events. A more detailed discussion of proportional counter detectors can be found in chapter 6 of Knoll (2000).

A hexagonal BeCu tube collimator is mounted on top of each individual PCU, restricting the FOV to 1°. In most cases this is sufficient to contain one source at the PCU sensitivity limit, even in the crowded galactic center. In cases where a second source is within 1°, e.g., the two pulsars 2E 1145.1-6141 and 2S 1145−619 (Lamb et al., 1980; White et al., 1978b), where the two objects are only 15' apart, the PCA is not able to distinguish whether the individual photons come from one source or another, leading to source confusion in the data. Such cases are rare, but have to be considered when planning observations of individual sources and/or extended emission regions, and off-set pointings may be required.

The PCA is a fixed pointing detector without the capability of measuring a simultaneous background for its observations. The PCA instrument team provides a predicted background based upon a background model for the different PCA gain epochs, which correspond to high voltage changes in the individual PCUs (see below). In addition, background and calibration observations are performed on a regular basis to provide input for the background predictions and to assess the effect of long time degradation in the detectors (Jahoda et al., 2006). Two background models are provided for each epoch, the `Sky_VLE`-model, used for bright galactic sources, and the `Faint`-model used mostly for extragalactic or weak galactic sources. Both models consists of three main components:

- Diffuse cosmic background, where the source of background photons are the unresolved extra-galactic sources (see, e.g., Comastri et al., 1995; Hasinger et al., 2002).

- Local particle background consisting of energetic protons and electrons which can produce energy losses in the detectors similar to those of X-rays. The particle dosage, as measured by the particle monitor on the HEXTE instrument (Rothschild et al., 1998), is used in the theoretical model description along with the rates in the anti-coincidence cells on the sides and bottom of the Xenon region.

- Internal background caused by high energy particles interacting with the detector and the satellite, e.g., during SAA passages, where the incident particles cause nuclear reactions in the material of the instrument. When the newly created isotopes decay, the created photons and electrons increase the background in the detector. This component of the internal background decays exponentially after such an activation with a decay half-life time of ~ 24 minutes (Jahoda et al., 2006).

Throughout its mission, several major events reduced the performance of the PCAs[2]:

- Shortly after the launch PCU 3 and 4 showed occasional high count rates, which might have been caused by breakdowns in the Xenon/Methane chambers. To minimize these effects, the anode high voltage during scientific observations was reduced in multiple steps, so called epochs. In addition, the individual PCUs were turned off periodically throughout observations so that the Xenon/Methane gas could recover. While at the beginning of the mission often all 5 PCUs were on simultaneously, only 2 PCUs on average were turned on at the same time in more recent years.

- On 2000, May 12, the Propane layer in PCU 0 lost its pressure over the period of one day, possibly due to a micro-meteorite puncturing the outer window.

[2]see `http://heasarc.nasa.gov/docs/xte/whatsnew/big.html`

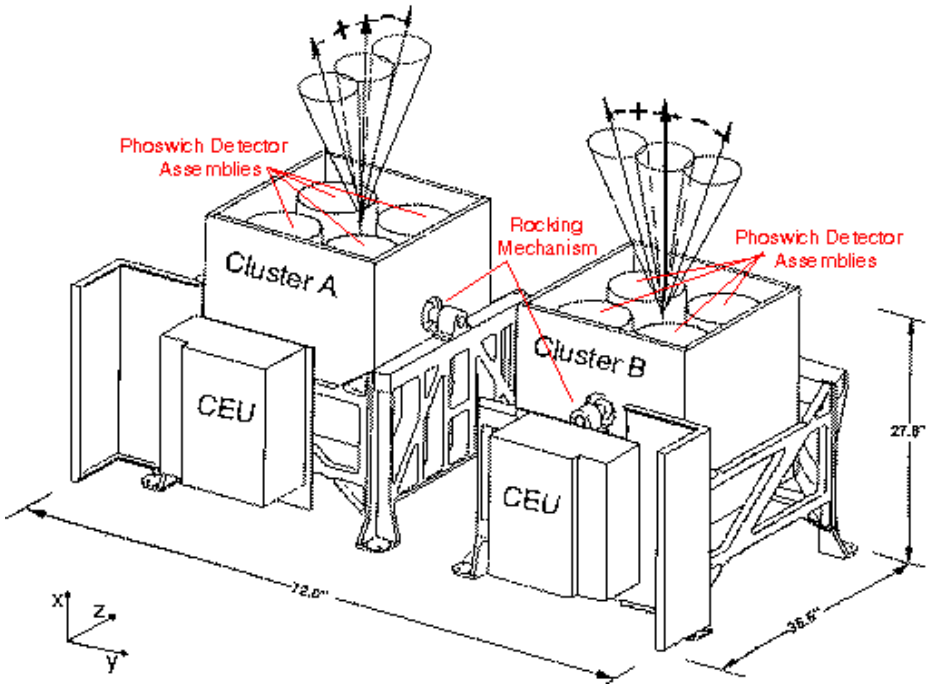

Figure 2.3 Diagram of the HEXTE cluster A and B where the three pointing positions, one source and two background pointings are indicated with their respective FOVs.

The Xenon/Methane chamber was not affected and remained functional after the instrument was turned back on a few days later. PCU 0 is still used for scientific analysis, although the increased background limits the usage to brighter sources. A new background model for PCU 0 was provided shortly after this event.

- On 2006, December 25 the Propane layer of PCU 1 suffered a similar event, where the pressure in the Propane layer declined and the Xenon/Methane layer was not affected. Again, observations could continue with an increased background and due to the periodic cycling of the different PCUs the impact on the scientific PCA results was only marginal. Similar to PCU 0, the increased background limits the use of PCU to brighter sources only.

2.1.2 High Energy X-ray Timing Experiment

The HEXTE instrument was developed at the Center for Astrophysics and Space Sciences (CASS) at the University of California, San Diego. The HEXTE detectors consist of two clusters (A & B) each containing four NaI(Tl)/CsI(Na)-Phoswich scintillation detectors (Rothschild et al., 1998). In front of each detector a hexagonal lead collimator limits the FOV to $\sim 1°$, co-aligned with the PCA instruments discussed above. The nominal energy range goes from 15 keV to 250 keV with an energy resolution of $\sim 15\%$ at 60 keV.

An incident photon excites scintillation light in the 3 mm thick NaI(Tl) scintillator material. A second, thicker CsI(Na) scintillator detector below the NaI(Tl) scintillator is used as an anti-coincidence shield for charged particles and photons coming from the bottom and the sides of the detector. It also acts as a light guide for the scintillator light from the NaI(Tl) layer. The photons created by the scintillators pass through a fused quartz window and strike the photocathode behind the entrance window of the photomultiplier, creating a cloud of free electrons, which is accelerated onto the first dynode, and then amplified via secondary emission through several dynode stages until reaching the final anode, where the accumulated charge is processed by the on-board electronics. Each of the detectors has an additional continuously tagged ^{241}Am calibration source, where the line energy of the source is used to auto-align the gain for each detector to be the same for all detectors in a cluster. Direct combination of events from detectors within a cluster does not affect energy resolution and simplifies data analysis.

In contrast to the PCA, HEXTE is capable of measuring the near-realtime background for each detector. Each cluster is mounted in a way that allows it to be moved either $\pm 1.5°$ or $\pm 3°$ from the original pointing position. To minimize the possibility that another source in the vicinity contaminates the background, cluster A and B are mounted with rocking axes perpendicular to each other, thus modulating between 4 background regions around the main source (see Fig. 2.3). If the background is contaminated in one background region, the other region can still be used to measure an instrumental background. This eventually guarantees that the background for each cluster will be measured for every observation. In

addition, the software `HEXTErock`[3] can provide information of known X-ray sources which could contaminate a cluster's background FOV in a specific observation. The clusters 'rock' with a 16 or 32 second dwell time on-source, where one cluster is always pointed at the source, and the other one is viewing one of the background regions. After the dwell time of 16 or 32 seconds, the off-source cluster moves on-source, and the other cluster moves to an off-source background position. This sequence continues until all off-source positions were observed, before it repeats again (see Figure 2.3). The HEXTE instrument also has the capability to stop modulation and can be stopped at a specific position. The following major events affect the performance of the HEXTE instruments:

- Shortly after the launch, on 1996 March 6, the pulse shape analyzer of one of the four HEXTE detectors in cluster B failed. Data are still processed and can be used for timing studies, but is not useable for spectral analysis. For the most scientific observations, this detector is ignored.

- Between 2004 December 13 and, 2005 January 14, the HEXTE Cluster A occasionally stopped modulating in a position halfway between the background and the source position. The system was rebooted on 2005, January 14th, resuming full function.

- In 2005, December 12, the same cluster encountered a similar event, where modulation stopped again and was fixed in an off source position. Again a reboot of the cluster and reinitialization of the modulation restored full function.

- In 2006, October 20, multiple on- and off-source modulation anomalies were observed in cluster A, where the cluster stopped its motion in different positions. After rebooting, the cluster recovered but failed again after a few days. The decision was made to stop cluster A in the on-source position to allow the continuation of data collection without risking that the instrument would get stuck off-source without a chance of recovery. The HEXTE instrument

[3]http://mamacass.ucsd.edu/cgi-bin/HEXTErock.html

team generated a background estimation tool (`hextebackest`), which uses background data of the functional cluster B to calculate the background for cluster A (Pottschmidt et al., 2006).

- In 2009, December 14, HEXTE cluster B ceased modulation. After multiple reboots the decision was made to stop cluster B in an off-source position, rather than risk a breakdown in a non-recoverable position. Using cluster A, which is kept in the on-source position, and the `hextebackest` model with background data of cluster B, the HEXTE instrument is still capable to obtain scientifically relevant data.

2.1.3 All Sky Monitor

The ASM, developed by the Center for Space Research at the Massachusetts Institute of Technology, is the third scientific instrument onboard RXTE and is used to monitor the long term flux variability of known X-ray sources in the sky as well as to discover new transient sources. With a highly automated extraction pipeline and an automated distribution on the world wide web, the scientific community can be easily notified about the activity of individual sources within 24 hours.

The ASM detectors consist of 3 Scanning Shadow Cameras (SSCs), with a FOV of $6° \times 90°$ each. The three cameras are mounted on a rotatable shaft at one end of the *RXTE* spacecraft (see Figure 2.1) and, with programmed shaft rotations, cover $\sim 80\%$ of the sky throughout one satellite orbit. Each camera points for 90 seconds to a region in the sky and then moves to a new position. The instruments are based on the coded mask principle, where a partially coded mask is located above each detector plane, casting a unique shadow pattern on the detectors for every sky position. This pattern can then be used to recover the source positions and individual count rates. For multiple sources, as expected in such a large FOV, the shadow pattern is much more complicated and requires a complicated deconvolution algorithm to extract the position and luminosity of individual sources.

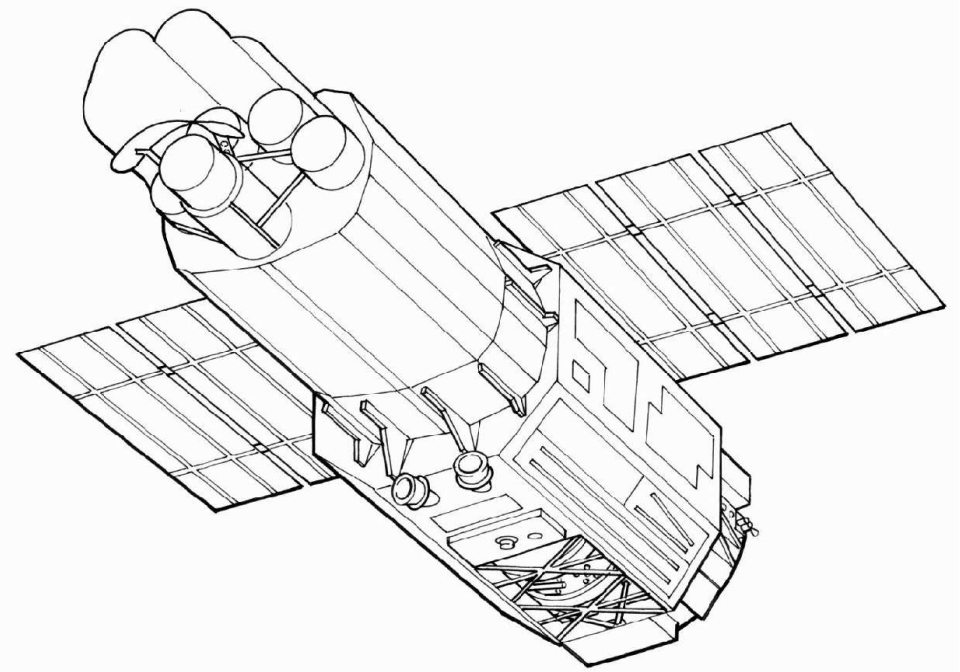

Figure 2.4 Schematic view of the *Suzaku* satellite showing the 5 XRT mirrors (circles) at the front. the HXD detector is mounted on the top and is not visible here.

The detectors are position sensitive proportional counters (PSPCs) with an energy range of 2-12 keV providing energy information in three energy bands. With multiple anodes, the PSPC has a spatial resolution that can provide the direction of the source. The ASM can resolve individual sources with a $3' \times 15'$ accuracy on the sky. For the $\sim$ 150 monitored sources, data are available for each $\sim$90 s pointing and summarized on a daily basis. Such a detailed montioring allows for the possibility of very fast follow up observations with *RXTE* and other pointed missions.

2.2 Suzaku (Astro-E2)

The *Suzaku* (*Astro-E2*) mission was launched in 2005, July 10, after the launch vehicle for the first *Astro-E* mission malfunctioned and failed to achieve orbit in 2000. *Suzaku* is in an low earth orbit with an altitude of $\sim$ 570 km and an inclination of 31°. One of the three main instruments, the low energy

X-ray spectrometer (XRS), failed a few days after the launch due to a thermal short between the helium and neon tank, resulting in the loss of the liquid helium coolant. A detailed description of the XRS can be found in Kelley et al. (2007). The two other main instruments are the X-ray Imaging Spectrometer (XIS) and the Hard X-ray Detector (HXD) and are discussed in detail below. Five X-ray telescopes (XRTs) are used to image the X-ray sky in the field of view onto the four XIS instruments and the XRS detector, where photons are reflected under grazing angles and are focused onto the individual instruments. In contrast to *RXTE*, *Suzaku's* solar panels are fixed, limiting the visibility of most sources to two observation time windows each year. Figure 2.4 shows a schematic layout of the *Suzaku* satellite with its main instruments. A full technical description can be found in the technical design report on the *Suzaku* homepage: `http://heasarc.nasa.gov/docs/suzaku/prop_tools/suzaku_td/` .

2.2.1 X-Ray Imaging Spectrometer

The XIS is the low energy instrument of the *Suzaku* satellite and consists of 4 individual charge coupled devices (CCDs), where one is a back illuminated (BI) and the other three are front illuminated (FI) CCD chips. Each XIS instrument has a single 1024×1024 pixel CCD chip, which images a $18' \times 18'$ region of the sky, defined by the FOV of the XRTs. The difference between FI and BI CCDs is the position of the gate structure, which transfers the charge packets to the readout electronic. In FI CCDs the incident X-ray photons have to pass through the gate structure before they are detected, reducing the efficiency for low energy photons. For the BI CCD, the gate structure is on the back and thus it has a larger effective area below 2 keV, whereas the FI CCDs are more effective above 2 keV. ^{55}Fe sources are positioned between the chips, so that two corners of each detector are illuminated and can be used for inflight calibration and degeneracy studies. The energy range of the detectors is $0.5-12$ keV with a resolution of 150-200 eV for the Mn Kα emission line from the ^{55}Fe source.

Three CCD readout window options are provided, depending on the brightness of the source. In full window mode the whole CCD area is read out every

8 s, whereas the 1/4 window mode allows for a faster readout of 2 s to minimize the pile-up effect in bright sources. The caveat of the 1/4 window mode is that only the center region on each CCD is read out, excluding the corners with the calibration sources. In addition, the CCDs can also be operated in a 1/8 window mode, where the read out area is smaller than the point spread function (PSF) of the X-ray telescopes. This mode is therefore not recommended by the instrument team.

Pile-up occurs when two incident photons hit the same detector pixel or adjacent pixels between readouts. These photons cannot be distinguished and are processed as a single photon with an energy higher than that of the individual photons. In such a case, too many photons are measured at higher and too few at lower energies, possibly influencing the physical interpretation of the data, i.e., the source spectrum appears harder than its original energy distribution and the inferred flux will be incorrect. *Suzaku* data in this thesis were tested for pile-up and regions with more than 5% pile-up were excluded from further analysis (see section 5&6).

For extremely bright sources, the readout time can be further reduced with either the Burst option or the Parallel-Sum (P-Sum) clock mode in the XIS. In the P-Sum mode, multiple rows are added during the readout process and spatial resolution in one dimension is lost. The highest time resolution obtainable in P-Sum mode is ~ 7.8 ms. Due to the loss of imaging capability in this mode, it is only used in cases where a very high time resolution is extremly important. The Burst option can be used in the full and 1/4 window mode and uses the variable time t to reduce the exposure time to 8 s-t and 2 s-t, respectively. The remaining time t of a readout cycle is ignored. The use of the Burst option in the full window is generally not recommended and it should only be used for bright, extended sources.

Due to the imaging capability of the XIS instruments, the source region can be selected on the obtained image, taking the point spread function (PSF) into account. In general, a region in the same image can be selected as a background region, which is then used to extract a measured background. It is recommended

to keep the size of the background region similar to the size of the source region.

The XIS encountered multiple significant events limiting its operational capability:

- On 2006, November 9, XIS 2 was hit by a micro-meteorite, affecting most of the imaging area. XIS 2 was not useable after this incident.
- On 2009, June 23, another micro-meteorite hit XIS 0 and made $\sim 1/8$ of the area not useable for readout. Luckily the affected area is not in the center region of the CCD and scientific analysis is only potentially affected in the full window mode.
- On 2009, December 19, a third micro-meteorite hit the XIS 1 instrument. This meteorite did not create any damage on the CCD, but most likely punctured a hole in the optical blocking filter (OBF). The impact of the loss of the OBF in a small region is not yet fully understood.

The data in this thesis are only affected by the loss of the XIS 2 detector, resulting in a slightly lower signal to noise ratio at low energies.

2.2.2 X-ray telescopes

To minimize the detector noise in the XIS instruments, the individual CCD pixels are fabricated very small, resulting in a very small collection area of the instrument. With X-ray telescopes (XRTs), the collecting area can be drastically increased by focusing the incident photons on the small detector area.

An incident X-ray photon from a random direction is mostly absorbed instead of being reflected by most materials. This provides a challenge when trying to focus X-rays onto a detector. For most materials, the index of refraction is $n \sim 1$ for X-rays, so that reflection only occurs at very small incident angles highly dependent on the photon energy. The small angles result in focal lengths of multiple meters, which is very challenging for implementation in satellites due to constraints in the size of the payload space.

Hans Wolter introduced a telescope design, where the X-ray photons hit the reflecting material under a grazing angle of $< 4°$ (Wolter, 1952b,a). The use

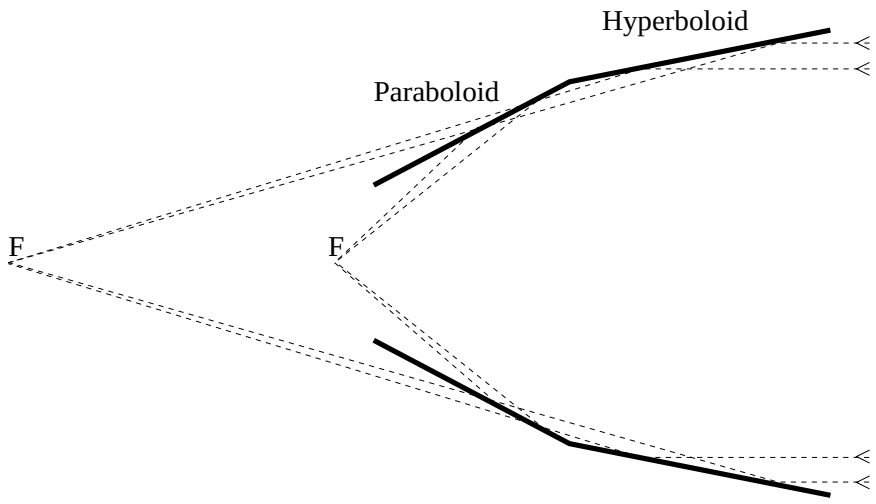

Figure 2.5 Schematic view of Wolter Type I mirrors and the light path of incident photons. The double reflection on a hyperboloid and a paraboloid decreases the focal length significantly without the loss of spatial resolution. The individual mirrors are nested to increase the photon collection area.

of a combination of parabolic and hyperbolic mirrors (Fig. 2.5) allowed a decrease in total focal length, making such telescopes more suitable for satellites. The use of nested mirrors with the same focal length allows one to increase the collection area of the mirrors significantly.

Conventional X-ray mirrors are made of polished and very smooth glass ceramics, which are coated with metal to increase reflectivity, and are nested to give a larger collecting area. Such telescopes have a high spatial resolution and can produce sharp images in the X-ray band with sub arc-second spatial resolution (e.g, Chandra, Zhao et al., 2004). Due to the necessary precision and the thickness of the individual shells, these mirrors are very heavy, expensive, and have a limited collecting area.

In a different approach, the reflective surface consists of many layers of thin aluminum sheets, which are coated with a high density material to increase reflectivity and then formed into the individual mirror shells. Unfortunately, the very thin mirrors can not be fabricated with the same precision as the conventional X-ray mirrors, limiting the spatial resolution to fractions of an arc-minute. The use of very light material and the easy fabrication process allows for a very inexpensive

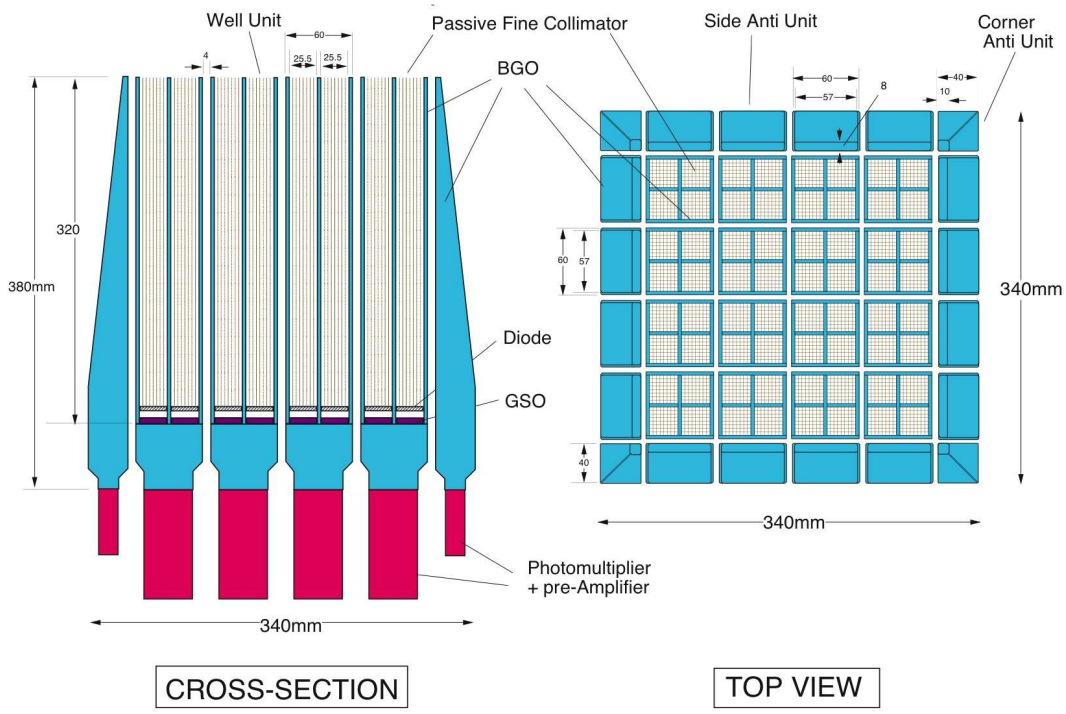

Figure 2.6 Schematic picture of the HXD instrument, which consists of two types of detectors: the PIN diodes and the GSO/BGO scintillators.

production and results in a very lightweight mirror assembly.

The *Suzakus* mirrors each consist of 175 thin-foil nested shells adding up to an effective area of $\sim 440\,\mathrm{cm}^2$ at 1.5 keV and $\sim 250\,\mathrm{cm}^2$ at 8 keV, where the reduction in the collection area at higher energies is due to the smaller angle of total reflection. The mirrors are coated with a thin gold layer to increase reflectivity and to reduce instrumental features due to the reflecting material. Four XRT mirror assemblies are used for the four individual XIS instruments, and a fifth mirror assembly is mounted for the XRS instrument, which failed early in the mission. The focal length of the XRT-Is is 4.75 m with a weight of $\sim 20\,\mathrm{kg}$, each.

2.2.3 Hard X-ray Detector

The *Suzaku* HXD is a non-imaging, collimated hard X-ray scintillation instrument with an energy range from $\sim 10\,\mathrm{keV}$ up to $\sim 600\,\mathrm{keV}$. The detector consists of 16 main detector units, arranged as a 4×4 array, surrounded by 20

crystal scintillators for active shielding (Fig. 2.6). Each unit consists of two types of detectors, a 2 mm-thick Positive Intrinsic Negative (PIN) silicon diode for energies up to $\sim$ 60 keV, and a Gadolinium Silicate/ Bismuth Germanate (GSO/BGO) phoswich scintillator for energies above $\sim$ 40 keV. The 16 scintillators are read out individually by photomultiplier tubes. Passive collimators define the FOV to a $34' \times 34'$ square opening in the HXD instruments below $\sim$ 100 keV. Above $\sim$ 100 keV, these collimators become transparent and the active collimator limits the FOV to $4.5° \times 4.5°$. The effective area of the HXD is $\sim 160\,\mathrm{cm}^2$ at 20 keV and $\sim 260\,\mathrm{cm}^2$ at 100 keV, and the time resolution of the detectors is 61μs, where each event is processed individually.

Similar to the *RXTE*/PCA, the background for both instruments is provided by the instrument team. The background consists mainly of the non X-ray background (NXB) from activation in the detectors and from cosmic rays as well as of the cosmic-X-ray background (CXB) due to unresolved extragalactic sources. Throughout the last years, the GSO background increased significantly due to long-term in-orbit activation. With the longest half-life in the activated material being one year, it is expected that the background will saturate from $\sim$ 2011 onward.

Short term variations of up to a factor of 3 are observed in the PIN background and are anti-correlated with the geomagnetic Cut-Off Rigidity (COR) over the orbit. The COR value indicates how deep a charged particle can penetrate the magnetosphere and activate the detector material, adding background to the observation (see Lemaitre & Vallarta, 1933, for details). The background for the PIN instrument is primarily based on the count rate of the high-enery charged particles, directly measured by the PIN diodes. This rate is saved as the Upper Discriminator (UD) count rate in the housekeeping data and is considered a direct indicator for the flux of the primary cosmic-ray particles. For the modeling procedure, the raw PIN-UD rate is added to an integrated PIN-UD rate with a fixed decay constant taking other effects, such as the passage through the SAA, into account. The spectral shape for the NXB is assumed to be dependent on the COR values as well as the time since SAA passage and is extracted from an existing database based on Earth occultation data. The final PIN background is

modeled with a 10 times higher event rate, suppressing Poisson errors. The CXB, which accounts for $\sim 5\%$ of the PIN background, is not included in the provided background and has to be simulated and added to the background manually. The CXB spectral parameters are based on the data obtained by the High Energy Astrophysics Observatory satellite *HEAO 1* (Boldt, 1987), modeled with a simple power law and a high energy cutoff.

The GSO background model generation is similar to the PIN background, and is also provided by the instrument team. Unlike for the PIN, the cosmic X-ray background is negligible and the background can be modeled to 3% accuracy to data from background pointings. The provided GSO background does not have to be further manipulated before used in the scientific analysis.

2.3 Data Extraction

For all data extraction I used the High Energy Astronomy Software (HEASOFT) with its most recent version for each publication. The data for the individual satellites and sources are stored at the HEASARC Archive facilities at Goddard Space Flight Center and is freely available on the world wide web[4].

2.3.1 RXTE Data

To extract *RXTE* data, a suite of analysis programs based upon the suite of FTOOLs, that are available from the HESARC, were used for generating spectral and temporal (lightcurves) files.

After accumulating the data from the HEASARC, a filter has to be applied to find the times when the source data is minimally affected by external influences. To establish the Good Time Interval (GTI) for each observation, different selection criteria can be applied based on the housekeeping data of the satellite. Only data with more then 10° pointing above the Earth's limb are used, to avoid contamination from X-rays produced in the Earth's atmosphere. As mentioned before, the activation of the detectors when passing through the SAA can be a big

[4]http://heasarc.gsfc.nasa.gov/

problem. To avoid influence from this activation, data within a 30 minute time window since the peak of the individual SAA passages were rejected in the analysis. The pointing of the source position was . An increased level of precipitating high energy particle event can be filtered out by setting the electron ratio to 0.1 or above. In bright sources, the luminosity can increase the electron ratio, so that the threshold value has to be adjusted for the extraction.

After the selection criteria, data was extracted for each individual PCU following the description in the two technical guides: "The ABC of XTE"[5] and "The RXTE Cook Book"[6]. The extracted data has to corrected for the detector dead time, a value that can reach up to 40% in the HEXTE instruments.

2.3.2 Suzaku Data

For the extraction of *Suzaku* data, the HEASOFT package provides another suite of FTOOLs to utilize *Suzaku* specific extraction steps.

The first step, after accumulating the data from the HEASARC, is the attitude adjustment and cleaning of the events, where small variations in the pointing of the satellite and hot pixels in the detector are corrected. As the XIS is an imaging instrument, the image software `DS9` is used to extract an image of the whole data file and to select regions for the source and for a suitable background. To avoid pile-up from bright observations, such as the data set in 1A 1118 (see chapter 5.2.1) the external S-lang routine `pile_estimate.sl`[7] is applied to the data, mapping the estimated pile-up throughout the whole detector. The earlier determined regions have to be adjusted to exclude a pile-up of $> 5\%$. This value was chosen so that the pile-up does not have too much influence on the data and not to much data are lost during the exclusion process. The extraction then follows the "Suzaku ABC Guide"[8], where the selection criteria for the GTI are proposed by the guest observer facility (GOF), i.e., Time since SAA passage (500 s) and the elevation above Earth's limb (5°).

[5] http://heasarc.gsfc.nasa.gov/docs/xte/abc/contents.html
[6] http://heasarc.nasa.gov/docs/xte/recipes/cook_book.html
[7] http://space.mit.edu/ASC/software/suzaku/
[8] http://heasarc.nasa.gov/docs/suzaku/analysis/abc/

For the PIN data, no spatial resolution exists, and the background is provided by the instrument team. From the way how the background is provided, diffuse galactic ridge emission is not taken into account and has to be added manually, following the "ABC Guide". The source data are dead time corrected before the final spectral analysis. GSO data can be also easily extracted without further preparation. The instrumental team also provides the background and response files for each observation.

Chapter 3

Magnetic fields

This chapter introduces the influence of the magnetic field on the accreting matter and the different accretion geometries used to describe the accretion onto the neutron star. It also gives a general overview about the physics behind the observed continuum, as well as the physics of the cyclotron resonance scattering features.

3.1 Origin of the strong magnetic fields

Magnetic fields of neutron stars are among the strongest known magnetic fields in the universe. The magnitude of the magnetic field can be estimated by considering the conservation of the magnetic flux during the collapse of the late type star, which is similar to the magnetic field in a closed loop, where:

$$\Phi = \int \vec{B} \cdot d\vec{l} = \int\int \vec{B} \cdot d\vec{A} \sim B \cdot A = \text{constant} \tag{3.1}$$

with $d\vec{l}$ as the differential length along the closed path enclosing the magnetic field lines $\vec{B}$ on the surface, and $d\vec{A}$ as the differential of area enclosed by the loop. If $d\vec{A}$ represents the size of the magnetic pole (Mészáros, 1992), and the initial B-field of the progenitor star has the strength of 100 G (a typical value for a solar type star, Schatzman et al., 1993), the calculated strength of the magnetic field of a neutron star close to its surface is of the order of $\sim 10^{12-14}$ G. Observations have

shown that a bulk of the known neutron stars have a magnetic field of $\sim 10^{12}$ G (Bhattacharya & Srinivasan, 1995).

Soon after the discovery of the existence of the magnetic fields in neutron stars, theories were proposed on how such a field would evolve over time. Ostriker & Gunn (1969) suggested that magnetic fields in isolated neutron stars decay on time scales of $\sim 10^6$ years due to ohmic dissipation. In contrast, Baym et al. (1969a) argued for much longer decay times, where, for a non superconducting core, the conductivity of the neutron star decays due to ohmic dissipation from electrons scattering on neutrons on a timescale of $\sim 10^{13}$ years, which is larger than the age of the universe. On the other hand, if the interior of the neutron star is indeed superconducting, the magnetic flux vortices would not be able to leave the superconducting region easily and would be trapped for a similarly long time scale (Bardeen & Stephen, 1965). The longer decay time-scales are nowadays backed up by many observations which do not show a significant change in the magnetic field strength over the years (Srinivasan, 1989; Bhattacharya et al., 1992).

Magnetic fields in binary systems show a more complicated behavior. Where the magnetic field of an unperturbed neutron star only decays on very long time scales without an external influence, in binary systems the decay occurs most likely much faster. Srinivasan et al. (1990) suggested that the spin down due to accretion can cause a decay of the magnetic field, where magnetic vortices in the core will move outwards and be annihilated at the boundary layer between the solid crust of the neutron star and the core. A detailed discussion of this phenomenon can be found in Bhattacharya & Srinivasan (1995), Srinivasan et al. (1990), and references therein. Geppert & Urpin (1994) suggested that with sufficient accretion rate the neutron star crust would be heated ($> 10^8$ K, Miralda-Escude et al., 1990), causing the conductivity to diminish and the decay of the magnetic field to accelerate. For large accretion rates over long periods of time (10^{6-7} years), the magnetic field can decay to 10^{-3} to 10^{-5} times its original strength, as observed in many binary sources (Urpin & Geppert, 1995). Bisnovaty-Kogan et al. (1979) suggested that additional hydrodynamical flows on the neutron star surface also can have an influence of the decay of the magnetic field.

As discussed in chapter 1, the magnetic field of a neutron star can couple to the accretion disk which can lead to a change of the pulse period of the neutron star. Although the observed pulse periods vary between a few milliseconds (e.g., A 0538−66, Skinner et al., 1982) up to hundreds of seconds (e.g., X-Per, White et al., 1976), the magnetic field in all these sources is of the order of 10^{12} G. This apparent contradiction can be explained by the relative fast transfer of angular momentum onto the neutron star, whereas the decay of the magnetic field is much slower and proceeds over million of years. The age of binary systems with an evolved companion is dictated by the evolution time of the companion star, which is limited to a few million years in the case of a B star companion. Therefore the magnetic field in such systems simply did not have the time to decay and the neutron star in such systems will most likely have a much weaker field in the future.

3.2 Accretion column

The interaction of the accreted material and the magnetic field is very complex and not fully understood. As discussed in chapter 1, accretion onto the neutron star occurs primarily by the means of Roche Lobe overflow and wind accretion, where the former generally creates an accretion disk around the compact object. The strength of the magnetic field with distance from the center of the dipole can be described by

$$B \sim \frac{\mu}{r^3} \tag{3.2}$$

where the magnetic field with a magnetic moment μ at the distance r can be assumed as a dipole. A more detailed discussion of the assumptions about the magnetic field is given in section 3.5. Far away, the influence of the magnetic field on the accreted matter can be neglected. Closer to the neutron star, the magnetic pressure, which can be described by:

$$P_{\mathrm{mag}} = \frac{\mu^2}{4\pi r^6} \tag{3.3}$$

is increasing rapidly until it dominates the motion of the infalling matter. At this 'magnetospheric radius' r_{m}, also known as the Alvén radius, the material

flow is interrupted and forced to follow the the magnetic field lines, funneling the matter onto the magnetic poles of the neutron star. This transition occurs in the boundary layer, a thin region which also represents the innermost stable radius for the infalling material (see Figure 3.1).

The distance $r_{\rm m}$, where the material attaches to the magnetic field lines, is highly dependent on the accretion geometry and the amount of initial angular momentum. For the case of a pure spherical accretion, the radius can be calculated as:

$$r_{\rm m,s} = 2.9 \times 10^8 B_{12}^{4/7} R_6^{10/7} M_{\rm NS}^{1/7} L_{37}^{-2/7} [\rm cm] \tag{3.4}$$

where B_{12} is the magnetic field in 10^{12} G, R_6 is the radius in 10^6 cm (10 km), $M_{\rm NS}$ is the neutron star mass in $M_\odot$ and L_{37} is the accretion luminosity in 10^{37} ergs s^{-1} (Lamb et al., 1973).

In the case of a thin accretion disk, the equation is slightly more complicated and has to include the viscosity parameter of the disk (α, Shakura, 1973) resulting in a disk magnetospheric radius (Kiraly & Meszaros, 1988):

$$r_{\rm m,d} = 10^8 B_{12}^{40/61} R_6^{104/61} M_{\rm NS}^{-25/61} L_{38}^{-16/61} \alpha^{-2/61} [\rm cm] \tag{3.5}$$

Alternatively, the magnetospheric radius can also be calculated based on the Keplerian velocity $v_{\rm K}$ with $\gamma B_{\rm p}^2 r^2 = \o M v_{\rm K}$, where $\gamma = (B_\phi / B_{\rm p})(\Delta r / r)$ with B_ϕ and $B_{\rm p}$ the azimuthal and radial magnetic field components in the disk, and Δr the width of the transition region. The radius can then be described as (Mészáros, 1992):

$$r_{\rm m,s} = 2.9 \times 10^8 \gamma^{2/7} B_{12}^{4/7} R_6^{10/7} M_{\rm NS}^{1/7} L_{37}^{-2/7} [\rm cm] \tag{3.6}$$

A physical description of the boundary layer and its physics is very complicated, and only specific cases, e.g., a thin Keplerian α disk, have been discussed in the literature (Sunyaev & Shakura, 1986; Popham & Sunyaev, 2001). Material at the magnetospheric boundary layer has two ways in which it can be accreted onto a star: through a funnel stream following the magnetic field lines (Ghosh & Lamb, 1978, 1979a,b) or through plasma instabilities at the boundary layer (Arons & Lea, 1976; Elsner & Lamb, 1977; Shakura et al., 2011). Up to this date the boundary layer is not fully understood. In recent years, Kulkarni & Romanova (2008) used

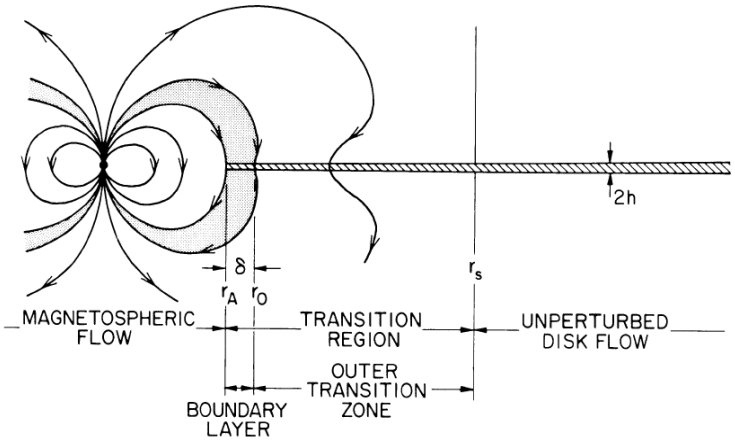

Figure 3.1 Side view of the accretion flow through an accretion disk onto a neutron star. The magnetic field disrupts the disk at the boundary layer, funneling the plasma onto the magnetic poles. From (Ghosh & Lamb, 1978)

3D magnetohydrodynamic simulations which include Rayleigh-Taylor and Kelvin-Helmholtz instabilities at the boundary layer to further study physical processes in this region. These models have only been simulated for a very simple geometry and can still not fully describe more complicated cases.

The distance of the boundary region to the neutron star surface depends strongly on the rotation of the accretion disk. Since the neutron star and its magnetic field can be seen as a solid rotator, the material at the boundary layer will be forced to co-rotate with the neutron star. This material can only co-rotate, when the rotational velocity of the neutron star is smaller than the Keplerian velocity:

$$\omega R < \sqrt{\frac{GM_{\rm NS}}{R}} \tag{3.7}$$

where ωR is the rotation frequency at a specific radius r and $M_{\rm NS}$ is the mass of the neutron star. For a rapidly rotating neutron star, the material cannot couple to the magnetic field lines and no material is accreted from the disk onto the compact object (Pringle & Rees, 1972). In this case, where the neutron star rotates much faster than the material in the disk, the material is expelled by the magnetic field and the inner edge of the disk moves outwards in the so-called propellor effect (Illarionov & Sunyaev, 1975). This effect is very difficult to observe, as sources that show the propellor effect generally cease to accrete material and are therefore

very dim. If the rotation velocity of the neutron star is only slightly higher than the rotation velocity of the material in the boundary layer, an increase in the infalling material increases the ram pressure and the magnetospheric radius decreases. If the accretion decreases again, the magnetosphere expands and the accretion flow on the compact object shuts off. Such a process can explain the behavior of some Be/X-ray binaries which are not observed outside of periastron.

For a system where the magnetic field co-rotates with the accretion disk, the material is coupled to the magnetic field lines in the boundary layer and is accreted onto the neutron star. The free-falling material follows the magnetic field lines and forms the tall accretion column, which can reach a height of multiple kilometers (Basko & Sunyaev, 1976). Material reaching the neutron star surface at the polar caps can form an accretion mound, where bremsstrahlung and black body radiation is produced. These accretion mounds have a size of $\sim 1\,\mathrm{km}$ (Lamb et al., 1973), assuming that the field lines close to the poles are undistorted dipole lines. The material close to the neutron star encounters a very extreme environment, with strong magnetic fields of $10^{12}\,\mathrm{G}$, large gravity and extreme temperatures. At these strong magnetic fields, radiative transfer and radiation hydrodynamics have to be taken into account when describing the accretion. The strong gravitational field requires a fully relativistic treatment, making a self-consistent model of the accretion process very complicated. Some of these problems have been addressed in the past (see, e.g., Nagel, 1981b,a; Harding et al., 1984; Burnard et al., 1990, and references therein) but a full description of the different observed spectra and light curves is still lacking.

Basko & Sunyaev (1976) proposed two different models for the accretion geometry, which are widely used in modern simulations (see Fig. 3.2). For smaller accretion rates, the hollow cylinder geometry applies and only a narrow range of the magnetic field lines is coupled to the disk, sweeping away the material from the accretion disk before it can get closer to the neutron star. Because the material is locked into the magnetic field lines, it will stay on the initial field line and accrete as a hollow cylinder onto the magnetic pole of the neutron star. The walls of the hollow cylinder are thin compared to the size of the polar cap.

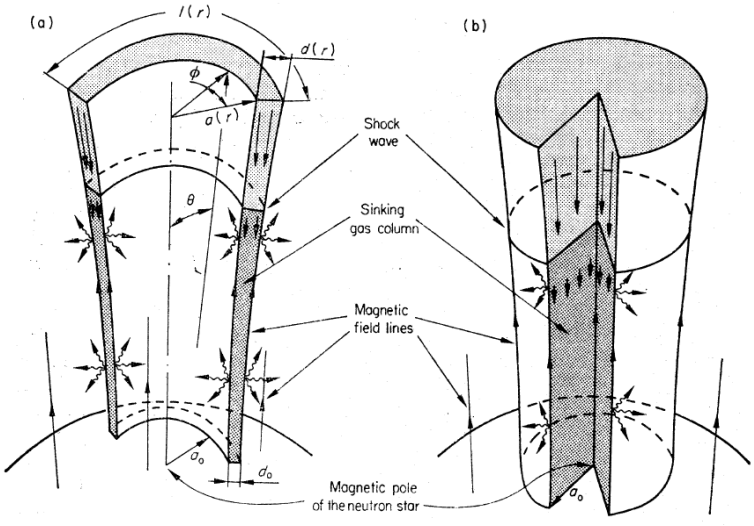

Figure 3.2 Two different accretion column geometries of a neutron star. The left side shows the hollow accretion column where material is funneled in a narrow hollow cylinder onto the neutron star. The right size shows the accretion for a filled cylinder. From Basko & Sunyaev (1976).

For higher accretion rates, or if the material is accreted spherically such as in wind accretors, the material will couple to different magnetic field lines and form a more solid cylinder as an accretion column. Depending on the accretion rate, the material can reach supersonic speeds approaching the speed of light (King, 1995). The free falling material can create shock regions above the polar caps (Zel'Dovich & Shakura, 1969; Shapiro & Salpeter, 1975), where the density increases and where the individual X-ray photons can be up-scattered. Inhomogeneities in the accretion stream will have a time-dependancy, where the matter falls as individual blobs onto the neutron star. These blobs are highly elongated along the magnetic field lines (Hameury et al., 1980).

The emission geometry and the position of the possible shock region depends strongly on the accretion rate. The shock region is formed above the accretion mound and can be multiple neutron star radii above the surface. Not much is known about the shock, but according to Harding (1994) it is most likely collisionless, as the mean free path of the emitted photons for a collisional shock is much larger than the neutron star itself (Mészáros, 1992). The supersonic material is decelerated in the shock region and then slowly sinks in a cylindrical geometry

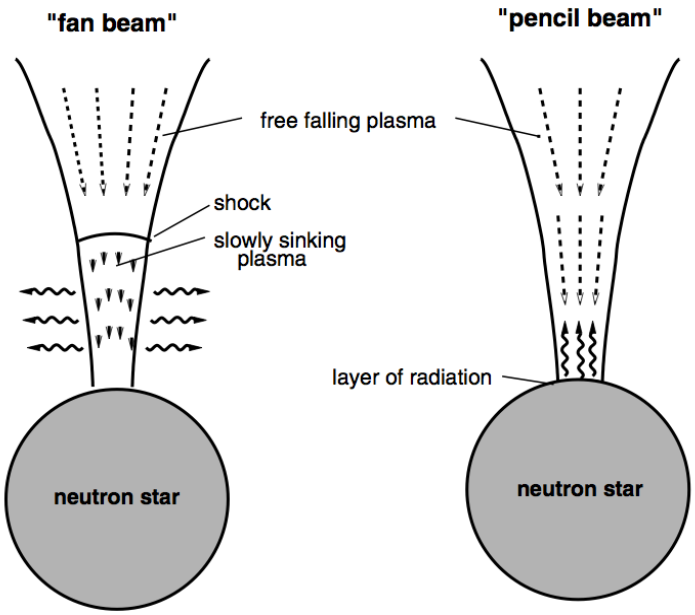

Figure 3.3 Different emission geometries in a neutron star system. With a shock region (left) the material sinks slowly on the neutron star surface, emitting photons to the sides. If no shock is formed, material falls onto the neutron star, and the photon emission occurs primarily along the magnetic axis. From Schönherr et al. (2007) after Harding (1994).

onto the neutron star, radiating X-ray photons. Because the accretion column is almost opaque to the X-rays, only photons close to the edge of the column can escape. The X-rays leave mostly perpendicular to the sinking matter, resulting in a broad emission geometry, the so-called fan beam (Figure 3.3, left).

For smaller accretion rates, the material falls directly to the neutron star surface onto the accretion mound and is either stopped by Coulomb interaction at the accretion mound (Kirk & Galloway, 1981; Kirk & Stoneham, 1982) or by a classical gas-shock very close to the neutron star surface. X-ray photons are produced in this slab geometry by thermal bremsstrahlung and Compton cooling. The emitted photons are collimated in a narrow emission beam along the magnetic pole axis, forming the so-called pencil beam (Figure 3.3, right)

3.3 Continuum models

Understanding the broad band continuum of a source is essential, especially when searching for features such as the CRSF. Up to this date, no coherent physical model has been found to describe the different shapes of the continuum in accreting X-ray pulsars (see Harding, 1994, and references therein). Historically, the observed spectra have been described with empirical models, where the general shape follows an absorbed power law with a cutoff at higher energies. Titarchuk & Hua (1995) introduced an analytical and Monte Carlo simulated model based on photon Comptonization (`compTT`), which was successfully used to describe the spectral shape in some X-ray binaries, but could not fully describe the spectrum in others. In more recent years, Becker & Wolff (2007) developed a more physical model based on bulk or dynamical Comptonization of photons due to collisions in compressed gas in the accretion column assuming the process of first order Fermi energization.

Although the empirical continuum model of an X-ray binary generally can be described with a simple cutoff power law, the underlying physics is more complicated. Katz (1976) and Shapiro et al. (1976) were the first to show that the power law spectra are a result of Comptonization of emitted X-ray photons in the vicinity of the neutron star, i.e., bremsstrahlung and black body radiation. Titarchuk & Lyubarskij (1995) later showed that the power law spectral shape is an exact solution for the radiative kinetic equation for an high energy photon injected in the accretion column.

This section describes the three commonly used empirical models, as well as the more physical `compTT` and Becker-Wolff models.

3.3.1 PLCUT

One of the historically most commonly used models for a pulsar continuum is the power-law with a high-energy cutoff (`highecut`, White et al., 1983) with

the form[1]:

$$PLCUT(E) = AE^{-\Gamma} \times \begin{cases} 1 & \text{for } E \leq E_{\text{cut}} \\ e^{-(E-E_{\text{cut}})/E_{\text{fold}}} & \text{for } E > E_{\text{cut}} \end{cases} \tag{3.8}$$

where Γ, E_{cut}, and E_{fold} are the power law index, cutoff energy, and folding energy, respectively. The cutoff energy indicates where the spectrum turns from a regular power law to a steeper, curved model. The PLCUT model shows a sharp discontinuity at the cutoff energy which does not occur in natural phenomena and can create artificial residuals around the cutoff energy that mimic the appearance of a broad emission or absorption line. Therefore this model is generally not suited for a physical interpretation and is often only used for a comparison with historical data.

3.3.2 FDCUT

The Fermi-Dirac (FD) cutoff model was proposed by Tanaka (1986) and can be described by:

$$FDCUT(E) = AE^{-\Gamma} \frac{1}{1 + e^{(E-E_{\text{cut}})/E_{\text{fold}}}} \tag{3.9}$$

This description allows a smooth, continuous turnover at the cutoff energy. The cutoff and folding energies in this model are technically very similar to the components in the power law with a high energy cutoff (`highecut`), but describe the spectrum differently, so that the model parameter values cannot be directly compared. The FD-cutoff model is based on the Fermi-Dirac distribution in statistical mechanics, but is used solely for its analytical shape of the spectrum and is not based on its physical interpretation.

3.3.3 NPEX

A third analytical model was introduced by Mihara (1995) and describes the unabsorbed continuum with a Negative and Positive power-law Exponential

[1] A very similar model, called `cutoffpl` can be also found in the XSPEC library, where in this case the curving begins at 0 keV. In the case of 1A1118−61, the cutoff energy in the `highecut` component was close to 0, making the PLCUT effectively a `cutoffpl`.

(NPEX). This model also avoids a discontinuity at the cutoff energy and is described by:

$$NPEX(E) = A(E^{-\Gamma_1} + BE^{+\Gamma_2})e^{-E/E_{\rm fold}} \tag{3.10}$$

where Γ_1 and Γ_2 are the negative and positive power-law exponentials, and $E_{\rm fold}$ describes the folding energy. The NPEX model is very flexible but did not show any improvements to the other models used in our analysis.

3.3.4 CompTT

This analytical model describes the Comptonization of soft photons in a hot plasma and includes relativistic effects (Titarchuk, 1994; Titarchuk & Hua, 1995). It can be applied in both optically thin and thick regimes and the spectrum is determined by 5 parameters: the redshift, the seed photon and plasma temperatures, the optical depth of the plasma, and the geometry. Due to the high complexity of this model, the allowed parameter space is not very well constrained, and has to be carefully considered for a physical interpretation (Hua & Titarchuk, 1995) . The advantage of this model is the use of physical parameters, which lead directly to an interpretation of the data.

I apply the `CompTT` model in the analysis of the X-ray Binary 1A1118−61 (Chapter 5), where the *Suzaku* and *RXTE* data are compared.

3.3.5 Becker-Wolff

In more recent years, a more physical model was developed by Becker & Wolff (2005a,b, 2007) based on bulk and thermal Comptonization of photons by a shock in the accreted gas. Earlier physical models (e.g., Nagel, 1981b; Meszaros & Nagel, 1985a,b) were not capable of fully describing the observed spectra. The Becker & Wolff model is based on calculating and convolving Green's function terms of the transport equations, based on bremsstrahlung, cyclotron and black body emission sources. Seed photons are created by thermal black body emission of the thermal mound at the bottom of the accretion column (Davidson & Ostriker, 1973). In the bulk Comptonization, kinetic proton energy is transfered to the

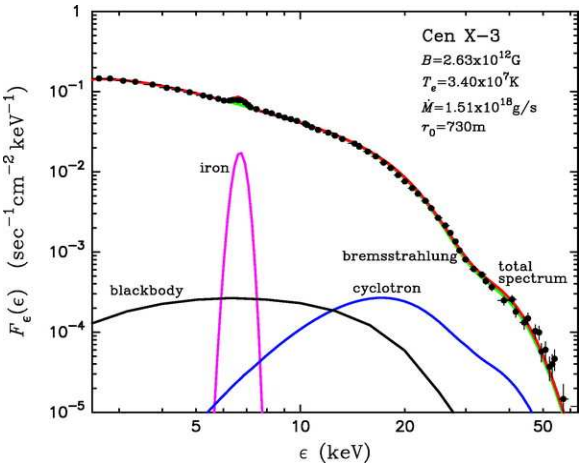

Figure 3.4 Theoretical flux/spectrum based on the Becker-Wolff model compared with the Beppo-Sax Cen X-3 observations from Burderi et al. (2000). The plot includes the overall spectrum, as well as the bremsstrahlung, cyclotron emission and blackbody components. An additional iron emission line is also included. From (Becker & Wolff, 2007).

photons, a process which mostly dominates at lower electron temperatures ($< 10^7$ K). The pure bulk description does not invoke the high-energy cutoff, a common feature in many X-ray binaries. The thermal Comptonziation is introduced to provide the high energy-cutoff and the general spectral shape of the spectrum. The final spectrum consists of the sum of these three individual components. Figure 3.4 shows an example of this model and its components with Cen X-3 *Beppo-SAX* data from Burderi et al. (2000).

With a typical neutron star mass of $\sim 1.4\,M_\odot$ and a stellar radius of 10 km, this model can be constrained with 6 physical parameters: accretion rate $\dot{M}$, column radius r_0, electron plasma temperature T_e, magnetic field strength B, photon diffusion parameter ξ and the Comptonization parameter δ (see Becker & Wolff, 2007, for details)

Although the model was applied successfully to a limited number of sources, e.g. Her X-1, Cen X-3, LMC X-4 (Becker & Wolff, 2007), and 4U0115+63 (Ferrigno et al., 2009), the model is not yet available to the public and still lacks some aspects for a fully physical interpretation. Therefore this model has not been applied to the data presented in this thesis.

3.4 Cyclotron Resonance Scattering Features

Electrons in a uniform magnetic field can travel freely along the magnetic field lines, but are constrained to circular motion when traveling perpendicular to the magnetic field. This helical motion can be observed in the laboratory, where the moving electrons circle in a magnetic field with the Larmor frequency of:

$$\omega_{\mathrm{Larmor}} = \frac{v_\perp}{r} = \frac{e}{m_\mathrm{e}} B \tag{3.11}$$

where $v_\perp$ is the perpendicular velocity of the electron in the magnetic field B. This frequency is also called cyclotron frequency, due to the circular motion of the charged particle in the magnetic field. The radius of this gyration can then be derived as:

$$r_{\mathrm{Gyration}} = \frac{m v_\perp}{eB}. \tag{3.12}$$

For very strong magnetic fields, such as fields close to the neutron star surface, the gyration radius becomes similar to the de Broglie wavelength:

$$r_{\mathrm{Gyration}} = r_{\mathrm{de\ Broglie}} = \frac{\hbar}{mv} \tag{3.13}$$

so that quantum effects become non negligible. In such a regime, the perpendicular motion of the electrons is quantized and is described by individual Landau levels (see, e.g, Lai, 2001, and references therein):

$$E_\mathrm{n} = m_\mathrm{e} c^2 \sqrt{1 + \left(\frac{p_\parallel}{m_\mathrm{e} c}\right) + 2n \frac{B}{B_{\mathrm{crit}}}} \tag{3.14}$$

where n is the quantum number of the individual Landau level, $p_\parallel$ is the momentum of the electrons parallel to the magnetic field, and B_{crit} is the critical magnetic field strength ($\sim 4.4 \times 10^{13}\,\mathrm{G}$), where the Gyration radius is below the de Broglie wavelength. For $B << B_{\mathrm{crit}}$, the energy between two Landau levels is described by the cyclotron energy:

$$E_{\mathrm{cyc}} = \hbar\omega = \frac{\hbar B}{m_\mathrm{e} c} \approx 11.6 \times \frac{B}{10^{12}\mathrm{G}} [\mathrm{keV}] \tag{3.15}$$

which can be easily remembered in the form of the **12-B-12**-rule. Measuring the mean energy of the cyclotron line can then be used to calculate the magnetic field in the vicinity of the neutron star.

A photon with the cyclotron energy $E_{\rm cyc} = h\nu$ can interact with an electron in the magnetic field by exciting the electron from its present Landau level n to the next higher level $n + 1$. The electron de-excites to its original state shortly after with a decay rate of (Latal, 1986):

$$\nu_{\rm r} = \left(\frac{\alpha m_{\rm e} c^2}{\hbar}\right)\left(\frac{B}{B_{\rm crit}}\right)^{1/2} \tag{3.16}$$

by emitting a photon with the same energy in a random direction. In this equation, $\alpha = 1/137$ is the fine structure constant. Because only a small fraction of the electrons is being emitted into the original direction, an outside observer measures a lack of photons at the cyclotron energy. For the typical magnetic fields of a neutron star (10^{12} G), the decay rate of the excitation is $\nu_{\rm r} \sim 10^{15}$ Hz, so that the electrons are almost instantly de-excited, very similar to a scattering process. Therefore the observed feature is also commonly referred to as a Cyclotron Resonance Scattering Feature (CRSF).

For photons with much higher energies, an electron can be excited into a higher energy state (Δn >1) and de-excite through different Landau levels in a cascade of multiple photons. This process is called photon spawning and is the preferred decay channel in sources where the magnetic field is $B < B_{\rm crit}$. Because additional photons are created at the fundamental cyclotron energy, the spawned photons can partially fill up the fundamental line. Therefore it is not unusual for the first harmonic to be deeper than the fundamental line.

Since the de-excitation time is so short, most electrons mainly populate the energetic ground level ($n = 0$). As photons of the energy $n \times E_{\rm cyc}$ are created during the de-excitation process, it was believed at first that this process would result in emission at $E_{\rm cyc}$ in the spectrum (Meszaros et al., 1977; Yahel, 1977). The first cyclotron feature was observed in Her X−1 by Trümper et al. (see Fig.3.5, 1978) where it was initially interpreted as an emission feature. Shortly after the discovery, Herold (1979) showed that the mean free path of the created photons is so small that the photons are reabsorbed by a close electron before they can leave the plasma. Photons are only capable to escape if they are at the edge of the infalling plasma or if their energy has changed due to the numerous scattering processes so that the free mean path increased. Up to this date, CRSFs have

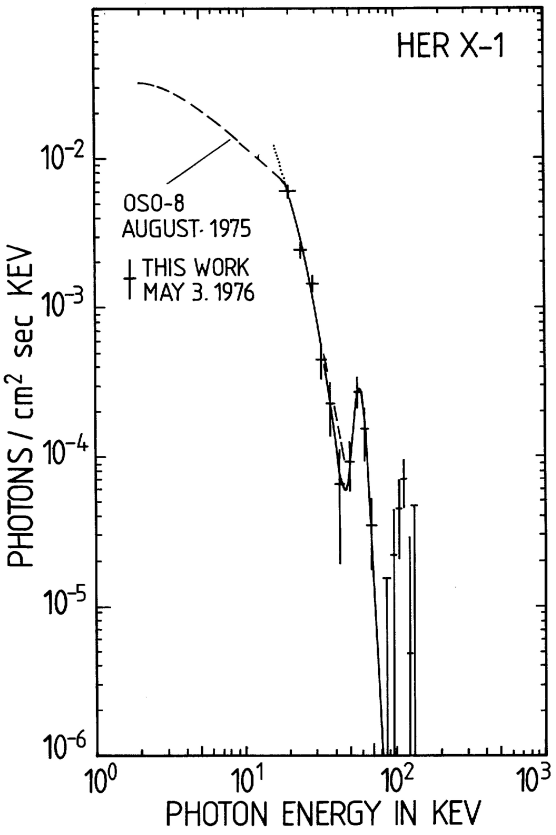

Figure 3.5 First detection of a CRSF in Her X-1 from the UHURU satellite. It was assumed that the CRSF is an emission line, but shortly after the detection it was established that the CRSF is in fact an absorption line. From Trümper et al. (1978) .

been observed in 17 X-ray Binaries, where the fundamental line energies vary from $\sim 14\,\mathrm{keV}$ (4U 0115+63, Heindl et al., 1999) up to $\sim 50\,\mathrm{keV}$ in A0535+26 (Kendziorra et al., 1992) and $\sim 55\,\mathrm{keV}$ in 1A1118−61 (Suchy et al., 2011b) (see tables 3.1 and 3.2 for details). LMC X-4 has a possible line at 100 keV (La Barbera et al., 2001), which has not been confirmed in other observations.

Table 3.1. List of known persistent CRSF sources

Name	E_{CRSF} [keV]	P_{Spin} [s]	P_{Orb} [d]	Companion	Discovery Paper
4U 1907+09	18, 38	441	8.37	B2 III-IV	BeppoSAX (Cusumano et al., 1998)
4U 1538-52	22, 47	530	3.7	B0I	*Ginga* (Clark et al., 1990), *RXTE* (Rodes-Roca et al., 2009)
Vela X-1	24, 52	283	8.96	B0.5Ib	*Mir-HEXE* (Kendziorra et al., 1992), *RXTE* (Kreykenbohm et al., 2002)
Cen X-3	29	4.8	2.09	O6.5II	*BeppoSAX* (Santangelo et al., 1998), *RXTE* (Heindl et al., 1999)
X Per	29	837	250.3	B0 IIIVe	*RXTE* (Coburn et al., 2001)
4U 1626-67	37	7.66	0.028	WD?	*BeppoSAX* (Orlandini et al., 1998), *RXTE* (Heindl et al., 1999)
GX 301-2	37	690	41.5	B1.2Ia	*Ginga* (Mihara, 1995)
Her X-1	41	1.24	1.7	A9-B	*Ballon-HEXE* (Trümper et al., 1978)

Table 3.2. List of known transient CRSF sources

Name	$E_{\rm CRSF}$ [keV]	$P_{\rm Spin}$ [s]	$P_{\rm Orb}$ [d]	Companion	Discovery Paper
Swift J1626.6-5156	10	15.4	132.9	Be	*RXTE* (DeCesar et al., 2011)
4U 0115+634	14, 24, 36, 48, 62	3.6	24.3	Be	*HEAO-1* (Wheaton et al., 1979), *RXTE* (Heindl et al., 1999), *BeppoSAX* (Santangelo et al., 1999)
V 0332+53	27, 51, 74	4.37	34.25	Be	*Ginga* (Makishima et al., 1990)
Cep X-4	28	66.25	> 23	B1	*Ginga* (Mihara et al., 1991)
MXB 0656-072	33	160	100?	O9.7Ve	*RXTE* (Heindl et al., 2003)
XTE J1946+274	36	15.8	169.2	B0-1V-IVe	*RXTE* (Heindl et al., 2001)
A0535+26	45, 100+	104	110.6	Be	*Mir-HEXE* (Kendziorra et al., 1992, 1994), *CGRO* (Maisack et al., 1997)
GX 304-1	54	272	132.5	B2 Vne	*RXTE* (Yamamoto et al., 2011)
1A1118-61	55, 110?	408	400-800?	O9.5IV-Ve	*RXTE* (Doroshenko et al., 2010b), *Suzaku* (Suchy et al., 2011b)
GRO J1008-57	88?	93.5	247.8	B1-B2	*CGRO* (Shrader et al., 1999)

The exact location of the X-ray emission region is uncertain and strongly depends on the accretion geometry, accretion rate and other parameters. Also it is uncertain if the region of the CRSF is consistent with the emission region of the X-ray continuum or the shock region. It is generally assumed that the CRSF is created somewhere in the accretion column, close to the neutron star surface, so that the magnetic field can be calculated from the measured CRSF. All indications, however, point to the CRSF production region being located close to the shock region.

Variations of the CRSF centroid energy have been observed throughout the pulse phase, e.g., Her X-1 (Gruber et al., 2001), Vela X-1 (Kreykenbohm et al., 2002), 4U 1538−52 (Clark et al., 1990), and GX 301-2 (Kreykenbohm et al., 2004; Suchy et al., 2011a). In addition, many of these sources also show a luminosity dependence of the CRSF. A negative centroid energy-luminosity correlation has been found in V 0332+53 and 4U 0115+63 (Tsygankov et al., 2006; Nakajima et al., 2006), whereas a positive luminosity correlation was found in Her X-1 (Staubert et al., 2007). Other sources, i.e., A0535+63 (Caballero, 2009), do not show variations throughout large luminosity ranges.

As a critical luminosity is thought to separate positive and negative correlations (Staubert et al., 2007, Becker et al., in prep.) it is important to understand what processes occur in each of these cases. For sources above the critical luminosity, the material creates a radiation-dominated shock in the accretion column, where the material is slowed down and slowly sinks to the neutron star surface. X-rays are emitted from the sides of the accretion column in the form of a fan beam. When the accretion rate increases, the shock region moves higher up in the accretion column, where the magnetic field is weaker. So, for a CRSF emission region close to the shock region, the CRSF centroid energy decreases with increasing luminosity. For sources below the critical luminosity the material falls directly onto the neutron star surface and results in X-ray emission in the form of a pencil beam. In this scenario an increase of the accretion rate can force the Coulomb deceleration in an 'atmosphere' near the accretion mound or the gas-mediated shock closer to the neutron star surface, where the magnetic fields are stronger. In such

a case, the CRSF centroid energy would increase with an increasing luminosity.

With the emission so close to the neutron star surface, gravitational redshift also plays a significant role and influences the measured CRSF centroid energy:

$$E_{\rm cyc}^{\rm obs} = \frac{E_{\rm cyc}}{1+z} \tag{3.17}$$

where z is the gravitational redshift and is

$$z \approx \frac{1}{\sqrt{1-\frac{2GM_{\rm NS}}{Rc^2}}} - 1 \approx 0.3 \tag{3.18}$$

for a typical neutron star with $M_{\rm NS} \approx 1.4 M_{\odot}$.

To further complicate the picture, the Landau levels are not fully equidistant in the relativistic regime. The CRSF also depends on the angle between the magnetic field lines and path of the absorbed photon Θ (Harding, 1994; Harding & Daugherty, 1991). A more detailed equation to describe the CRSF energy is:

$$E_n = \frac{m_{\rm e}c^2}{\sin^2\Theta}\left(\sqrt{1+2n\frac{B}{B_{\rm crit}}\sin^2\Theta} - 1\right) \tag{3.19}$$

where the dependence of CRSF fundamental and harmonic energies on Θ leads to an uneven spacing. Since these energies are nontrivially dependent on the photon's propagation angle with respect to the field, the observed spectral features are influenced by the plasma geometry and the internal orientation of the magnetic field.

3.4.1 Gabs

The most common empirical model to describe a CRSF is a simple negative exponential Gaussian line with an optical depth as the amplitude:

$$f(E) = e^{(-\tau/\sqrt{2\pi}\sigma)e^{-0.5((E-E_{\rm cyc})/\sigma)^2}} \tag{3.20}$$

where $E_{\rm cyc}$ is the centroid energy of the CRSF, σ is the width, and τ the optical depth. This model is implemented in XSPEC as the multiplicative model `gabs` and is multiplied by the continuum. It can describe a majority of observed CRSFs, and is applied in most publications. In this thesis I primarily use the `gabs` model to model the observed CRSF.

3.4.2 Cyclabs

A second common empirical model is the pseudo Lorentzian shaped cyclotron absorption line (XSPEC model `cyclabs`) which has the form:

$$f(E) = exp[-\tau_{\rm cyc}\frac{(\sigma_{\rm cyc}E/E_{\rm cyc})^2}{(E-E_{\rm cyc})^2+\sigma_{\rm cyc}^2} + \tau_{\rm H}\frac{(\sigma_{\rm H}E/2E_{\rm cyc})^2}{(E-2E_{\rm cyc})^2+\sigma_{\rm H}^2}] \tag{3.21}$$

This model was introduced by Mihara et al. (1990) and Makishima et al. (1990), and models simultaneously the fundamental cyclotron line (cyc) as well as the first harmonic (H) at twice the energy of the fundamental. To use this model in sources where only the fundamental line is observed, such as the sources in this thesis, $\tau_{\rm H}$ has to be fixed to 0. The fact that the energy of the harmonic line is fixed to twice the energy of the fundamental line increases the number of degrees of freedom by one. But it also leads to problems when modeling the data since, as we have shown earlier, not all lines are equidistant and the first harmonic will therefore not always be at exactly twice the energy.

The energies obtained by the `cyclabs` model are $\sim 10-20\%$ below the centroid energies obtained by the `gabs` model. The discrepancy between the `cyclabs` and `gabs` model is explained by the way the centroid energy is calculated in each model. In the `cyclabs` model the width, which accounts for $\sim 10-20\%$ of the line energy, is included in the shape, moving the obtained energy values towards lower energies (Nakajima et al., 2010, and references therein)

3.4.3 Physical CRSFs

Similar to the first continuum models, the two previously discussed models are only an empirical attempt to describe the observed CRSF and do not address asymmetrical or more complex line shapes. Kreykenbohm et al. (2005), Pottschmidt et al. (2005), and Nakajima et al. (2010) showed in the case of V 0332+53 that the line shape is sometimes more complex and cannot be modeled with a simple Gaussian or Lorentzian profile. In these cases, the fundamental line was modeled with a combination of two `gabs` or a `cyclabs-gabs` combination with similar energies. To better understand the physics involved in the formation of the CRSF, a fully physical model is necessary.

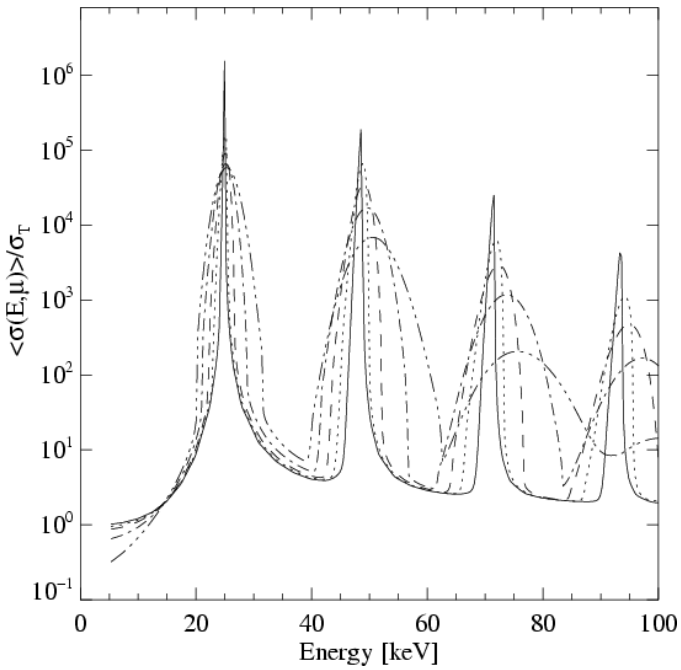

Figure 3.6 Cross sections for a magnetic field of $\sim 2.2 \times 10^{12}$ G and an electron temperature of $kT_{\rm e} = 3$ keV in units of Thompson cross section $\sigma_{\rm T}$. The different profiles indicate different angles of propagating photons with respect to the magnetic field vector, between $\cos\Theta = 0.005$ (solid line) and $\cos\Theta = 0.875$ (broadest dash-dotted line). From Schönherr et al. (2007) based on Araya & Harding (1999).

To achieve such a physical model, Araya & Harding (1999) calculated the relativistic magnetic Compton-scattering cross sections for electrons in magnetic fields, where they varied the angle between the field and the traveling electron, Θ, for a fixed magnetic field strength (Figure 3.6). The individual peaks of the cross sections occur at the individual Landau energies, where the electrons absorb and re-emit the photons from the X-ray continuum. These cross sections were used in an early model, which calculated the propagation of photons through different geometries, i.e., a slab and cylinder, where seed photons are created within a constrained emission region and then are modeled on their way through the material until they escape. The escaped photons then form the observed spectrum (Araya & Harding, 1999; Araya-Góchez & Harding, 2000). Due to the simplicity of the model and the dependence on the continuum, which provides the seed photons for the propagation, only specific cases could be modeled with this code.

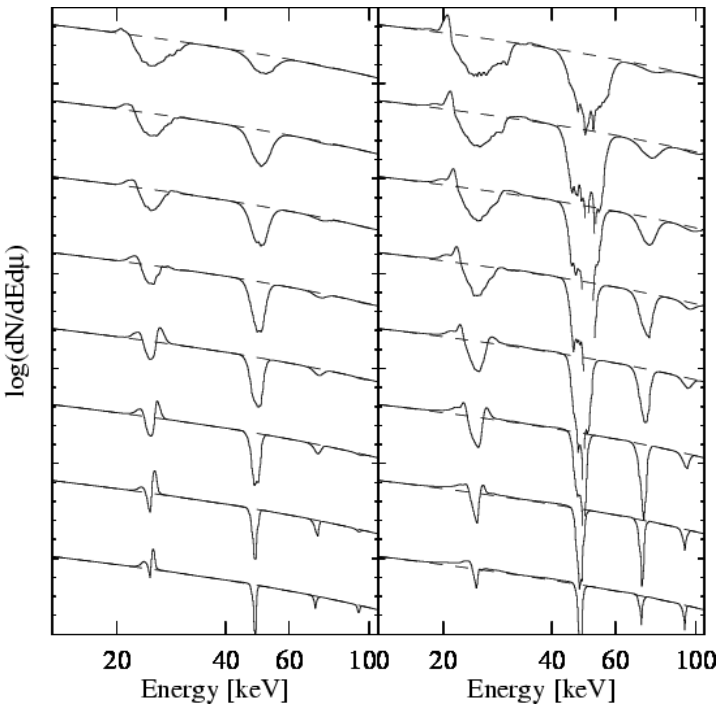

Figure 3.7 Different CRSF line profiles for a cylinder geometry as a function of observation angle and optical depth τ. Left: $\tau = 3 \times 10^{-4}$; Right: $\tau = 3 \times 10^{-3}$. The continuum has a power law distribution with $\Gamma = 2$ with an exponential cutoff at $E_{\rm cut} = 40\,{\rm keV}$. The 8 profiles indicate the different viewing angle cosΘ from 0 - 1 (bottom to top). From Schönherr et al. (2007).

Based on the work of Araya & Harding (1999), Schönherr (2007) improved upon their code using a Green's function approach, which made the model independent of an assumed continuum model. Using a Monte Carlo method, Schönherr (2007) calculated the Green's functions for a variety of different parameter combinations. Based on these pre-calculated Green's function tables, the model is able to generate output models for the CRSF based on input photons from any given continuum for a large parameter space. The model is also capable of easily comparing the slab and cylindrical geometry, and can use different geometries, depending where the seed photons from the continuum are created. The model was implemented in XSPEC and was tested on multiple sources, such as V 0332+53 (Schönherr et al., 2007) and Cen X-3 (Suchy et al., 2008)

The model confirmed that the line shapes of the CRSF are rather complex and cannot always be easily modeled by a simple shape, such as the previously

discussed `gabs` or `cyclabs` model (Figure 3.7). The results of this model were very promising, but still showed some unexplained and unobserved features, such as emission wings around the CRSF and very strong features at the centroid energy. A possible explanation is that the assumed B-fields in the model are uniform, whereas the B fields in the CRSF-generating region have intrinsic gradients due to the physical size of the region, which would smear out these features. In addition, the authors of Schönherr et al. (2007) found a problem in their code, that caused some of the original cross section profiles to be off by a factor of ~ 2, thus reducing the mean free paths and increasing the number of scattering events in the medium.

Based on the work of Schönherr et al. (2007), Schwarm (2010) corrected the code and incorporated an improved method to calculate the mean free path length from interpolation instead of Monte-Carlo simulation. At this time, the code has not yet been fully implemented for the full parameter space and was therefore not applied to the data presented in this thesis. Future work will include the implementation of a B-field gradient and a possible merging with the previously discussed physical continuum model by Becker & Wolff (2007).

3.5 Geometrical dipole model

Assuming a simple dipole magnetic field around a spherical neutron star, and taking the viewing angle and the misalignment of the magnetic dipole to the spin axis into account, I can use a geometrical discussion to model the variation of the CRSF energy throughout the pulse phase. A displacement and a misalignment of the two magnetic poles can also be included in the model.

I use this model for both, Cen X-3 (chapter 4) and GX 301−2 (chapter 6) to discuss the observed variations throughout the pulse phase.

The total magnetic moment μ of the neutron star can be calculated with:

$$\langle \mu \rangle = B \cdot R_{\mathrm{NS}}^3 \langle \sqrt{1 + 3\cos^2 \Phi} \rangle \tag{3.22}$$

using the average magnetic field from the phase averaged CRSF centroid energy and a typical neutron star radius of $R_{\mathrm{NS}} = 10\,\mathrm{km}$. The value of the last part,

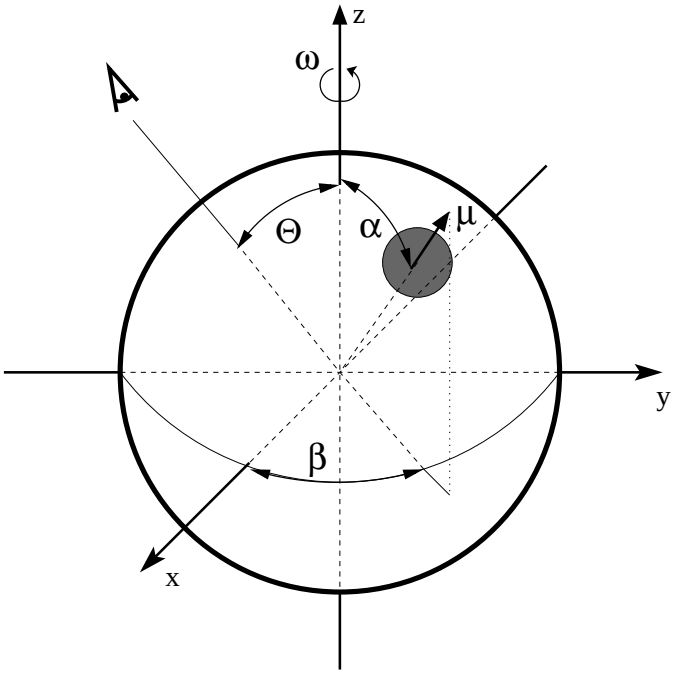

Figure 3.8 Schematic view of the dipole model, indicating the different angles used to calculate the CRSF energy variation.β is the angle between the projection of the magnetic moment in the x-y-plane and the ephemeris (x-axis) .The eye indicates the line of sight towards us.

including the azimuthal angle Φ of the magnetic pole was estimated to the average value of 1.54.

The total average magnetic moment is divided into three components based on the cartesian coordinate system in Figure 3.8:

$$\mathbf{m} = \mu \begin{pmatrix} \sin(\alpha)\cos(\beta) \\ \sin(\alpha)\sin(\beta) \\ \sin(\beta) \end{pmatrix} \tag{3.23}$$

where α is the angle between the dipole field and the spin axis and β is the rotation angle from the ephemeris, i.e. the x-axis. Next, the vector $\mathbf{n}$ was calculated for each individual phase bin ϕ used in the phase resolved analysis.

$$\mathbf{n} = \begin{pmatrix} \sin(\Theta)\cos(\phi) \\ \sin(\Theta)\sin(\phi) \\ \sin(\phi) \end{pmatrix} \tag{3.24}$$

The individual components of $\mathbf{n}$ are the projections of each phase bin on the three axes, as seen from the line of sight of the observer. The angle Θ corresponds to the angle between the line of sight and the spin axis. For each of the individual phase bins, the magnetic field was calculated using the position vector $\mathbf{n}$ indicating the position of the magnetic pole and the vector $\mathbf{m}$, which indicates the magnetic moment:

$$B_{\text{phase}} = \frac{3 \cdot \mathbf{n} \left| \mathbf{m} \cdot \mathbf{n} \right|}{\left| \mathbf{n} \right|^5} - \frac{\mathbf{m}}{\left| \mathbf{n} \right|^3} \tag{3.25}$$

The calculated magnetic field values were then fitted to the measured magnetic field, varying the three angles Θ, α, and β until the fit converged. To avoid wrong solutions due to local minima, the starting parameter of all three angles were varied in steps of 10° before the fit was started.

Chapter 4

Cen X-3

4.1 Overview

Cen X-3 is the third discovered X-ray source in the Centaurus constellation and the first X-ray pulsar discovered (UHURU, Schreier et al., 1972; Giacconi et al., 1971a). The pulse period was established with 4.8 s and the orbital period was measured as ~ 2.1 days. The binary system consists of a neutron star with a mass of $1.21 \pm 0.21\, M_{\odot}$ accompanied by an O 6.5 II supergiant star with a mass of $20.5 \pm 0.7 M_{\odot}$ (Hutchings et al., 1979; Ash et al., 1999). The distance of the binary system has been estimated to be roughly 8 kpc with a lower limit of 6.2 kpc (Krzeminski, 1974) and the eccentricity is found to be ≤ 0.0016 (Bildsten et al., 1997). Day & Tennant (1991) used dust scattering measurements to derive a distance of 5.4 ± 0.3 kpc, a result only marginally consistent with Krzeminski (1974) within given uncertainties. Thompson & Rothschild (2009) also used a dust scattering method on *XMM-Newton* data and calculated a distance of 5.7 ± 1.5 kpc, with the caveat that a majority of the dust is in the vicinity of the solar system, making the dust scattering approach very unreliable. In order to allow for easier comparison with earlier publications I will adopt the widely used distance of 8 kpc. HMXBs generally show a strong stellar wind which can supply a continuous tidal stream to the compact object when the companion star is close to filling its Roche lobe (Petterson, 1978; Stevens, 1988; Blondin et al., 1991). Day & Stevens (1993) discussed that in a system like Cen X-3 an X-ray excited wind would be sufficient

as a possible mechanism for mass transfer able to sustain a constant mass flux. In addition evidence for an accretion disk can be found: Tjemkes et al. (1986) compared the observed light curve of Cen X-3 with modeled binary light curves and achieved best results when including an accretion disk. The observed overall spin-up trend of 1.135 ms/yr with fluctuations on timescales of a few years (Tsunemi et al., 1996) also indicates the presence of an accretion disk, attributed to Roche lobe overflow. A realistic picture of the mass transfer mechanism in this source would therefore be a combination of disk accretion with an excited stellar wind, as proposed by Petterson (1978). An example of a system with a combined mass transfer mechanism is, e.g., GX 301-2 (Leahy, 2002; Leahy & Kostka, 2008), which will be discussed in more detail in chapter 6.

An absorption feature in the X-ray spectrum at ∼30 keV, interpreted as a cyclotron resonance scattering feature (CRSF), was first observed in Cen X-3 with *Ginga* by Nagase et al. (1992). *BeppoSAX* and *RXTE*/HEXTE confirmed this feature at 28 keV and 30 keV, respectively (Santangelo et al., 1998; Heindl et al., 1999). It is assumed to be the fundamental line and so far no higher line harmonics have been observed for this source. Using the previously discussed 12-B-12 method, and correcting for the gravitational redshift of ~ 0.3 for a typical neutron star, the calculated magnetic field is $\sim 3.4 \times 10^{12}$ G for a CRSF centroid energy of ~ 30 keV

Kohmura et al. (2001) analyzed the PCA data of this observation in the energy band $2-13$ keV with a high time resolution of 15.625 ms. They saw a delay in the time variability of the iron K band by 0.39 ± 0.10 ms, and concluded that these photons were reprocessed away from the neutron star and are probably part of the matter accreting onto the NS. In addition to the prominent Kα emission line, Iaria et al. (2005) discovered an additional Fe XXXV emission triplet at the energies of 6.61, 6.67, and 6.72.

A preliminary analysis by Heindl et al. (1999) of the HEXTE data concentrated on basic pulse phase resolved spectroscopy, dividing the pulse profile into four broad phase bins, and provided a first indication of a possible increase of the cyclotron line energy during the rise of the main pulse. As discussed in the previous

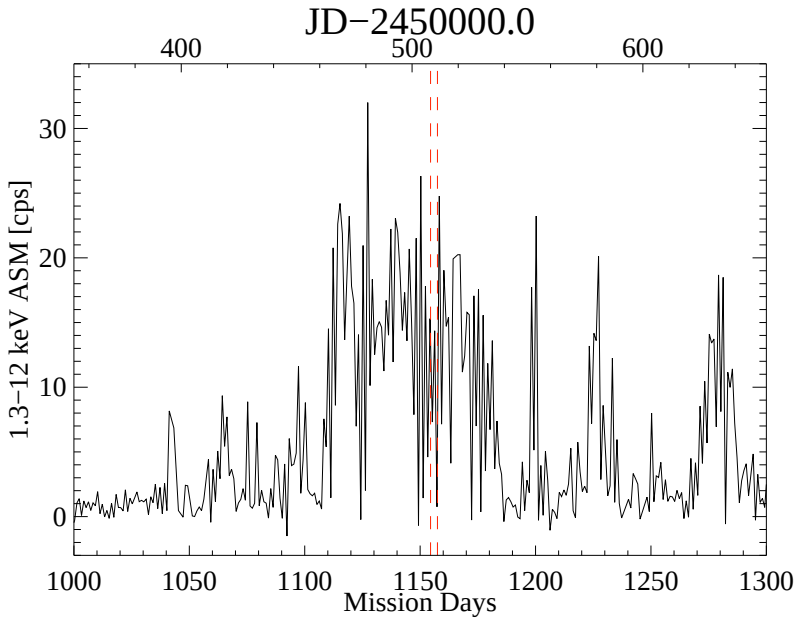

Figure 4.1 Long term light curve of Cen X-3 using the *RXTE*/ASM. The vertical lines indicate the times when *RXTE* performed the here discussed pointed observations.

chapter, systematic variations of the CRSF centroid energy over pulse phase have also been observed in other sources, e.g., Her X-1 (Soong et al., 1990; Gruber et al., 2001), Vela X-1 (La Barbera et al., 2003; Kreykenbohm et al., 2002), 4U 0352+309 (Coburn, 2001), 4U 1538−52 (Clark et al., 1990), and GX 301−2 (Kreykenbohm et al., 2004). The origin of these changes is not yet fully understood and possible scenarios were discussed in the previous chapter. Straightforward mechanisms like the angular dependence of relativistic corrections to the cyclotron energy are not sufficient to explain the observed variations.

4.2 Observation and data reduction

RXTE observed Cen X-3 with the Proportional Counter Array (PCA; Jahoda et al., 1996) and the High Energy X-ray Timing Experiment (HEXTE; Rothschild et al., 1998) between 1997 February 28 and March 3 (Figure 4.1) where Cen X-3 was in a state of medium to high activity (See Figure 4.1). The observation, proposal ID P20104, covered two consecutive binary orbits between eclipses,

excluding the time of eclipse between orbits (Figure 4.2, top panel). The total exposure time of 310 ks was split into 12 shorter data sets ("ObsIds") of ~ 8 hours each.

For $\sim 90\%$ of the time all five PCUs were collecting data during the observation, with PCU 3 being turned off for a short period. The PCA background was modeled using the "Sky-VLE" model. The HEXTE data was taken in modulating mode, switching every 16 s between source and background. At any given time one of the HEXTE clusters was on-source.

The data were reduced using HEASOFT version 6.0.6., applying standard extraction criteria: a pointing offset of $< 0.01°$ from the nominal source position, an exclusion time for the South Atlantic Anomaly (SAA) of 30 min, and a source elevation of $> 10°$. I imposed a maximum "electron ratio" of 0.15 in order to filter for precipitating particle events, taking into account a slightly elevated electron ratio level due to the influence of the bright target source. Depending on the analysis method, further grouping and filtering of the resulting good time intervals (GTIs) were applied in order to derive the PCA and HEXTE light curves and spectra. Details are described below, including the respective choices of data modes and binning options. All HEXTE data products were deadtime corrected using the HEASOFT ftool `hxtdead`. Since precise absolute flux measurements are beyond the scope of this paper, correction for the PCA deadtime of a few percent has not been carried out. Systematic uncertainties of 0.5% were included in the PCA spectral data. All high time resolution products were converted into the frame of reference at barycenter. To correct for the nature of the binary system, a binary correction was applied with the orbital values from Bildsten et al. (1997) presented in Table 4.1. Note that Raichur & Paul (2010) used the same *RXTE* data to update the orbital parameters of Cen X-3. For spectral modeling I used XSPEC version 11.3.2p (Arnaud, 1996).

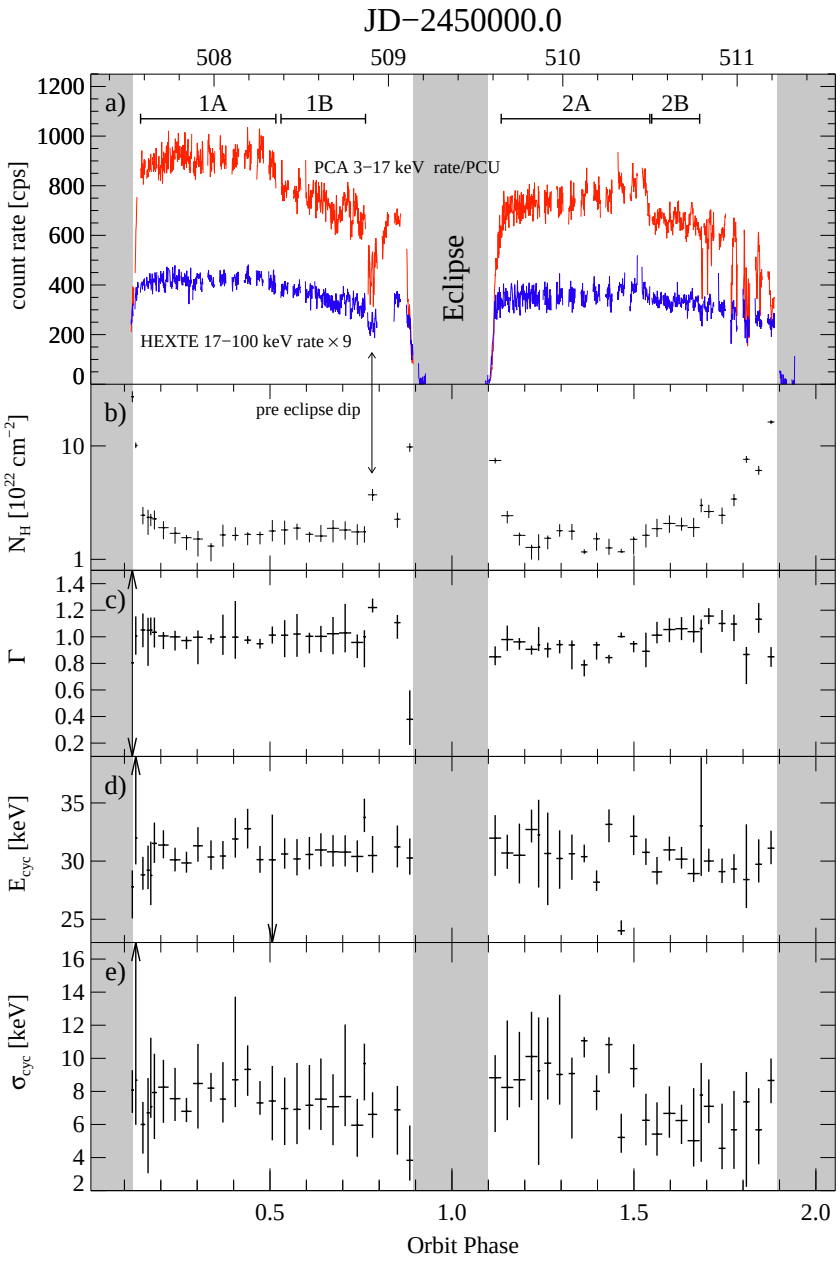

Figure 4.2 (a) Background subtracted 3–17 keV PCA (top) and 17–100 keV HEXTE (bottom) light curves (bintime 128 s). Shaded region indicates the eclipse of the compact object. Error bars are not plotted but are smaller than any variations visible. Horizontal lines above the data indicate the time intervals used for creating the time averaged spectra analyzed in §4.4.1. (b)–(e) Evolution of selected spectral parameters over two binary orbits. See text for model details. While the spectrum is stable – away from enhanced (pre-)eclipse $N_{\rm H}$ – over the first orbit, the behavior changes significantly after the mid-orbit break of the second orbit. Data points during eclipse are ignored for the spectral analysis.

Table 4.1. Orbital parameter of Cen X-3

Name	Bildsten et al. 1997	Reichur et al. 2010
Epoch	48561.656702*	50506.788423
$P_{\rm orb}$	2.08706533	2.08713936
$a_x \sin i$	39.627	29.6612
$\dot{P}_{\rm orb}/P_{\rm orb}$	$-9.93 \times 10^{-9\dagger}$	$-1.799 \times 10^{-6\ddagger}$
ecc	0.0016	¡0.0001

Note. — $^*T_{\pi/2}$= epoch of 90° mean orbital longitude, † days day^{-1}, ‡ days yr^{-1}.

4.3 Broad band orbital light curve

I extracted PCA and HEXTE light curves for all available ObsIDs. For the PCA, "standard2f" mode data were used, selecting the well calibrated energy range from 3–17 keV and the highest possible time resolution for this data mode of 16 s. Corresponding background model light curves were created. In the case of HEXTE I use science event mode data from 17–100 keV, with the source not being significantly detected at higher energies. Since the HEXTE source and background measurements for each cluster are performed quasi-simultaneously due to the 16 s rocking cycle, the high time resolution background for HEXTE light curves with less than 16 s time resolution is based on interpolating the measured background rates. For each 1 s time-resolved data bin in a 16 s segment I performed a linear interpolation of the background, using the neighboring 16 s background pointings[1]. As HEXTE's cluster B only has 3 fully functional detectors, the count rate for this cluster was normalized to cluster A.

Fig. 4.2*a* shows the background subtracted PCA and HEXTE light curves (both rebinned to a resolution of 128 s for display purposes). The PCA light curve has been normalized to one PCU and the HEXTE light curve consists of

[1]More precisely the background is measured during 12 s, preceded and followed by 2 s during which the cluster is moving between on- and off-source (Rothschild et al., 1998).

the summed contributions of both clusters and has been multiplied by a factor of nine, for display purposes. The same general features are visible above and below 17 keV, indicating the absence of extreme spectral variability over the binary orbit. For orbital phase $\phi_{\rm orb} > 0.5$ both orbits show a clear drop in the count rates. In addition the source was fainter overall during the second orbit, with the brighter first half of orbit 2 approximately at the same level as the less bright second half of orbit 1. The eclipse covers $\sim 20\%$ of the orbital period. Pre-eclipse dips can be observed in both orbits. Takeshima et al. (1991) and Nagase et al. (1992) also observed a drop in luminosity for the second part of the orbit, calling it a pre-eclipse dip. In this case I distinguish between before and after mid-orbit break and use the term pre-eclipse dip for relative short count rate drops, slightly longer than one satellite orbit.

In the first orbit one single pre-eclipse dip is visible around $\phi_{\rm orb} = 0.75$ (JD 2450508.4) where the PCA rate drops by a factor of two. Unfortunately, no HEXTE data are available in the archive for the egress of this pre-eclipse because the instrument was not turned on (PCA data are available). In the second orbit dipping activity starts around the same $\phi_{\rm orb}$ (JD 2450510.8), however, all pre-eclipse dips are partially obscured by data gaps due to SAA passages and earth occultations, so that no detailed analysis is possible.

Based on modeling the averaged spectrum for the first part of orbit 1 (1A in Fig. 4.2 and Table 4.3) I found a $2-10$ keV unabsorbed flux of $7.0^{+0.5}_{-0.7} \times 10^{-9}\,{\rm erg\,cm^{-2}\,s^{-1}}$ with the PCA. Taking the deadtime influence into account the measured flux increases by a few percent. The *BeppoSAX* observation analyzed by B00 was performed between 1997 February 27 19:45 and February 28 11:00 (UT) and thus overlaps with parts of data set 1A of the *RXTE* observation. B00 find a somewhat lower post eclipse egress 2–10 keV flux of $5.7 \times 10^{-9}\,{\rm erg\,cm^{-2}\,s^{-1}}$. The 18% discrepancy in flux is not surprising, due to the uncertainty in the cross calibration between the PCA and the *BeppoSAX*. I point out that the fluxes derived from the HEXTE instrument are 14% lower than those derived with the PCA (see $c_{\rm HEXTE}$ in Table 4.3) and thereby agree much better with *BeppoSAX*. Based on the PCA flux measurement we derived a 2–10 keV luminosity of $5.4^{+0.4}_{-0.5} \times 10^{37}\,{\rm erg\,s^{-1}}$,

Table 4.2. Best fit parameters for time and phase averaged spectra.

	1A	1B	2A	2B
$N_{\rm H}$ [$10^{22}{\rm cm}^{-2}$]	$1.6^{+0.4}_{-0.2}$	$1.8^{+0.5}_{-0.5}$	$1.3^{+0.4}_{-0.2}$	$2.4^{+0.5}_{-0.4}$
$E_{\rm cut}$ [keV]	$11.1^{+1.5}_{-2.3}$	$4.8^{+9.7}_{-4.8}$	$7.7^{+4.0}_{-2.5}$	$20.9^{+6.6}_{-7.1}$
$E_{\rm fold}$[keV]	$7.2^{+0.2}_{-0.3}$	$7.7^{+0.8}_{-0.5}$	$7.2^{+0.1}_{-0.4}$	$6.6^{+1.0}_{-2.3}$
$E_{\rm cyc}$ [keV]	$30.7^{+0.5}_{-0.4}$	$31.2^{+0.7}_{-0.7}$	$31.5^{+0.6}_{-0.5}$	$30.3^{+0.7}_{-0.6}$
$\sigma_{\rm cyc}$ [keV]	$6.4^{+1.0}_{-0.8}$	$4.3^{+2.8}_{-1.6}$	$6.3^{+0.9}_{-0.5}$	$7.3^{+1.4}_{-1.6}$
$\tau_{\rm cyc}$	$0.67^{+0.17}_{-0.07}$	$0.48^{+0.27}_{-0.09}$	$0.61^{+0.09}_{-0.06}$	$0.97^{+1.52}_{-0.34}$
Γ	$0.92^{+0.06}_{-0.04}$	$0.88^{+0.20}_{-0.15}$	$0.76^{+0.05}_{-0.06}$	$1.16^{+0.17}_{-0.09}$
$A_{\rm pl}$ [$\rm phcm^{-2}\,s^{-1}$]	$0.70^{+0.07}_{-0.05}$	$0.75^{+0.33}_{-0.18}$	$0.52^{+0.12}_{-0.08}$	$0.58^{+0.10}_{-0.06}$
$E_{\rm Fe}$ [keV]	$6.60^{+0.06}_{-0.05}$	$6.57^{+0.05}_{-0.06}$	$6.61^{+0.06}_{-0.05}$	$6.55^{+0.06}_{-0.06}$
$\sigma_{\rm Fe}$ [keV]	$0.13^{+0.18}_{-0.13}$	$0.22^{+0.17}_{-0.22}$	$0.09^{+0.21}_{-0.09}$	$0.27^{+0.15}_{-0.26}$
$A_{\rm Fe}$[10^{-2} ph $\rm cm^{-2}\,s^{-1}$]	$1.40^{+0.26}_{-0.21}$	$1.91^{+1.22}_{-0.34}$	$1.33^{+0.36}_{-0.26}$	$0.94^{+0.18}_{-0.16}$
$E_{13\,\rm keV}$ [keV]	$13.3^{+0.2}_{-0.2}$	$13.6^{+0.5}_{-0.4}$	$13.2^{+0.3}_{-0.2}$	$13.0^{+0.4}_{-0.7}$
$\sigma_{13\,\rm keV}$ [keV]	$2.8^{+0.4}_{-0.3}$	$4.0^{+1.0}_{-1.1}$	$3.4^{+0.4}_{-1.3}$	$3.2^{+0.8}_{-0.6}$
$A_{13\,\rm keV}$[10^{-2} $\rm phcm^{-2}\,s^{-1}$]	$5.2^{+4.4}_{-1.6}$	$23.0^{+35.0}_{-14.0}$	$7.0^{+5.3}_{-3.8}$	$3.1^{+5.3}_{-1.3}$
$c_{\rm HEXTE}$	$0.857^{+0.003}_{-0.003}$	$0.856^{+0.003}_{-0.003}$	$0.854^{+0.003}_{-0.003}$	$0.860^{+0.004}_{-0.004}$
$L_{2-10\,\rm keV}$ [$10^{37}\rm erg\,s^{-1}$]	$5.4^{+0.4}_{-0.5}$	$4.4^{+1.2}_{-1.1}$	$4.3^{+0.8}_{-0.3}$	$4.0^{+0.6}_{-1.0}$
$\chi^2_{\rm red}$/dof	1.13/83	0.71/83	0.86/83	0.77/83

Note. — The data sets 1A–2B are defined in Fig. 4.2. Parameters listed are the hydrogen column density $N_{\rm H}$; the Fermi-Dirac cutoff and folding energies $E_{\rm cut}$ and $E_{\rm fold}$; the CRSF energy $E_{\rm cyc}$, width $\sigma_{\rm cyc}$, and depth $\tau_{\rm cyc}$; the power law index Γ and strength $A_{\rm pl}$; the Fe K emission line energy $E_{\rm Fe}$, width $\sigma_{\rm Fe}$, and strength $A_{\rm Fe}$; and the 13 keV emission feature energy $E_{13\,\rm keV}$, width $\sigma_{13\,\rm keV}$, and strength $A_{13\,\rm keV}$. Uncertainties are quoted at the 90% confidence level assuming independent parameters (see text for existing correlations). The flux normalization of the HEXTE instrument with respect to the PCA, $c_{\rm HEXTE}$, and the luminosity in the 2–10 keV energy range derived from the PCA, $L_{2-10\,\rm keV}$, are also given.

applying a distance of 8 kpc (B00: $4.4 \times 10^{37}\,\mathrm{erg\,s^{-1}}$). The fainter second orbit shows a $2-10$ keV flux of $5.6^{+1.0}_{-0.4} \times 10^{-9}\,\mathrm{erg\,cm^{-2}\,s^{-1}}$ during its first half, corresponding to a luminosity of $4.3^{+0.8}_{-0.3} \times 10^{37}\,\mathrm{erg\,s^{-1}}$. The luminosities after the mid-orbit drop are $4.4^{+1.2}_{-1.1} \times 10^{37}\,\mathrm{erg\,s^{-1}}$ and $4.0^{+0.6}_{-1.0} \times 10^{37}\,\mathrm{erg\,s^{-1}}$ for orbit 1 and 2, respectively, i.e. the relative flux change in the second orbit is a factor of two smaller than in the first orbit.

4.4 Phase Averaged Spectroscopy

4.4.1 Time averaged spectral parameters

For each available ObsId "standard2f" mode PCA spectra and standard science event mode HEXTE spectra were extracted, including the corresponding background spectra. All spectra within one of the four time intervals indicated in Fig. 4.2*a* were added. The resulting time averaged spectra are count rate selected in the sense that they are characterized by episodes of different average count rate levels within a given binary orbit, i.e., for each of the two orbits the first interval spans the bright phase up to the mid-orbit break, while the second interval spans the time up the on-set of pre-eclipse dipping. Time averaged broad band source spectra were modeled taking background subtracted PCA spectra from 3–23 keV and background subtracted HEXTE spectra from 17–100 keV into account, rebinning data above 60 keV by a factor of five. As the CRSF centroid energy is at ~ 30 keV and a contamination of this data due to the Xenon K-edge at 33 keV would be possible, we decided not to increase the PCA range up to 60 keV as described by Rothschild et al. (2006), Appendix B.

The basic continuum we use throughout this chapter is an absorbed power law with index Γ, modified by a Fermi-Dirac cutoff characterized by cutoff and folding energies E_{cut} and E_{fold} (local XSPEC model `fdcut`, Tanaka, 1986), as discussed in section 3.3. Fig. 4.3*b* shows the residuals for fitting an absorbed `fdcut` model to the averaged broad band spectrum for the first part of orbit 1 (1A in Fig. 4.2 and Table 4.3), also including a Gaussian line to model the narrow Fe K emission feature. The reduced χ^2 for this fit is χ^2_{red}=24 for 88 degrees of freedom

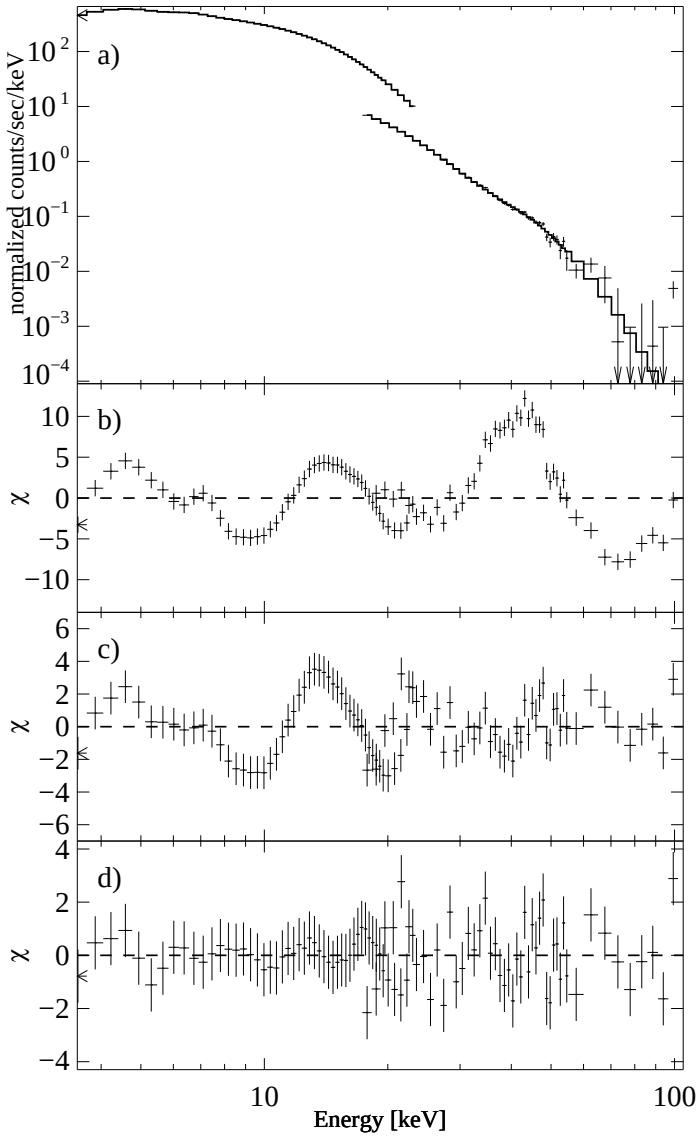

Figure 4.3 (a) PCA and HEXTE phase averaged counts spectra, accumulated over the first part of the first binary orbit (1A in Fig. 4.2 and Table 4.3), and best fit model. (b) Residuals for an absorbed power law with a Fermi-Dirac cutoff, and a Gaussian Fe line. (c) Improved residuals obtained by adding a cyclotron line at $\sim 30\,\mathrm{keV}$. (d) Best fit residuals obtained by modeling the broad residual around 13 keV with an additional Gaussian emission line. The reduced χ^2 values are 24, 3.4, and 0.97 from (b) to (d). See text for a detailed description of the model components and Table 4.3 for the best fit parameters. The count rate is normalized by taking the effective detector area into account.

(dofs) and an absorption line is clearly visible in the residuals at $\sim$ 25–30 keV, which I interpret as a CRSF. To model the CRSF I use the previously discussed `gabs` model, a line shape with a Gaussian optical depth profile, which is the basis for past modeling of *RXTE* data While including this component improves $\chi^2_{\rm red}$ to 3.5 for 86 dofs a strong residual structure remains around $\sim$ 13 keV (Fig. 4.3*c*). Adding a single Gaussian emission line at this energy results in a good overall fit with $\chi^2_{\rm red} = 1.13$ for 83 dofs (Fig. 4.3*d*). The same model was also successfully applied to describe the other three time-averaged spectra with the resulting best fit parameters listed in Table 4.3. We note that the line parameters do not significantly depend on the continuum model chosen: fits using a negative-positive exponential continuum (local XSPEC model `npex`, Mihara, 1995) instead of the power law with Fermi-Dirac cutoff lead to the same cyclotron line parameters. Compared to a `NPEX` or `highecut` continuum we achieved slightly better spectral fits with a power law with Fermi-Dirac cutoff. B00 used a blackbody emission to describe the spectrum between 0.1 and 2 keV. The spectral data does not extend below 3.5 keV and I do not detect an influence of a black-body at lower energies. Becker & Wolff (2007) are using a Comptonized Bremsstrahlung spectrum to calculate the continuum. They state that the contribution of blackbody emission is negligible in their spectrum.

To better understand the observed 13 keV feature, I checked for correlations for all possible pairs of spectral parameters using χ^2 contours. I found no correlation between the parameters characterizing the broad 13 keV feature and the cyclotron line parameters or the roll-over of the continuum model. As expected, however, a dependence on the power law index Γ (and therefore also on $N_{\rm H}$) was clearly detectable. An increasing Γ or $N_{\rm H}$ value resulted in a lower centroid energy of the 13 keV feature. I conclude that this feature is part of a more complex continuum rather than the simple phenomenological approach used here.

A broad feature at energies below the fundamental cyclotron line, mostly around $\sim$ 10 keV, has also been observed in several other cyclotron line sources, e.g., with *RXTE* in MXB 0656−072 (McBride et al., 2006), Her X-1, 4 U1626−67, 4U 1907+09, and 4U 1538−52 (Coburn et al., 2002), and with *Ginga* in 4 U1538−52,

4U 1907−09, and V 0331+53 (Mihara, 1995). A weak 10 keV absorption feature was also reported by Santangelo et al. (1998) for a different *BeppoSAX* observation of Cen X-3. Such residuals are usually best described by an additional broad absorption line to improve the fits. In some cases a broad emission line can describe the data better. In this data I find that an emission line at 13 keV describes the observed feature much better. Substituting the 13 keV emission line by a Gaussian absorption line at ~ 8 keV leads to $\chi^2_{\rm red} = 1.31$ as compared to 1.13 for 83 dofs .

As described earlier, B00 observed quasi-simultaneously with *BeppoSAX* (11 hours overlap with observation 1A from Table 4.3). A phase averaged analysis was carried out by these authors using a power law with high-energy cutoff, smoothed around the cutoff energy for the continuum. The CRSF parameters, with $E_{\rm cyc} = 30.6 \pm 0.6$ keV and $\sigma_{\rm cyc} = 5.9 \pm 0.7$ keV, are comparable to those presented here . Their measured value of $N_{\rm H} = 1.95 \pm 0.03 \times 10^{22}\,{\rm cm}^{-2}$ is still within the error bars of this RXTE observation of $N_{\rm H} = 1.6^{+0.4}_{-0.2}\,{\rm cm}^{-2}$. Their photon index of $\Gamma = 1.208 \pm 0.007$ is much higher than the value of $\Gamma = 0.92^{+0.06}_{-0.04}$ due to the model definitions. I applied the B00 model to this data and obtained consistent results within error bars. Due to a known deviation in the slope of the Γ-index between *RXTE*-PCA and *BeppoSAX* (Kirsch et al., 2005), my resulting value of $\Gamma = 1.26 \pm 0.03$ for the B00 model is marginally consistent.

4.4.2 Physical model for CRSF

Ideally, models based on a physical description of the accretion column above the magnetic poles of the neutron star should be used to fit the shape of the cyclotron line and the spectral continuum. Despite recent successes (Becker & Wolff, 2007, see chapter 3 for details), however, a fully self-consistent solution to the problem of continuum formation and radiative transfer in neutron star accretion columns is not yet available. I used the physical derived Monte Carlo model Schönherr et al. (2007), which was described in more detail in chapter 3 to try a physical interpretation of the observed CRSF.

Here, I will present results from the analysis of the time averaged 20–70 keV HEXTE data with this model. I limit myself to the 1-0 geometry for the line

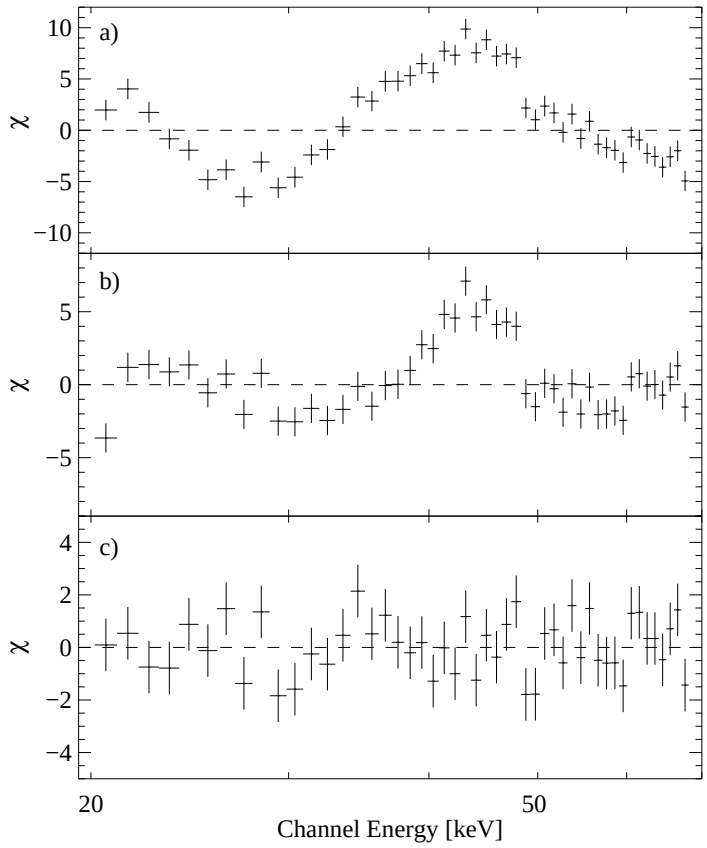

Figure 4.4 Residuals for fitting data with CRSF shapes obtained for Monte Carlo simulations applied on phase averaged HEXTE data from 20-80 keV. (a) continuum `fdcut*powerlaw` with $\chi^2_{\rm red} = 24.0$ (45 dofs). (b) included `cyclomc` model for Slab 1-0 geometry showing emission wings ($\chi^2_{\rm red} = 8.0$ with 41 dofs). (c) added partial covering to reduce emission wings ($\chi^2_{\rm red} = 1.4$ with 39 dofs). Note that the residuals in (a) are slightly different than those shown in Fig. 4.3 since only the HEXTE data were modeled.

forming region (see Schönherr et al., 2007; Freeman et al., 1999; Isenberg et al., 1998, for details), where the accretion column is described as a slab with the slab normal being parallel to the magnetic field and where the continuum spectrum is illuminating the bottom of the slab. This setup mimics a plane-parallel and thin emission region close to the surface. The continuum is again taken to be a power law modified by a Fermi-Dirac cutoff (Eq. 3.9). I decided to exclude $N_{\rm H}$ from the continuum because it is neglectable in the chosen energy range. A gravitational redshift $z = 0.3$ is assumed, a typical value for neutron stars (see chapter 1).

Figure 4.4a shows the residuals after modeling the HEXTE spectrum with

the continuum model without taking the cyclotron f formation into account. Introducing the cyclotron line model and refitting significantly reduces the residuals (Fig. 4.4b), although some structure remains. As has been shown by Schönherr et al. (2007), this structure is caused by the fact that the predicted self-consistent cyclotron line shapes are generally too deep and in addition have significant emission wings, assuming the simplified scenario of a constant magnetic field and simple geometry. These wings are due to so-called spawned photons, which are the result of the stepwise de-excitation of electrons from higher Landau levels after their excitation through a scattering photon (Araya & Harding, 1999; Araya-Góchez & Harding, 2000). One way of reducing the line depth and strength of the wings is by invoking a partial covering approach, where only part of the seed photon spectrum is seen through the accretion column, while the remainder is observed without being modified by the column. Note that this approach is not unique. Other geometries, such as a seed photon source distributed throughout the accretion column, a column with a temperature gradient, or a vertically varying magnetic field, could also result in shallower cyclotron line profiles with less dominant wings (Schönherr et al., 2007).

Shortly after the publication of this data, a problem in the calculation of the cross sections was found, making the here presented results not fully consistent. As mentioned earlier, a new version of the `cyclomc` software will be published soon, and the here presented analysis of the CRSF will be recreated. To have a comparison with the future analysis, and also the empirical models, the

The result of fitting the data with a partial covering model is shown in Fig. 4.4c. This model describes the data well ($\chi^2_{\rm red} = 1.35$ for 40 degrees of freedom). The best fit parameters are $B = 3.46^{+0.07}_{-0.03} \times 10^{12}\,\mathrm{G}$ for the magnetic field, $kT_{\rm e} = 7.04^{+0.63}_{-0.48}\,\mathrm{keV}$ for the electron temperature, $\tau_{\rm T} = 2.4^{+0.05}_{-0.07} \times 10^{-3}$ for the Thomson optical depth of the continuum, not to be confused with the optical depth of the `gauabs` model. Note that the optical depth in the lines can be larger by a factor of more than 10^4 (Araya & Harding, 1999). The cosine of the angle, θ, between the line of sight and the magnetic field is $\cos(\theta) = 0.94^{+0.00}_{-0.07}$, i.e., $\theta = 20^{+10}_{-0}$ degrees.

To check the consistency of this result with that determined in the phase averaged data, I use the best-fit parameters from above to calculate the centroid energy of the cyclotron line based on equation 3.19, including the gravitational redshift (see chapter 3 for details):

$$E_{\rm cyc} = m_{\rm e}c^2 \frac{\sqrt{1 + 2B/B_{\rm crit}\sin^2(\theta)} - 1}{\sin^2(\theta)} \times \frac{1}{1+z} \tag{4.1}$$

giving $E_{\rm cyc} = 30.9^{+0.7}_{-0.3}$ keV for data set 1A. The width of the CRSF can be estimated from Doppler broadening (e.g., Meszaros & Nagel, 1985a)

$$\sigma_{\rm FWHM} = \sqrt{\frac{8\ln(2)kT_{\rm e}}{m_{\rm e}c^2}}\,|\cos(\theta)|\,E_{\rm cyc}. \tag{4.2}$$

In this case I obtain a width of $8.0^{+0.5}_{-0.9}$ keV. Both results lie within the uncertainties of Table 4.3. The CRSF depth in this model is described by the Thomson optical depth and cannot be directly translated into the `gauabs` depth due to strong dependencies of the scattering cross section on the emission angle θ.

4.4.3 Spectral evolution over the orbit

This data set allows us to perform the most complete and detailed analysis of the orbital dependence of Cen X-3's broad band spectrum to date. I extracted PCA and HEXTE spectra from the same data modes as for the time averaged analysis (§4.4.1) but using shorter GTIs with their duration mainly constrained by observation gaps due to SAA passages and earth occultations. This selection procedure leads to spectra with a typical exposure time of ~ 3.5 ks ($\Delta\phi_{\rm orb} \sim 0.03$). Data subsets with considerably longer observation times were further split into subsets of ~ 3.5 ks duration. I ignored data taken during the eclipse and I also ignored the data set at the end of the pre-eclipse dip in orbit 1, since no HEXTE data were available. The resulting broad band spectra were then modeled with the same model used to describe the time averaged spectra in §4.4.1. The chosen energy range was 3.5–23 keV for PCA and 18–60 keV for HEXTE.

Fig. 4.2*b*–*e* shows selected time-resolved spectral parameters. As already indicated by the time averaged results (Table 4.3), the two orbits show a somewhat

different behavior with respect to the two luminosity levels observed in each case. During the first orbit the parameters are essentially stable within the uncertainties over most of the orbit. $N_{\rm H}$ increases near eclipse ingress and egress during both orbits (Fig. 4.2*b*) as expected from an increasing amount of stellar material in the line of sight (Clark et al., 1988). During the pre-eclipse dip in orbit 1, $N_{\rm H}$ is enhanced by a factor of ~ 2. Γ also increases during the pre-eclipse dip (Fig. 4.2*c*). Error contour plots for individual observations throughout the orbit calculated using the `steppar` command in XSPEC are shown in Fig. 4.5. A clear correlation between $N_{\rm H}$ and Γ can be seen throughout the orbit. During the pre eclipse dip the same correlation can be observed, although at higher $N_{\rm H}$ and Γ values (Fig. 4.5 inset). This correlation is an artifact from the continuum modeling. When modeling the spectrum one achieves similar χ^2 values for different $N_{\rm H}$–Γ combinations. Increasing $N_{\rm H}$ results in a reduction of flux at lower energies. This effect can be compensated by using a softer, and therefore steeper, power law component leading to higher Γ values. Therefore a simultaneous increase in $N_{\rm H}$ and Γ is expected.

During the second orbit I observe a change of the general behavior of many of the spectral parameters that is apparently related to the mid-orbit luminosity drop. $N_{\rm H}$ stays relative constant prior to mid-orbit and rises continuously afterward (Fig. 4.2*b*). Analysis with a frozen Γ value to take the $N_{\rm H}$-Γ-correlation into account, showed the same tendency in $N_{\rm H}$ during the second orbit. As in the pre-eclipse dip of orbit 1, the power law Γ slightly increases with $N_{\rm H}$ (Fig. 4.2*c*). The CRSF parameters variability is slightly more pronounced during the second orbit (Fig. 4.2*d* and Fig. 4.2*e*). Note that the cutoff and folding energies do not show any significant change throughout the whole observation.

4.4.4 Wind model

I calculated a simple radiation driven wind model for $N_{\rm H}$ based on the model by Castor et al. (1975, hereafter CAK), although I note that this assumption of a radiation driven wind is only an approximation, as it is very likely that the wind is disrupted by the strong X-rays present in the system (Wojdowski et al., 2001,

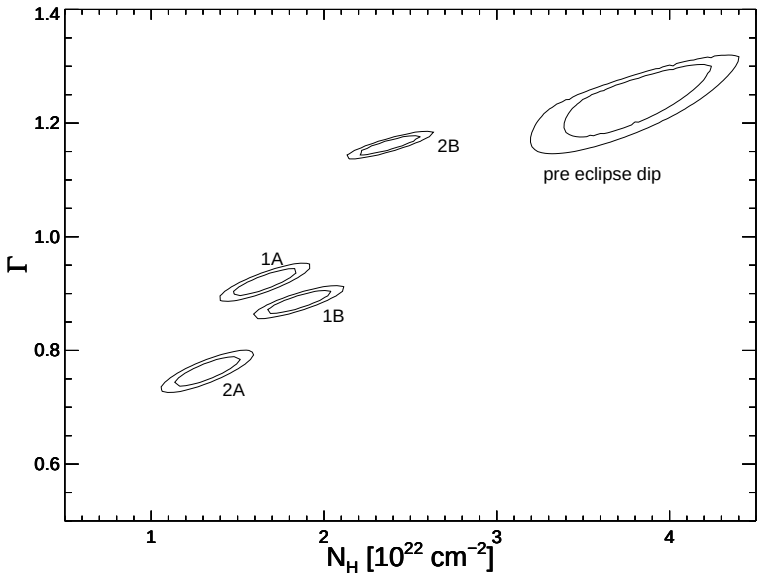

Figure 4.5 XSPEC contour plots for 4 selected 3.5 ks observations throughout the first binary orbit. The $N_{\rm H} - \Gamma$ correlation can be seen in througout all data sets. The shown contours are 1σ confidence levels. The inset shows the 1σ error contour during the pre-eclipse dip in the first orbit. Note that for small Γ values the contours are sometimes dominated by numerical noise.

2003, and references therein). I assumed a mass loss, $\dot{m}$, for the donor star and the CAK velocity profile $v(r) = v_\infty(1 - R_\star/r)^\beta$, where v_∞ is the terminal velocity. This gives

$$n_{\rm H}(r) = \frac{\dot{m}}{4\pi k r^2 v(r)} \tag{4.3}$$

for the radial particle density profile, where k is a conversion factor from mass to effective proton particle density, assuming a wind with cosmic abundances, a system inclination of 90°, and ignoring the orbital eccentricity ($e \leq 0.016$). I then integrate over the density along the line of sight for a specific position in the orbit:

$$N_{\rm H} = \int_{l_{\rm NS}}^{\infty} n_{\rm H}(l')dl', \tag{4.4}$$

where $l_{\rm NS} = R_{\rm d}\cos(\phi_{\rm orb})$ is the position of the neutron star, projected to the celestial plane and where $R_{\rm d} = 19\,R_\odot = 1.58\,R_\star$ is the separation between neutron star and donor (Blondin, 1994). Assuming a typical value of $\beta = 0.8$ (Friend & Abbott, 1986) I obtain good results for $\dot{m} = 7{\times}10^{-7}\,{\rm M}_\odot\,{\rm yr}^{-1}$ and $v_\infty = 1200\,{\rm km\,s}^{-1}$ (Fig. 4.6*a*). For better comparison I also show the difference between data and

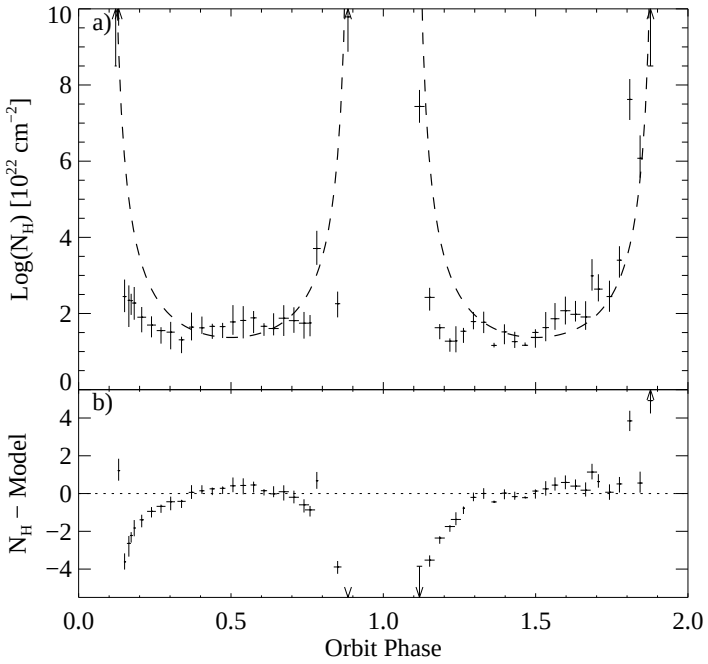

Figure 4.6 (a) values of $N_{\rm H}$ as a function of orbital phase (crosses) and calculated model for parameters mentioned in text (dashed line). (b) Difference of $N_{\rm H}$ and wind model.

model (Fig. 4.6*b*). Due to the definition of the model a strong correlation between increasing mass loss and terminal velocity is present, such that absolute values cannot be determined by this approach.

Both orbits show a different behavior in the evolution of $N_{\rm H}$. During the first orbit, where $N_{\rm H}$ is mostly constant, I see a symmetrical deviation during eclipse ingress and egress, when this simple approach fails to model the data. A similar deviation is seen at the beginning of the second orbit. After mid-orbit $N_{\rm H}$ keeps increasing for the remainder of the orbit, indicating an increased absorption in the second half of the orbit. A similar behavior has been simulated by Blondin et al. (1990) and probably indicates the presence of an accretion wake in this system. A small bump around $\phi_{\rm orb} = 0.3 - 0.4$ can be observed in both orbits, more pronounced in the second one. This bump also exists in the simulation and is another indication of a tidal wake.

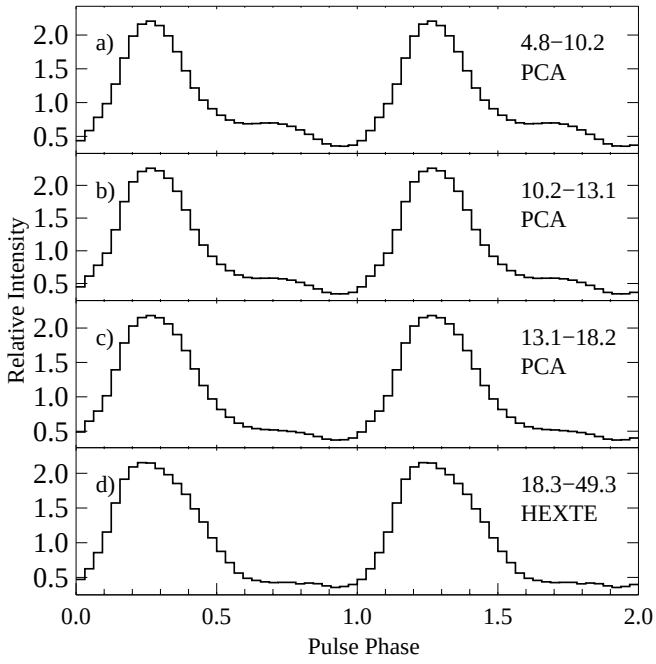

Figure 4.7 Normalized PCA and HEXTE pulse profiles for four energy bands: (a) 4.8–10.2 keV, (b) 10.2–13.1 keV, (c) 13.1–18.2 keV and (d) 18.3–49.3 keV. A secondary peak at pulse phase ~ 0.7 is visible for lower energies.

4.5 Phase resolved spectroscopy

4.5.1 Pulse profile

Pulse profiles with 32 phase bins for 4 energy bands were extracted for each of the 12 ObsIds. I decided to use locally determined pulse periods for each ObsID and the ephemeris from Nagase et al. (1992), after using the ephemeris and period from B00 did not result in consistent pulse profiles. All pulse profiles showed a similar shape with a main peak at pulse phase ($\phi_{\rm pulse}$) ~ 0.3, which allowed us to combine them after phase alignment. Figure 4.7 shows the resulting pulse profiles for four different energy ranges. A second weak peak at pulse phase of ~ 0.7 is visible at energies below 18 keV. Nagase et al. (1992) observed Cen X-3 in 1989 March with *Ginga* when the source had a $1-37$ keV luminosity of 5×10^{37} erg s^{-1}, a factor of two fainter than during this RXTE observation, and presents pulse profiles for 9 energy bands. At lower energies they observe a double peaked profile, where both peaks have equal intensities below 7 keV. Above 18 keV the profile

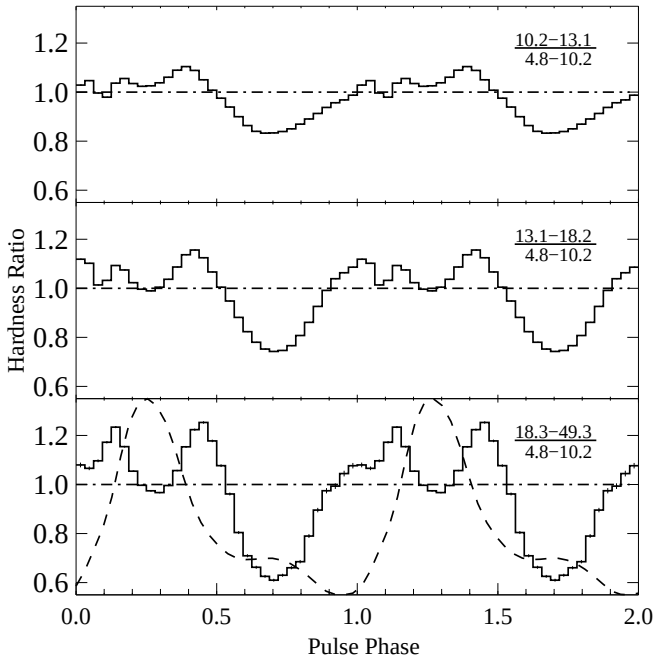

Figure 4.8 Normalized hardness ratios. Each panel has been calculated by taking the according pulse profile from Fig. 4.7 divided by panel (a) from Fig. 4.7. The pulse profile is indicated in the bottom panel (dashed line). Top right corner show the energy ranges.

is comparable to RXTE results with only one main peak. Audley et al. (2001) showed that the $2 - 25\,\mathrm{keV}$ pulse profile is highly variable, changing between an asymmetric double peaked profile, as in this observation, and a much more complex pulse profile with multiple peaks, depending on the count rate of the binary system.

I used the pulse profiles presented in Fig. 4.7 to create hardness ratios for each energy band using the lowest energy range as baseline (Fig. 4.8). At $\phi_{\mathrm{pulse}} = 0.7$, I see the decrease in hardness of the secondary peak toward higher energies. The rise and decay of the main peak ($\phi_{\mathrm{pulse}} = 0.1$ and 0.5) show peaks in the hardness ratio, a clear indication that the lower energy emission region is beamed more sharply. It is not clear if a third peak, visible at $\phi_{\mathrm{pulse}} = 1.0$, originates from a real physical feature or is part of an artificial wing from a phase continuity in the plot.

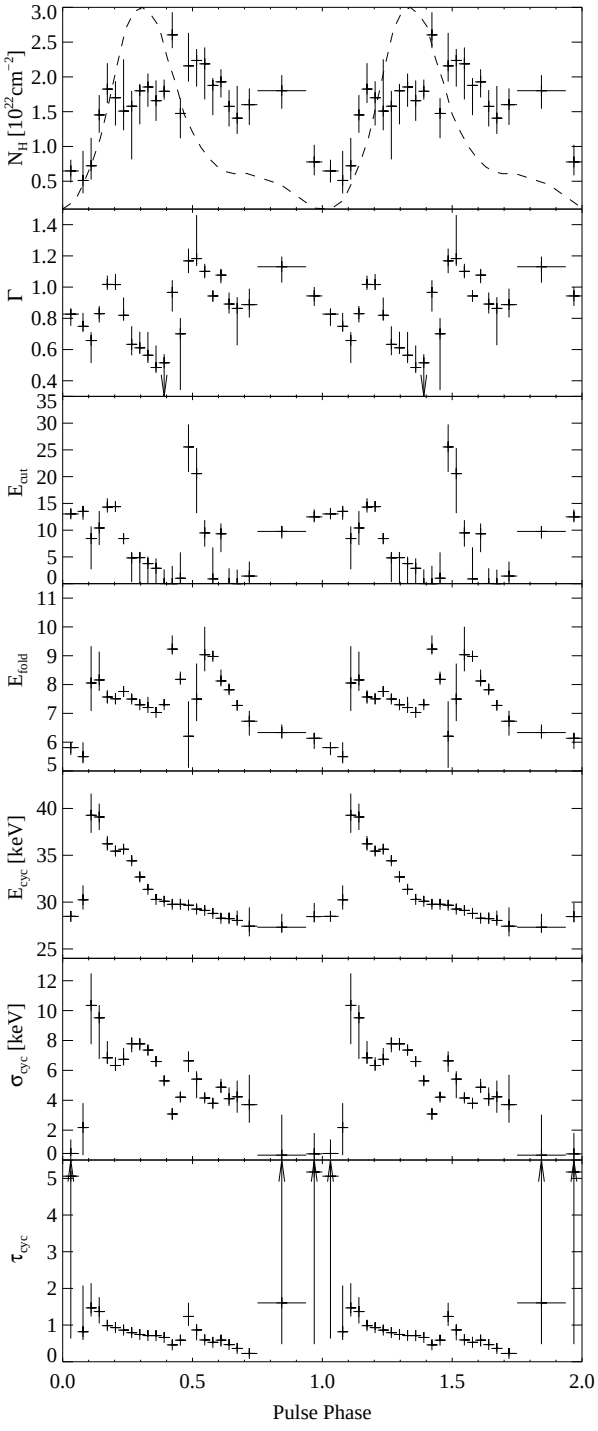

Figure 4.9 Selected spectral parameters over the pulse profile (dotted line). The last phase bins are binned. Error bars indicate 1σ deviations.

4.5.2 Spectral evolution over the pulse profile

Extraction of phase resolved spectra for each individual ObsId with 32 phase bins resulted in large uncertainties for the individual parameters. I therefore created phase resolved spectra for each ObsID with 8 phase bins and observed similarities in the behavior of the spectral parameters, e.g., an increase of the CRSF centroid energy during the rise of the main peak. I decided to sum all ObsIDs and use 32 phase bins resulting in an integration time of ∼12 ks in each phase bin for a phase resolved analysis. In the pulse minimum I binned the phases by a factor of 2, and even by a factor of 6 for the secondary peak, to be able to properly constrain the CRSF feature. This results in a total of 24 phase bins on which I performed a spectral analysis using the same model as in the phase averaged analysis. Figure 4.9 shows the best-fit values of selected parameters over the pulse period. Compared to the phase averaged analysis, not only N_H and Γ but also the CRSF parameters change drastically over the pulse period.

The pulse profile can be roughly divided into three regions where the continuum parameters are significantly different: main peak, secondary peak, and pulse minimum. The column density N_H is constant with a value of $1.5^{+0.3}_{-0.4} \times 10^{22}\,\mathrm{cm}^{-2}$ during the main peak. Between main and secondary peak, this value suddenly jumps up, to $2.2^{+0.2}_{-0.3} \times 10^{22}\,\mathrm{cm}^{-2}$. χ^2 contours indicate that this increase is not due to statistical fluctuations. During the pulse minimum the N_H value reaches a minimum of $0.5^{+0.5}_{-0.2} \times 10^{22}\,\mathrm{cm}^{-2}$. Another interpretation would be that N_H follows the shape of the pulse profile and is somehow capped during the main peak. I have not identified a physical explanation for this observational fact which might be caused by the limitations of the current continuum modeling. The power law index Γ also changes strongly over the pulse phase. It increases during the rise of the pulse up to a value of $1.0^{+0.1}_{-0.1}$ and then decreases to $0.5^{+0.2}_{-0.3}$ for the duration of the main peak. After the main peak the value jumps back up to $1.2^{+0.1}_{-0.1}$. The CRSF centroid energy also shows a drastic change throughout the pulse. During the rise of the main peak the value increases from ∼ 30 keV to almost 40 keV, slowly decreasing throughout the main peak and descent below the phase average value of less than 30 keV. The evolution of the CRSF throughout the pulse is similar to the shape of

the pulse profile with a phase shift of $\Delta\phi_{\rm pulse} = 0.2$ (ignoring the two outliers in the pulse rise I still obtain $\Delta\phi_{\rm pulse} = 0.1$). The width $\sigma_{\rm cyc}$ of the CRSF approximately follows the evolution of the centroid energy over the main peak, and drops to ~ 0 during the off-pulse, an indication that the CRSF is not well constrained. The depth $\tau_{\rm cyc}$ is slowly decreasing throughout the whole pulse and is also much less constrained during the pulse minimum. Compared to the other known sources featuring a variation of the CRSF, e.g., Her X-1 (Gruber et al., 2001), Vela X-1 (La Barbera et al., 2003; Kreykenbohm et al., 2002), 4U 0352+309 (Coburn, 2001), and GX 301−2 (Kreykenbohm et al., 2004), Cen X-3 is the only known source to show an increase of the centroid energy during the ascent of the main pulse.

B00 also provided a phase resolved analysis, but they divided the pulse into only 4 parts: ascent, maximum, descent of the main peak, and minimum, including the secondary peak. They also observe an increase in the CRSF centroid energy up to $36.6^{+1.6}_{-2.4}$ keV in the ascent. I combined the phase resolved spectra according to the phase bins in B00 and applied their model on these results. I can confirm the results from B00 within the error bars with small deviations for Γ.

4.6 Discussion and Conclusions

4.6.1 Orbital Variability of the X-ray Spectrum

The analysis for individual satellite orbits shows the evolution of the spectral parameters throughout both orbits. A difference between both orbits can be observed, not only in the luminosity, but also in the evolution of $N_{\rm H}$ and Γ, both correlated with each other. Comparison with a simple CAK wind model showed that, while reproducing the overall trends in $N_{\rm H}$, such a model is not sufficient to describe the observed data fully, regardless of inaccuracies during eclipse ingress and egress. Wojdowski et al. (2001) use a similar approach on a Cen X-3 data set from *ASCA* with significantly different results. Probing the parameter space they find best fit values for $\beta = 0.57^{+0.06}_{-0.07}$ and ionization parameter $\xi = 1.56$, which then can be used to determine the accretion rate and the terminal velocity of the system. Applying these parameters to my model I find a minimum $N_{\rm H}$ value of

$3.2 \times 10^{22}\,\mathrm{cm}^{-2}$, 1.5 times higher than the observed data. Also the change of N_{H} during ingress and egress of the eclipse is not as drastic as observed here. With a fixed $\beta = 0.8$ and $\xi = 0.7$ I obtain the results shown in Fig. 4.6.

In the data set a small increase in N_{H} is seen in the first half ($\phi_{\mathrm{orb}} = 0.3{-}0.4$) in both orbits, more pronounced in the second orbit. Blondin et al. (1991) used two-dimensional numerical simulations based on the CAK model to calculate the column density in massive X-ray binary systems with a tidal stream and observes such an increase in N_{H} around $\phi_{\mathrm{orb}} = 0.4 - 0.5$. They interpret this as a leading bow shock in front of the accretion stream which is extremely sensitive to orbital parameters, e.g., distance between neutron star and donor or the intensity of the stellar wind. A possible explanation of my observed increase is that it corresponds to this bow shock observed in the simulations. In the second half of the orbit, Blondin et al. (1991) see a general increase in N_{H}, comparable to my observations during the second orbit. This increase could be due to material in the line of sight, trailing the tidal wake. Taking into account that the continuum parameters do not change significantly over the orbit I can rule out that the system changed its state. Similar increases have been observed in other sources, e.g., 4U1700−37 (Haberl et al., 1989) and Vela X-1 (Haberl & White, 1990), where both systems are believed to have a tidal streams. In these cases, the difference was more than an order of magnitude, whereas here the increase is on the order of a factor of 2–3. We point out that we also observe a change in N_{H} with a fixed photon index so that the N_{H}-Γ-correlation alone can not be responsible for this rise. The fact that this increase is only visible during the second orbit could imply that the overall luminosity has an influence on the visibility of the accretion wake.

I do not rule out other possible explanations for the differences in orbit 1 and 2. Blondin et al. (1990) showed in their simulations that the column density throughout the orbit changes between consecutive orbits due to variability in the accretion flow. The drop in luminosity of $\sim 20\,\%$ between orbit 1 and 2 indicates the decrease of $\dot{m}$. In the simulations Blondin et al. (1991) observe instabilities for lower luminosities, i.e., less photon pressure from the donor star, trailing the tidal wake. These instabilities can create small pockets of denser material which also

could be responsible for the observed increase in $N_{\rm H}$. Also, the observations were performed during a time of strong and very variable activity (see Figure 4.1), so that sudden changes in the accretion rate are not unexpected.

Another hint for the existence of multiple material clumps is seen in the light curve (Figure 4.2a). Compared to the first orbit, the second orbit shows multiple pre-eclipse dips. In the first orbit, during the pre-eclipse dip $N_{\rm H}$ increases by a factor of ~ 2. Multiple dips close together could cause an overall increase of $N_{\rm H}$ throughout the second orbit. One small caveat in this theory is that the increase in $N_{\rm H}$ starts directly after the mid-orbit break, whereas the pre-eclipse dips are occurring at $\phi_{\rm orb} > 0.7$ of the second orbit. Therefore I do not think that pre-eclipse dips can be exclusively responsible for the rise.

4.6.2 Spectral and Pulse Phase Variability

I divided each orbit into two parts, before and after mid-orbit break, and extracted phase averaged spectra for each part. For the analysis I applied a power law with a Fermi-Dirac cutoff as continuum with an additional iron emission line. A CRSF at ~ 30 keV is visible in all data sets, consistent with previous observations. The widely used local model `gauabs` gave the best fit results for this feature. No significant changes in the spectral parameters could be observed throughout the orbit. An additional broad Gaussian emission feature at 13 keV had to be introduced to get reasonable residuals. I tested for correlations of this feature with other model parameters and determined that it is probably an artifact of the current continuum modeling. We conclude that the 13 keV feature is equal to the 10 keV absorption feature that has been observed in multiple different sources and with different instruments. Further investigation of this feature is necessary, but this is beyond the scope of this thesis.

I also applied a newly developed physical model, `cyclomc` (Schönherr et al., 2007), based on Monte-Carlo simulations to part of the phase averaged data (data set 1A). This model is self-consistent in determining the CRSF parameters using the Green's function for radiative transport. For all geometries of the line forming region available in the current implementation of the model, I generally find that

the predicted CRSFs are too deep and possess significant emission wings, leading to difficulties when matching the observed spectra. The slab 1-0 geometry, where the continuum is illuminating the bottom of the accretion column, has the smallest emission wings of the geometries tested and is therefore a good candidate for a first approach. Assuming partial covering of the continuum leads to a further reduction of the remaining emission wings. This approach is motivated by the idea that only a part of the continuum contribution emerges from the line forming region. The results are encouraging and in good agreement with the previous phenomenological approach.

For the phase resolved analysis I created pulse profiles in different energy bands over the whole observation. They show a main peak and a much smaller secondary peak which is only seen at lower energies. Compared to other sources, e.g., Vela X-1 or GX 301−2, the pulse profile is rather smooth and does not show a complex shape at lower energies. The main peak is more pronounced at lower energies and slightly asymmetric, steeper in the rise, at higher energies. Comparing with Nagase et al. (1992), where a clear double peaked profile at lower energies has been observed, we assume that this is a luminosity dependent effect on the pulse profile. During the observation of Nagase et al. (1992), Cen X-3 was fainter than during our second orbit and no changes in the pulse profiles have been observed throughout this observation.

For each bin in the pulse profile we extracted a spectrum to study the evolution of the parameters over the pulse. For better statistics I combined some of the data in the pulse minimum, resulting in 24 phase bins overall. The continuum parameters show some significant changes throughout the pulse and the general N_{H}-Γ-correlation seems not to be valid during the main peak.

The CRSF shows significant changes throughout the pulse. The shape of the changes is very similar to the pulse profile shifted by $\Delta\phi_{\mathrm{pulse}} = 0.1$, not including the two maximum values during the rise. These outliers have rather large uncertainties and should be handled with caution in the interpretation. From the main peak on, E_{cyc} slowly decreases to below 30 keV where it stays for the remainder of the pulse. Figure 4.10 shows how the magnetic field deduced from

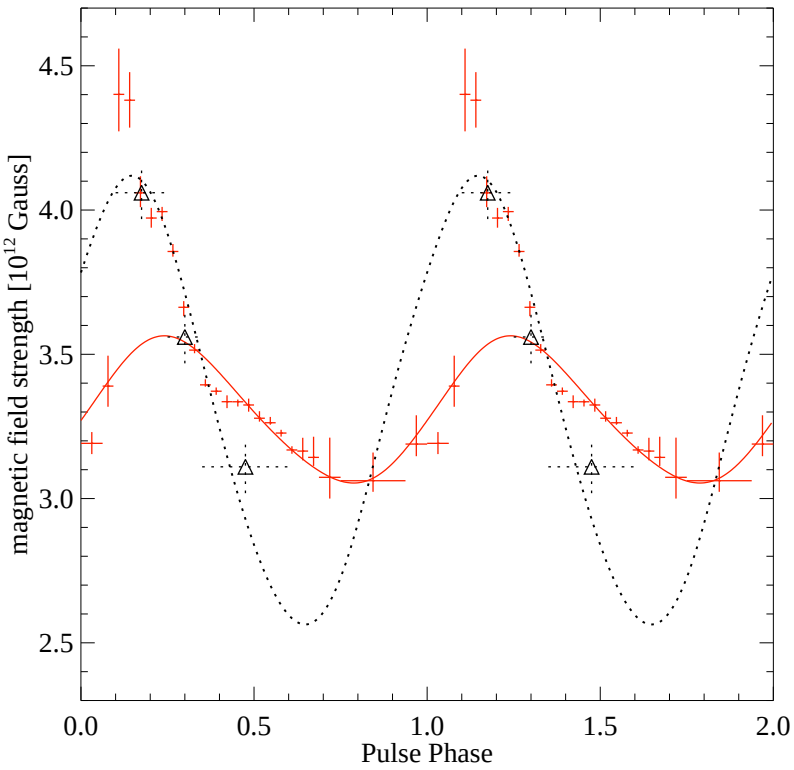

Figure 4.10 Calculated magnetic field strengths (crosses) and B00 results (triangles) using the CRSF centroid energy. Dotted line show the single dipole model using parameters from B00. Solid line show the best fit of the single dipol model to my data.

these measurements varies as a function of pulse phase. The figure also shows the earlier *BeppoSAX* measurements of B00, which are consistent with our much finer resolved data.

B00 argued that the large variation in B-field with pulse phase could not be due to a variation of the height in the accretion column at which the observed radiation originates, since this variation would imply height differences of kilometers. B00 instead argue that, based on earlier studies of the pulse shape of Cen X-3 by Leahy (1991), the polar cap of Cen X-3 is rather large. If this assumption is true, then it is likely that different locations on the neutron star's surface are observed over one rotation of the neutron star. Using the assumption that the observed X-rays are only produced by one of the two magnetic poles, and furthermore assuming that the observed X-rays are all coming from a location at a

constant geographical colatitude of the neutron star (taken by B00 to be the system's inclination), B00 then show that the variation of the B-field at the neutron star's surface produced by a magnetic dipole offset by $0.1\,R_{\rm NS}$ from the rotational axis of the neutron star can explain the B-field variation seen by *BeppoSAX*. I reproduce their best-fit model in Fig. 4.10. While the model is sufficient to explain the *BeppoSAX*-data, the higher resolution *RXTE*-data clearly show that it is not a viable explanation for the observed B-field variation. I extended the approach of B00 by allowing for observations of both magnetic poles and by also removing the constraint that the colatitude at which the X-rays originate equals the inclination. Neither of these approaches resulted in statistically satisfying descriptions of the variation of B with $\phi_{\rm pulse}$. Even when relaxing the model assumptions further, by using a skew-symmetric magnetic dipole, which approximates higher multipole moments for the B-field on the surface, and assuming that the X-rays come from two different locations on the neutron star, no satisfying description of the observed line variation was found. I therefore conclude that the model of B00 is not a viable description of the high resolution B-field variation seen here.

I note that an alternative study of the pulse profile of Cen X-3 has been presented by Kraus et al. (1996). Similar to the assumptions outlined above, these authors show that the shape and energy dependence of the pulse profile can be explained by emission from a distorted magnetic dipole. Taking into account the relativistic photon propagation close to the neutron star, Kraus et al. (1996) show that, in order to explain the pulse profile, both magnetic poles must contribute to the observed emission. Modeling observations of Cen X-3 made at a similar luminosity state as the one during the *RXTE* observation, Kraus et al. (1996) show that these assumptions yield an offset of approximately 10° for both poles, and that both poles contribute equally to the observed flux. In these models, they assume that the polar cap's radiation characteristic is a pen- plus pencil-beam pattern. A major result of these models is that in this decomposition the main pulse emission is dominated by the magnetic pole facing toward the observer, while the wings of the main pulse are dominated by the pole facing away from the observer. Although they do not take the height of the accretion column into account, I believe it is

likely that for geometric reasons the X-rays observed from the magnetic pole on the neutron star hemisphere facing away from the observer originate at a distance farther away from the neutron star surface, and thus in a region of lower B-field. Together with the possibility of slightly different surface magnetic strengths at both poles, I therefore deem it likely that the observed B-field variation over the X-ray pulse is due to us observing the two accretion columns at different heights, although further modeling of such a geometric setup is clearly required before a final answer on the origin of the B-field variation can be given.

This chapter is a reprint of the published publication: Suchy, Slawomir; Pottschmidt, Katja; Wilms, Jrn; Kreykenbohm, Ingo; Schnherr, Gabriele; Kretschmar, Peter; McBride, Vanessa; Caballero, Isabel; Rothschild, Richard E.; Grinberg, Victoria, "Pulse Phase-resolved Analysis of the High-Mass X-Ray Binary Centaurus X-3 over Two Binary Orbits ", The Astrophysical Journal, 2008, 675, 1478.

Chapter 5

1A1118-61

This chapter is primarily based on the *Suzaku* observations (Suchy et al., 2011b) of the transient HMXB 1A 1118−61 during its 2009 outburst. In addition, I was also very strongly involved in the analysis of the *RXTE* data of the same outburst (Doroshenko et al., 2010b) where the CRSF was first observed.

5.1 Overview

The Be/X-ray binary transient 1A 1118−61 was serendipitously discovered during an observation of the nearby binary system Cen X−3, when an outburst was detected in December of 1974 by the *Ariel-5* satellite (Eyles et al., 1975). A second, similar outburst occured in January of 1992 and was observed by the Burst and Transient Source Experiment on the Compton Gamma Ray observatory *CGRO*/BATSE (Coe et al., 1994). The measured peak flux was $\sim$ 150 mCrab for the 20-100 keV energy range, similar to the 1974 outburst. The source showed an elevated emission throughout the next $\sim$ 30 days after the decay of the main outburst (see Figure 1 in Coe et al., 1994). The third and most recent outburst occurred on 2009, January 4 and was detected by the *Swift* Burst Alert Telescope BAT (Mangano et al., 2009; Mangano, 2009). It reached a peak flux of $\sim$ 500 mCrab. This last outburst was monitored with *Swift* and *RXTE* as well as with two long pointed *Suzaku* observations and one observation with *INTEGRAL* during a flaring episode $\sim$ 50 days after the peak of the main outburst (Leyder

et al., 2009).

Pulsations with a period of 405.3 ± 0.6 s were observed during the 1974 outburst and were initially attributed to the orbital period of two compact objects (Ives et al., 1975). Shortly afterwards it was suggested that the period stems from a slow rotation of the neutron star (NS) itself (Fabian, 1975). During the 1992 outburst pulsations with a period of ~ 406.5 s were detected up to 100 keV, showing a broad, asymmetric, single peak pulse profile above the lowest BATSE energy of 20 keV. The pulse period decreased throughout the decline of the outburst with a rate of ~ -0.016 s/day and it appeared constant at ~ 406.35 s for the time of the elevated emission. During the 2009 outburst a similar period evolution was observed with *RXTE* resulting in a pulse period of $P_{\rm spin} = 407.719$ s, and $\dot{P}_{\rm spin} = -4.6 \times 10^{-7}$ s/s ≈ -0.04 s/day (Doroshenko et al., 2010b). Furthermore, the lower energies showed a more complex pulse profile with two peaks below an energy of ~ 10 keV. Due to the short duration of the *Suzaku* observations with respect to the pulse period, the derived *RXTE* values are used for determining the pulse profile and phase resolved spectra in this paper.

The optical counterpart was identified as the Be-star Hen 3−640/Wray 793 by Chevalier & Ilovaisky (1975) and classified as an O9.5IV-Ve star with strong Balmer emission lines indicating an extended envelope by Janot-Pacheco et al. (1981). The overall spectrum was found to be similar to other known Be/X-ray transients, such as X−Per and A 0535+26 (Villada et al., 1992, and references therein). The distance was estimated to be 5 ± 2 kpc (Janot-Pacheco et al., 1981) and was confirmed by Coe & Payne (1985), along with the spectral type classification, using UV observations of the source. Observed X-ray emission with *EXOSAT* from 1A 1118−61 between outbursts (Motch et al., 1988), indicated a continuous low level of accretion. Rutledge et al. (2007) reported on pulsations in the low luminosity state observed with *Chandra*, making it only the third known HMXB transient after A 0535+26 and 4U 1145-619 for which this behavior has been observed.

A study of the $H\alpha$ emission line before and during the 1994 outburst showed a strong correlation between its strength and the observed X-ray activity, indicating

the existence of a very large disk around the star. The fluctuation of the equivalent width of $H\alpha$ indicated possible instabilities in the disk, which were enhanced when the star passed through the periastrion. The analysis of the UV continuum and line spectra has indicated that the photospheric emission from the Be star was not affected by the X-ray radiation, similar to the case of A 0535+26 (de Loore et al., 1984).

Until recently, the orbit of 1A 1118−61 was not measured and assumed values were of the order of 350 days, based on the $P_{spin} - P_{orb}$ relation (Corbet, 1986), and $\sim$ 585 days based on the equivalent width of the $H\alpha$ line (Reig et al., 1997). Staubert et al. (2010) analyzed the pulse arrival time in *RXTE* data throughout the 2009 outburst and established an orbital period of $\sim$ 24 days with a very circular orbit around the Be-companion.

Spectral fitting during the 1974 outburst indicated a variable power law index, where the lowest value was $\sim$ 0.9 during the peak of the outburst, and $\sim$ 1.1 before and after (Ives et al., 1975). Coe et al. (1994) described the 1992 *CGRO*/BATSE data with a single-temperature, optically-thin, thermal bremsstrahlung (OTTB) with a temperature of 15 keV. Due to the different energy range of the instrument and the fact that pulse−off-pulse data have been used, these results can not be directly compared with the 1974 observation.

In the 2009 outburst Doroshenko et al. (2010b) discovered a CRSF at $\sim$ 55 keV making it one of the highest observed centroid energies in all known CRSF sources.

Suzaku observed 1A 1118−61 twice in 2009, once during the peak of the outburst and again $\sim$ 13 days later when the flux had returned to a level slightly above the quiescent state. In this chapter I will present the first detailed 0.7-200 keV broad band spectrum for this source with the discovery of the CRSF at 55 keV in the *RXTE* and *Suzaku* data. A possible first harmonic at $\sim$ 110 keV, twice the fundamental energy, was not significantly detected and only indicated in the data.

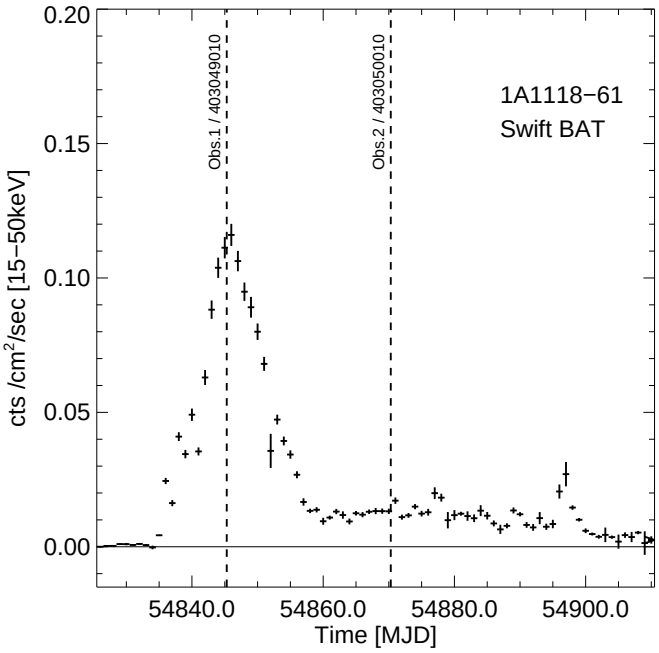

Figure 5.1 *Swift*/BAT light curve of 1A 1118 during its 3rd observed outburst. The vertical lines indicate the *Suzaku* observations discussed here.

5.2 Observation and Data Reduction

A sudden increase in activity of 1A 1118-61 was detected with the *Swift*/BAT instrument on January 4th, 2009 (Mangano et al., 2009). The count rate increased steadily until January 15th when it reached the maximum value of ~ 500 mCrab and then decayed until January 27th where it showed a low emission level with a brief period of flaring (Leyder et al., 2009) until mid March and then returned to quiescence (see Fig. 5.1). *Suzaku* observed 1A 1118−61 during the peak of the outburst on January 15th, 2009 (MJD 54846.5, ObsID 403049010) with both of its main instruments: the X-ray Imaging Spectrometer (XIS; Mitsuda et al., 2007) and the Hard X-ray Detector (HXD; Takahashi et al., 2007). A second observation was performed on January 28th, 2009 (MJD 54859.2, ObsID 403049010), ~ 13 days after the main outburst, at the beginning of the period of elevated emission.

Both observations were performed using the HXD nominal pointing to minimize the pile-up fraction in the XIS instruments and to enhance the HXD sensitivity for a possible CRSF detection. To reduce pile-up, the XIS instruments were

operated with the 1/4 window option, a readout time of 2 s and the burst option with only 1 s accumulation time for each readout cycle, reducing the exposure time for the XIS instruments by 50%. The data were taken in the 3×3 and 5×5 editing modes which were then combined for the final spectral analysis.

For the extraction the *Suzaku* FTOOLS version 16 (part of HEASOFT 6.9) was used. The unfiltered XIS data were reprocessed with caldb20090402 and then screened with the standard selection criteria as described in the ABC guide[1]. Each detector and editing mode combination was extracted independently and individual response matrices and effective area files were created. For the final spectra the data from both FI detectors were combined (XIS 0&3) and the BI data was left separate. The response matrices and effective areas were weighted according to the accumulated exposure time of the different modes. The XIS data were grouped so that the minimum number of channels per energy bin corresponded to at least the half width half maximum of the spectral resolution, i.e. grouped by 8, 12, 14, 16, 18, 20, 22 channels starting at 0.5, 1, 2, 3, 4, 5, 6, and 7 keV, respectively (Nowak, priv. com).

For the HXD data the *Suzaku* team provided the tuned PIN non X-ray background[2] (NXB). Following the ABC Guide the cosmic X-ray background (CXB) was simulated and the exposure time was adjusted in both backgrounds by the prescribed factor of 10. The PIN data were grouped so that at least 100 events were detected in each spectral bin.

GSO data were extracted using the FTOOL `hxdpi` with the newest gain calibration file from April, 2010. The NXB background files version 2.4 created by the *Suzaku* HXD instrument team were used. The data were then binned to 64 bins according to the Suzaku homepage[3]. GSO data in the range $70-200$ keV were used in the spectral analysis.

[1] http://heasarc.gsfc.nasa.gov/docs/suzaku/analysis/abc/
[2] http://heasarc.nasa.gov/docs/suzaku/analysis/pinbgd.html
[3] http://heasarc.gsfc.nasa.gov/docs/suzaku/analysis/gso_newgain.html

5.2.1 Pileup correction

For bright sources, such as 1A 1118−61 during the outburst, a strong pileup is expected. To measure the pileup in the two observations, a few steps have to be performed in the data reduction. First, the S-lang routine `aeattcor.sl`[4] was used to improve the attitude correction file and the point spread function of the events. Then the tool `pile_estimate.sl` was applied to produce a 2 dimensional map of the pileup fraction. The maximum values for pileup fractions were 10% and 15% for XIS0, 15% and 16% for XIS1, and 18% and 21% for XIS3 for the 3×3 and 5×5 editing modes, respectively. Regions with a pileup fraction above 5% were excluded from the extraction for each individual source event file. For the second observation the calculated maximum pileup fractions were $< 5\%$ and no regions had to be excluded for the extraction.

5.3 Phase averaged spectrum

For the outburst observation broad band I extracted XIS spectra in the energy range 0.7−12 keV (0.7−10 keV for the BI XIS1), PIN spectra for 12–70 keV and GSO spectra for 70–200 keV. For the second observation the GSO spectrum was not well constrained and therefore was not included in the analysis. The final model included the Galactic and intrinsic absorption, a continuum that steepened at higher energies, an iron line complex, and a CRSF. A low energy component in excess of the absorbed power law was modeled with a black body component. In addition a 10 keV absorption feature was required in the outburst observation.

The Galactic column density was modeled with a single photon absorption (`phabs`) component, where the column density was confined between 1.1 and 1.4 $\times 10^{22}\,\mathrm{cm}^{-2}$. The value for the Galactic line-of-sight column density determined by the NASA N_{H} Tool[5] for 1A 1118−61 is $1.22 \times 10^{22}\,\mathrm{cm}^{-2}$. For the outburst observation the value was restrained to leave some leeway due to the uncertainty of the distance to the source. For a better constraint, the values for the Galac-

[4]http://space.mit.edu/ASC/software/suzaku/

[5]http://heasarc.gsfc.nasa.gov/cgi-bin/Tools/w3nh/w3nh.pl

tic column were frozen to the outburst numbers in the second observation. The intrinsic column density was modeled with the partially covered photon absorption model `pcfabs` to take the flux at lower energies ($< 1\,\mathrm{keV}$) into account. All modeling was performed using the `wilm` abundances (Wilms et al., 2000) with the `vern` cross-sections (Verner et al., 1996). The continuum was modeled using a power law with an exponential cutoff (`cutoffpl`). Using a power law with a Fermi-Dirac (FD) cutoff, one of the empirical models often applied to accretion powered pulsars, resulted in a cutoff energy of ~ 0, making the FD cutoff effectively a `cutoffpl` (see chapter 3 for details), where the variable E_{cut} actually reflects the folding energy of the model. The additional 10 keV feature was modeled using a negative, broad ($\sigma = 1 - 2\,\mathrm{keV}$) Gaussian component. Such a feature has been previously observed in different sources and it is believed to stem from an improper modeling of the continuum (see chapter 3). More recent examples of such a feature are, e.g. 4U1907+09 (Rivers et al., 2010) and Cen X−3 (chapter 4). When including this feature in the overall best fit, the χ^2/dofs (degrees of freedom) decreased from 1173/477 to 678/474, respectively. Due to the small differences in the instrument response, all detectors were coupled with a normalization constant, which was set to 1 for the combined XIS 03 detectors. The final model is of the form `const*phabs*pcfabs*(cutoffpl*gabs+2*Gauss`$_{\mathrm{Fe}}$`)+Gauss`$_{10\,\mathrm{keV}}$`+3*Gauss`$_{\mathrm{Cal}}$. The best fit parameters are mentioned in the text and partially summarized in Table 6.1.

A second approach for the continuum was initiated by Doroshenko et al. (2010b) using the Comptonization model `compTT` developed by Titarchuk & Hua (1995) instead of the `cutoffpl` model. The parameters of the `compTT` were again left independent between the FI XIS03 and the BI XIS1, but only small differences could be observed. The negative Gaussian at 10 keV was not necessary for this model. When comparing the spectral parameters in the outburst between these two models, i.e. CRSF, N_{H} and the spectral lines, to the previously described `cutoffpl`, the values were consistent.

A comparison of the `compTT` values, such as the photon seed temperature T_0, the plasma Temperature kT_{e} or the optical depth τ_p showed consistency between

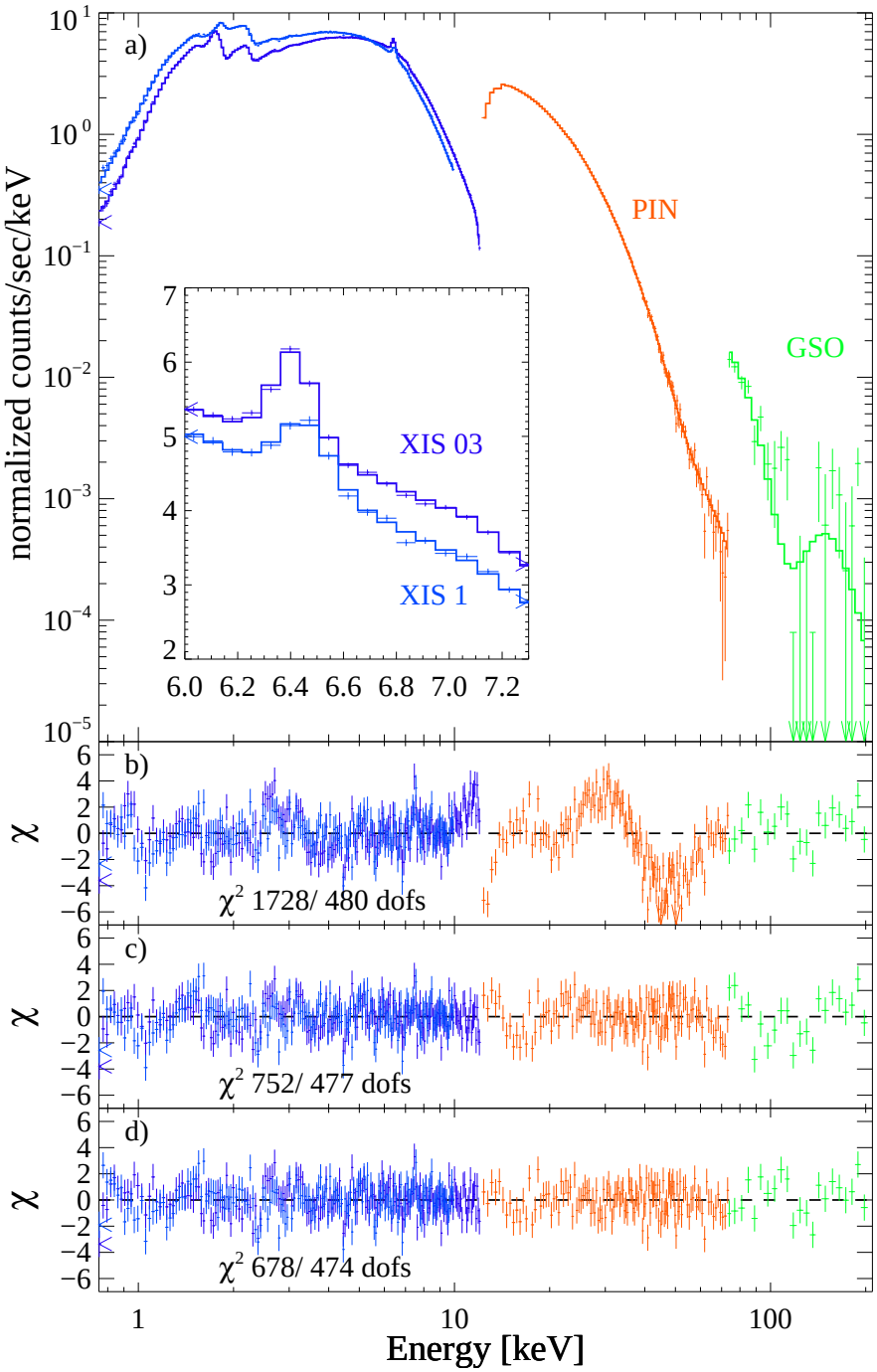

Figure 5.2 Broad band phase averaged spectrum of the outburst observation using the `cutoffpl` model. The residuals are shown without CRSF (b), with one CRSF at 55 keV (c) and with the second CRSF at 112 keV. The inset shows the Fe line region and the best fit model for XIS1 and XIS 03.

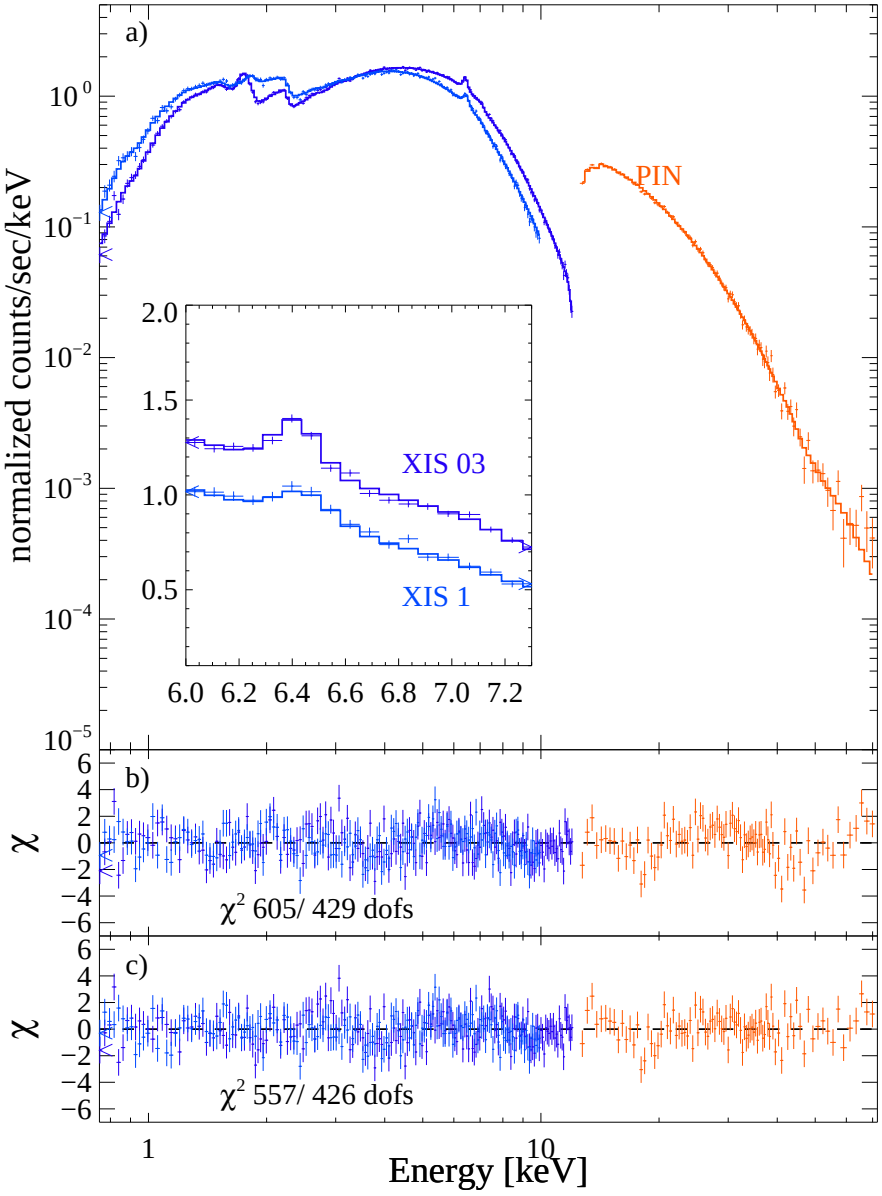

Figure 5.3 Broad band phase averaged spectrum of the second observation using the `cutoffpl` model. Only XIS and PIN data were used. Residuals without a CRSF (b) and with one CRSF at $\sim 47\,\mathrm{keV}$. The Inset shows the Fe line region and the best fit model for XIS1 and XIS 03.

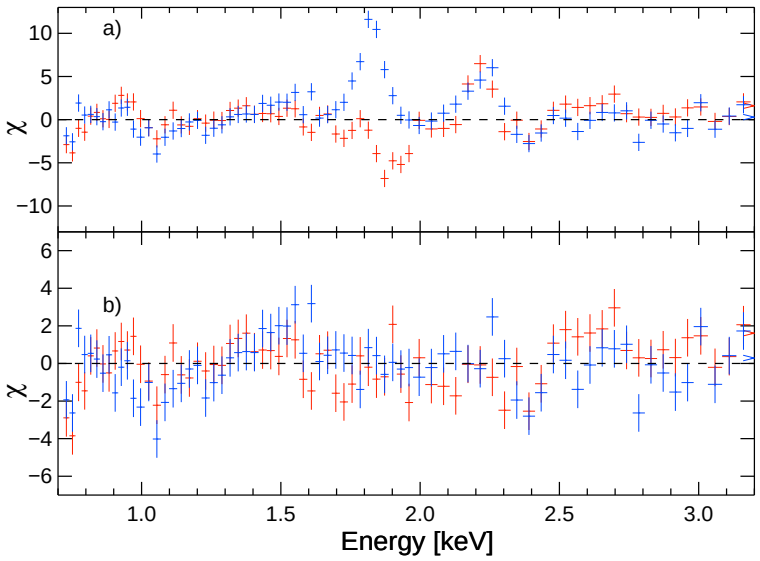

Figure 5.4 Instrumental residuals at lower energies for XIS 1 (blue) and XIS 03 (red) with the `cutoffpl` model. The clearly apparent lines are the energies of the Au Kα edge at ~ 2.1 keV and the Si Kα edge at ~ 1.8 keV. Additionally a possible Ni Kα edge at ~ 0.9 helps to improve the fit slightly. The uncertain modeling of the elemental edges, results in the appearance of line like structures around these energies.

the spectra of the outburst as seen by *Suzaku* and *RXTE* (Doroshenko et al., 2010b).

When comparing the outburst spectrum with the second observation, significant changes in the continuum parameters are observed. In the `cutoffpl` model the power law index softens from $0.350^{+0.022}_{-0.004}$ to $1.01^{+0.03}_{-0.03}$. The cutoff energy $E_{\rm cut}$ increased from $18.7^{+0.2}_{-0.2}$ keV during the outburst to $24.7^{+1.8}_{-1.6}$ keV in the second observation. The temperature of the additional black body decreased from $0.51^{+0.01}_{-0.003}$ keV to $0.15^{+0.01}_{-0.01}$ keV after the outburst. The intrinsic column density and covering fraction increased both from $11.2^{+0.2}_{-0.3} \times 10^{+22}\,\mathrm{cm}^{-2}$ and $0.66^{+0.01}_{-0.01}$ in the outburst to $13.6^{+0.5}_{-0.5} \times 10^{+22}\,\mathrm{cm}^{-2}$ and $0.71^{+0.01}_{-0.01}$ in the second observation.

In the `compTT` model the changes between the two observations were similar. The intrinsic column density and black body values were consistent with the values obtained with the `cutoffpl` model, where the intrinsic column density is $12^{+0.4}_{-0.5} \times 10^{12}\,\mathrm{cm}^{-2}$ and $15.1^{+0.1}_{-0.7} \times 10^{12}\,\mathrm{cm}^{-2}$ and the covering fraction is $0.71^{+0.01}_{-0.01}$ and $0.76^{+0.01}_{-0.01}$ for the outburst and the second observation, respectively. When

establishing the errors for the other spectral parameters of the continuum, these values had to be frozen to avoid a drift into an unreasonable part of the parameter space. The black body temperature declined from $0.53^{+0.01}_{-0.01}$ keV to $0.13^{+0.01}_{-0.01}$ keV, similar values as in the `cutoffpl` model. The `compTT` values changed significantly between the two observations. The photon seed temperature decreased from $1.34^{+0.04}_{-0.04}$ to $0.44^{+0.06}_{-0.04}$ keV. The electron plasma temperature $kT_{\rm e}$ increased from $7.6^{+0.3}_{-0.3}$ to 182^{+158}_{-96} keV, whereas the depth of the plasma τ_p decreased from $6.00^{+0.19}_{-0.18}$ to $0.68^{+1.33}_{-0.25}$. This behavior reflects the known negative $kT_{\rm e}$ and τ_p correlation (see Section 5.5.3).

5.3.1 Fe line component

An Fe Kα emission component was detected at $6.414^{+0.006}_{-0.002}$ keV in the outburst data (see Fig. 5.2, Inset), as well as at $6.42^{+0.01}_{-0.01}$ keV in the 2nd observation (see Fig. 5.3, Inset). For the best fit values the centroid energies of XIS03 and XIS 1 were left independent, due to a known shift in the energy calibration. Although the centroid energies for XIS1 generally show a slightly lower (30 eV) energy than the other XIS instruments[6], the XIS1 data here actually showed a 20-30 eV higher centroid energy. Residuals at ~ 7 keV were observed and were modeled with an additional Gaussian line with a best-fit energy of 7.13 ± 0.03 keV, indicating the existence of an Fe Kβ line. The width σ of the Fe Kβ line was set to the Fe Kα line value, and the normalization was left independent. The obtained value for the Kβ normalization was consistent with the expected 12% of the Kα normalization for neutral or nearly neutral ionization of iron. In the second observation the second line was very weak and its parameters could not be properly constrained. In this case the line centroid was frozen at the outburst value of 7.13 keV. The width was again coupled with the Fe Kα value. The residuals decreased from $\chi^2 = 721$ for 477 dofs to the best fit values of 678 for 474 dofs when the Fe Kβ line was included and an F-test showed only a 2.8×10^{-6} % probability that this improvement is of a statistical nature. Another possibility for modeling the observed residuals at ~ 7 keV is the addition of an Fe K-edge, located at 7.1 keV. When including the

[6] http://www.astro.isas.jaxa.jp/suzaku/process/caveats/caveats_xrtxis06.html

edge, the improvement is only marginal (χ^2 of 712 for 474 dofs) and the best fit energy is ~ 7.6 keV. Freezing the energy to the value of 7.1 keV did not improve the fit. The remaining residuals indicated that an additional Fe Kβ line would still be necessary. The measured energies of the Fe Kα and Kβ lines were slightly higher than the expected laboratory values, but still of the same order of magnitude of the energy scale uncertainties of the instrument ($\sim \pm$ 20 eV @ 6 keV according to the ABC guide).[7]

Comparing the equivalent widths (EQWs) of the Fe Kα and Kβ lines in the two observations showed no significant change during the outburst. The Fe Kα line showed an EQW of 51 ± 4 eV for both models, whereas the Fe Kβ line showed an EQW of 8 ± 3 eV for the `cutoffpl` model and 10 ± 3 eV in the `compTT` model. For the second observation, the Fe Kα EQWs were 46 ± 10 eV and 48 ± 10 eV, and the Kβ EQWs were 8 ± 2 eV and 11 ± 9 eV for the `cutoffpl` and `compTT` models, respectively. The similarity of the Fe line EQW between both observations indicates that the source of the Fe lines is near to the source of the continuum.

5.3.2 CRSF

In the burst observation a strong residual at $\sim$ 50 keV was observed in the HXD (Fig. 5.2, b). When including a CRSF-like feature with a Gaussian optical depth profile (`gabs`) the best fit was obtained with a centroid energy of $58.2^{+0.8}_{-0.4}$ keV, significantly improving the χ^2 from 1728 with 480 dofs to 752 for 477 dofs for the `cutoffpl` model, confirming the discovery of the CRSF in the *RXTE* data by Doroshenko et al. (2010b). The width of the line was $14.1^{+3.5}_{-3.1}$ keV and the optical depth τ was $60.1^{+5.9}_{-1.5}$. Using the `compTT` model, similar values for $E_{\rm cyc}$ and σ were obtained for the outburst data. In this case the optical depth was found to be $23.6^{+10.4}_{-6.9}$.

In the `cutoffpl` model, a second absorption line, using the `gabs` model, in the GSO data of the outburst spectrum at $\sim$ 110 keV improved the χ^2 to 678 with 474 dofs (see Fig. 5.2c). An F-test probability of 1.6×10^{-10} indicates that the line

[7] An inflight energy calibration using the Mn-calibration sources of the XIS detectors could not be performed, due to the usage of the 1/4 window mode, which excludes the corner regions where the calibration sources are located.

is significantly detected. However, an increase of the GSO Non X-ray Background (NXB) by 1 or 2% decreased the GSO counts to a non-detectable value. Another possible systematic effect is the decay of the ^{153}Gd instrumental line, which is activated when the satellite passes through the south atlantic anomaly (SAA), and thus creating a broad background line at $\sim 150\,\mathrm{keV}$. This could impose a deviation at $\sim 120\,\mathrm{keV}$ if not accurately represented in the modeled background. Therefore caution is advised when interpreting this feature.

In the lower luminosity observation the fundamental CRSF was marginally detectable (see Fig. 5.3). To test for the existence of a CRSF, the centroid energy and width were fixed to the outburst values, and the optical depth was left as a free parameter. With the addition of the CRSF, the `cutoffpl` model improved slightly from a χ^2/dofs of 605 / 429 to 592 / 428 with an optical depth of $\tau = 15.3 \pm 6.3$. An F-test showed a 0.2% probability that this component is just statistical noise. When leaving the CRSF parameters free, the centroid energy decreased to $47.4^{+3.2}_{-2.3}\,\mathrm{keV}$. With a χ^2/dofs of 572 / 426 the best fit improved further and the F-test probability reduced to 2.6×10^{-5} (see Tab. 6.1 for details).

For the `compTT` model, the addition of the CRSF with the frozen energy and width created residuals in the $10 - 20\,\mathrm{keV}$ range, which could be significantly reduced by decoupling the optical depth of the `compTT` model in the PIN data from the XIS data. The best fit optical depth of the CRSF line was $27.1^{+3.2}_{-3.0}\,\mathrm{keV}$ changing the χ^2 values from 871 to 567 for 477 and 474 dofs, respectively. When leaving the CRSF parameters free, the width of the CRSF increased to $> 30\,\mathrm{keV}$, making it part of the continuum and tampering with the results. Freezing the CRSF parameters to the values obtained with the `cutoffpl` model did not result in a satisfactory overall fit.

An alternative approach to describe the CRSF is to replace the `gabs` model with the XSPEC model `cyclabs` (Mihara et al., 1990), providing the resonance energy E_{res}, the resonance width σ_{res} and the resonance depth τ_{res}. Using this model does not improve the fits significantly, and actually results in a slightly worse χ^2/dof value of 782 / 475 for the outburst data. Note that in the case of `cyclabs` the ratio between the energy of the fundamental and first harmonic

line are fixed to 2, resulting in 1 more degree of freedom. The observed $E_{\rm res}$ of $49.5^{+0.8}_{-0.8}$ keV is of the order of $\sim 20\%$ below the centroid energy obtained with the `gabs` model. This discrepancy stems from the use of a different calculation of the line energy and is of the order of $10 - 20\,\%$ lower than the measured `gabs` energy (see Nakajima et al., 2010, for details). A width of $\sigma_{\rm res} = 19.4^{+2.8}_{-1.3}$ keV and a depth of $\tau_{\rm res} = 1.45^{+0.10}_{-0.06}$ are obtained for the outburst observation. In the second observation the resonance energy shows a slight decrease ($E_{\rm res} = 45.7^{+2.3}_{-2.0}$ keV), and only slightly smaller than the `gabs` values. These results reflect again the difficulty of constraining the CRSF parameters in the second observation. The width and depth, $\sigma_{\rm res} = 5.6^{+3.7}_{-2.4}$ keV and $\tau_{\rm res} = 0.46^{+0.19}_{-0.14}$, are consistent with the `gabs` result showing a decrease in width and depth for both observations. These results support the picture of the CRSF that there might be a luminosity dependent shift in the centroid energy.

Table 5.1. Phase averaged spectral parameter. Model described in the Text.

Parameter	Cutoffpl			Parameter	CompTT	
Outburst	2nd Obs.	2nd Obs.*		CompTT	Outburst	2nd Obs.
phabs $N_{\rm H}[10^{22}/{\rm cm}^2]$	$1.34^{+0.01}_{-0.01}$	1.34 frozen	$1.43^{+0.14}_{-0.13}$		$1.28^{+0.03}_{-0.02}$	1.28 frozen
pcfabs $N_{\rm H}[10^{22}/{\rm cm}^2]$	$11.2^{+0.2}_{-0.3}$	$13.5^{+0.4}_{-0.4}$	$13.6^{+0.5}_{-0.5}$		$12.00^{+0.4}_{-0.5}$	$15.1^{+0.1}_{-0.7}$
covering fract.	$0.66^{+0.01}_{-0.01}$	$0.71^{+0.01}_{-0.01}$	$0.71^{+0.01}_{-0.01}$		$0.71^{+0.01}_{-0.01}$	$0.76^{+0.01}_{-0.01}$
blackbody kT [keV]	$0.51^{+0.01}_{-0.003}$	$0.15^{+0.01}_{-0.01}$	$0.15^{+0.01}_{-0.01}$		$0.53^{+0.01}_{-0.01}$	$0.17^{+0.01}_{+0.01}$
blackbody norm $[10^{-3}]$	$7.3^{+0.4}_{-0.2}$	$2.2^{+0.2}_{-0.03}$	$2.85^{+1.67}_{-1.22}$		$12.8^{+1.1}_{-0.9}$	$2.89^{+0.03}_{-0.02}$
$E_{\rm cut}$ [keV]	$18.74^{+0.24}_{-0.18}$	$26.3^{+3.0}_{-2.5}$	$24.7^{+1.8}_{-1.6}$	T_0 [keV]	$1.34^{+0.04}_{-0.05}$	$0.44^{+0.06}_{-0.04}$
Γ	$0.350^{+0.022}_{-0.004}$	$1.02^{+0.04}_{-0.04}$	$1.01^{+0.03}_{-0.03}$	kT [keV]	$7.57^{+0.34}_{-0.26}$	182^{+158}_{-96}
$A_{\rm pl}[10^{-2}]^\dagger$	$9.55^{+0.02}_{-0.03}$	$5.8^{+0.3}_{-0.3}$	$5.7^{+0.3}_{-0.3}$	$\tau_{\rm p}$	$6.00^{+0.19}_{-0.18}$	$0.68^{+1.33}_{-0.26}$
				norm†	$0.096^{+0.003}_{-0.003}$	$0.002^{+0.004}_{-0.001}$
$E_{\rm CRSF}$ [keV]	$58.2^{+0.8}_{-0.4}$	58.2 frozen	$47.4^{+3.2}_{-2.3}$		$54.5^{+2.36}_{-2.07}$	54.5 frozen
$\sigma_{\rm CRSF}$ [keV]	$14.1^{+3.5}_{-3.1}$	14.1 frozen	$5.7^{+2.0}_{-1.7}$		$10.3^{+3.6}_{-0.1}$	10.3 frozen
$\tau_{\rm CRSF}$ [keV]	$60.1^{+5.9}_{-1.5}$	$15.4^{+6.4}_{-6.3}$	$6.0^{+3.0}_{-2.1}$		$23.6^{+10.4}_{-6.9}$	$27.1^{+3.2}_{-3.0}$
$E^\dagger_{\rm Fe\ K\alpha}$ [keV]	$6.414^{+0.006}_{-0.002}$	$6.42^{+0.01}_{-0.01}$	$6.42^{+0.01}_{-0.01}$		$6.42^{+0.01}_{-0.01}$	$6.42^{+0.01}_{-0.01}$
$E^\ddagger_{\rm Fe\ K\beta}$ [keV]	$7.13^{+0.03}_{-0.03}$	7.13 frozen	7.13 frozen		$7.13^{+0.03}_{-0.03}$	7.13 frozen
Eq. Width Kα/Kβ [eV]	$51^{+4}_{-4}/8^{+3}_{-3}$	$46^{+10}_{-10}/8^{+2}_{-2}$	$46^{+10}_{-10}/8^{+2}_{-2}$		$51^{+4}_{-4}/10^{+3}_{-3}$	$49^{+10}_{-10}/11^{+9}_{-9}$
Flux$_{2-10\,{\rm keV}}[10^{36}$ ergs/sec $]^\ddagger$	8.79	1.72	1.72		9.15	1.72
$C_{\rm XIS1}/C_{\rm PIN}/C_{\rm GSO}$	0.98 / 1.10 / 0.82	1.02 / 1.01/–	1.02/1.01/–		0.99/ 1.18 / 1.10	0.95/ 1.00/–
$\chi^2_{\rm red.}$/dofs	1.43 / 474	1.33 / 431	1.31/428		1.42 / 478	1.32/ 427

Note. — $\star$ free CRSF, † Units in Photons keV^{-1} cm^{-2} s^{-1}, ‡ unabsorbed flux

5.3.3 Low energy calibration issues

Strong residuals at lower energies, i.e. between 1.5 and 2.5 keV (see Fig. 5.4) were observed in both data sets. A comparison with known background properties of the *Suzaku*/XIS instrument (Yamaguchi et al., 2006) showed that these features are identical to the known instrumental Si Kα and Au Kα lines, located at 1.74 keV and 2.12 keV, respectively. In many observations of bright sources, e.g. 4U 1907+07 (Rivers et al., 2010) and LMC X−3 (Kubota et al., 2010), these energy bands are explicitly excluded. In this case, modeling these lines with two Gaussian emission features was sufficient to minimize the residuals and improve the χ^2/dofs from 1295 / 483 (without the lines) to the best fit value of 678 / 474. Note that the Au Kα line at ~ 2.1 keV could be described by the same Gaussian emission line at 2.21 ± 0.01 keV for both FI and BI XIS instruments, whereas the Si Kα line appears as an emission line for the BI XIS1 at 1.82 ± 0.01 keV (Fig: 5.4, blue) and a negative Gaussian line at 1.89 ± 0.01 keV for the FI XIS 03 combination (Fig. 5.4, red), indicating that for the FI instrument the line is either over-subtracted or not properly energy calibrated, leading to a dip in the spectrum. By using two independent lines at 1.89 keV (FI) and 1.82 keV (BI) the residuals can be well described. An additional Gaussian component at $0.93^{+0.01}_{-0.02}$ keV, located close to the Ni K edge at 0.897 keV, slightly improves the residuals (χ^2/dofs of 731 / 477 without the line, instead of the best-fit value of 672 / 474) This improvement indicates a possible systematic error of the calibration at lower energies for bright sources. This line is not very pronounced and can be omitted when using the `compTT` model.

5.4 Phase resolved analysis

For a phase resolved analysis the XIS and PIN data of both observations were folded with the *RXTE* determined pulse period from Doroshenko et al. (2010b) of $P_{\rm spin} = 407.719$ s, $\dot{P}_{\rm spin} = -4.6 \times 10^{-7}$ s/s and the MJD epoch of 54841.62. Pulse profiles with 20 phase bins were created for five different energy bands in the $1 - 10$ keV energy range for XIS and $12 - 40$ keV energy range

for PIN for both observations (Fig. 5.5 and Fig. 5.6). The statistical quality of the GSO data precluded the creation of pulse profiles and further spectral analysis.

During the outburst the pulse profile consisted of two peaks, where the main peak (P1, pulse phase $0.3 - 0.6$) stayed dominant throughout all energy bands and became broader towards higher energies (Fig. 5.5). The second peak (P2, pulse phase $0.65 - 0.9$) disappeared at energies above $\sim 10\,\mathrm{keV}$, consistent with the *RXTE* observations by Doroshenko et al. (2010b). The third region in Fig. 5.5 indicates the minimum of the pulse profile (MIN, pulse phase $0.95 - 1.25$), as determined from the lower energies of the XIS instrument.

In comparison, the pulse profile of the second observation (Fig. 5.6) showed a similar Peak P1 throughout the whole energy band, although narrower at lower energies. No second peak was observed at the position of P2, although a small "bump" in the $5 - 12\,\mathrm{keV}$ energy range was still visible. At lower energies, i.e. for the $3 - 5$ and $5 - 12\,\mathrm{keV}$ energy band, a small peak showed up on the opposite site of P1, the pulse phase where the minimum was defined in the outburst data.

5.4.1 Phase resolved spectroscopy

Spectra were extracted for three different pulse phases throughout the outburst: P1, P2 and MIN. XIS and PIN spectra were used and the same XIS grouping as in the phase averaged data was applied. The PIN data was again grouped to include at least 100 counts per spectral bin. The same spectral model was used as in the phase averaged analysis and the best-fit results are summarized in Table 6.2. In all pulse phases the CRSF component was visible in the spectra. Throughout the pulse phase the best-fit values for the galactic and intrinsic N_{H} values did not change significantly. Note that in both models a slight decrease of the covering fraction during P2 can be observed.

The most significant variation in the `cutoffpl` model was that of the cutoff energy E_{cut} which decreased from 30 keV in P1, to 18.3 keV in P2 and down to 10.7 in MIN. At the same time the power law index Γ varied from $0.42^{+0.06}_{-0.04}$ (P1), to $0.56^{+0.04}_{-0.02}$ (P2), and to $-0.13^{+0.09}_{-0.08}$ for MIN. In the three phases the CRSF centroid energy changed from $66.6^{+0.9}_{-2.3}\,\mathrm{keV}$ in P1, and declined to $55.5^{+0.5}_{-0.7}\,\mathrm{keV}$ throughout

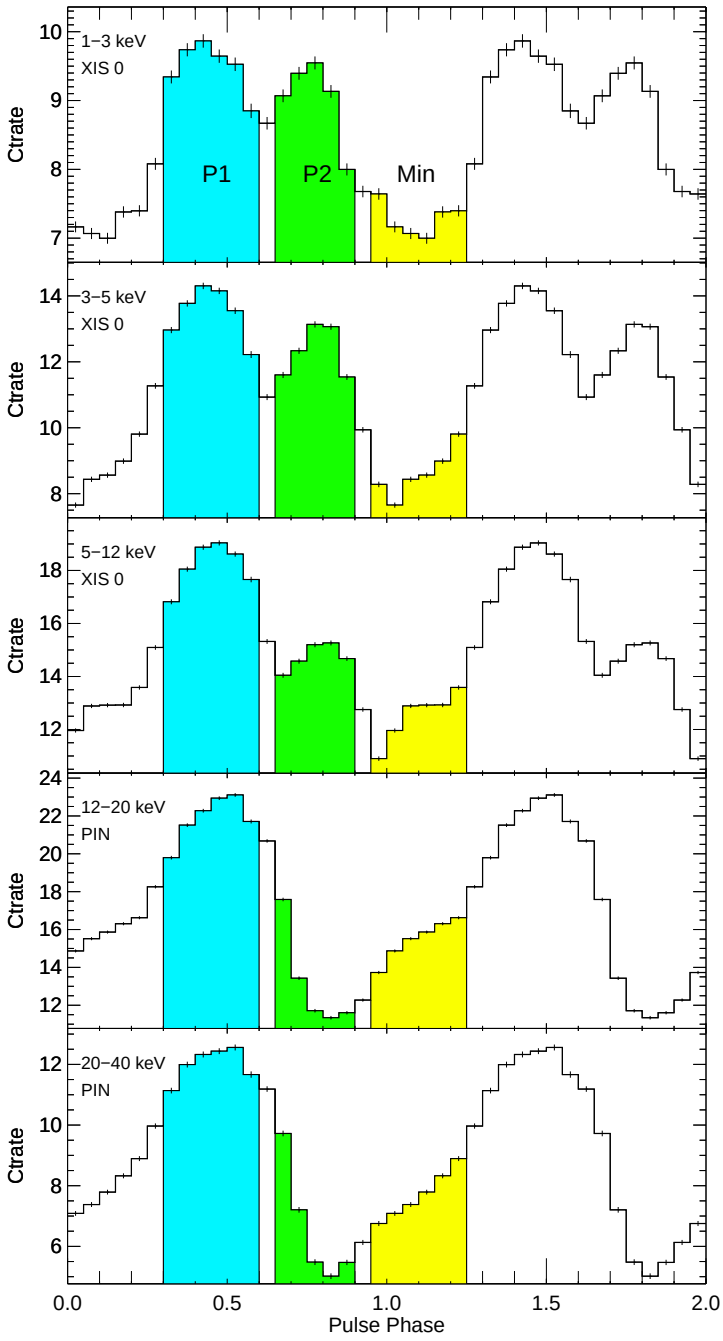

Figure 5.5 XIS and PIN pulse profiles for different energy bands for the outburst observation. P1, P2 and MIN indicate the regions used for the phase resolved spectral analysis.

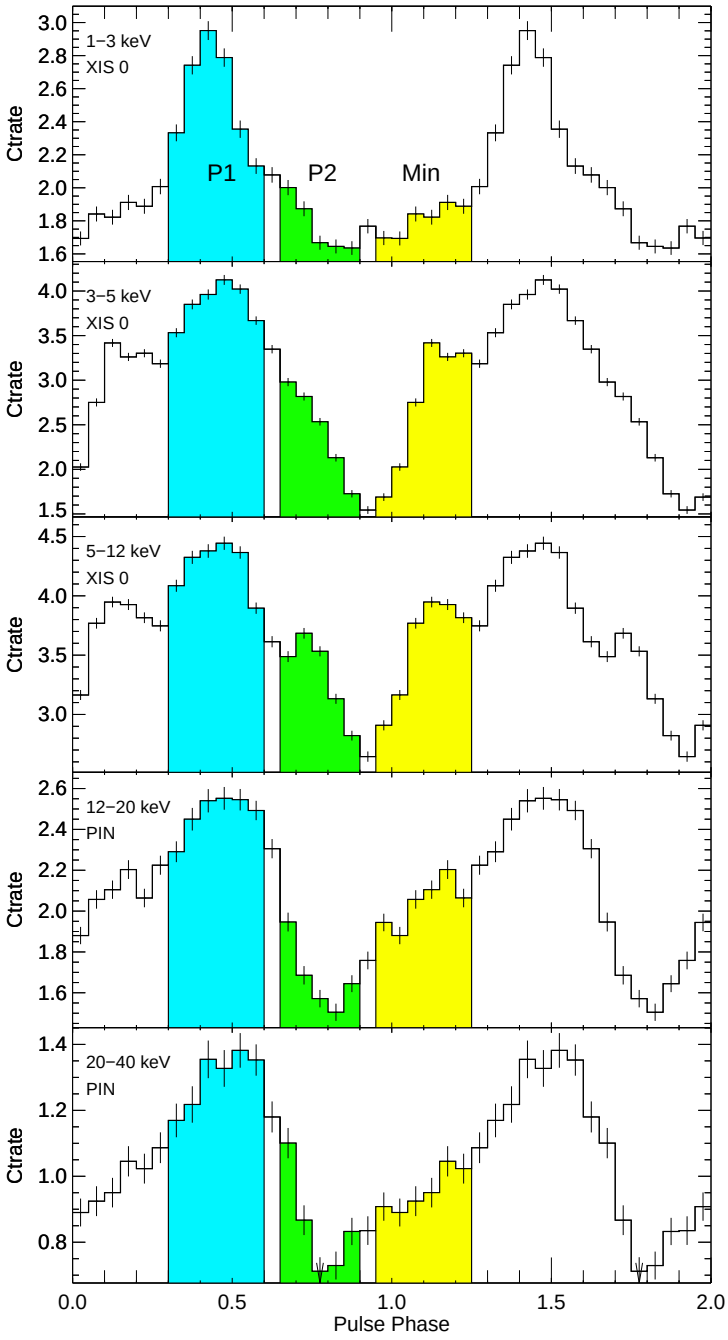

Figure 5.6 Same as Fig. 5.5 for the second observation. The highlighted regions indicate the same phase bins as in the outburst observation for a direct comparison.

P2, and $52.8^{+2.9}_{-2.0}$ keV for MIN. The CRSF width declined from $19.2^{+3.6}_{-2.7}$ keV in P1 to $11.4^{+0.3}_{-0.2}$ keV in P2, and to $9.3^{+2.5}_{-1.6}$ keV in MIN.

For the `compTT` model most parameters did not change throughout the pulse profile. The observed increase in the plasma temperature and the decrease of the optical depth $\tau_{\rm p}$ is a known systematic anti-correlation (see discussion). As with the phase averaged data, the CRSF did not show the same changes throughout the pulse profile, as in the `cutoffpl` model. The best-fit values for the CRSF centroid energy were $57.9^{+8.7}_{-4.2}$ keV for P1, $57.7^{+2.0}_{-4.1}$ keV for P2, and $51.0^{+4.9}_{-2.4}$ keV for MIN, and the widths were $13.5^{+15.5}_{-3.4}$ keV,$14.9^{+2.9}_{-3.1}$ keV, and $9.0^{+4.6}_{-2.0}$ keV for P1, P2 and MIN, respectively. Fe Kα and Fe Kβ energies were consistent with ~ 6.4 keV and ~ 7.1 keV, similar to the `cutoffpl` values.

Table 5.2. Phase resolved outburst spectral parameters. Same models as in Table 1

Parameter	Cutoffpl			Parameter	CompTT		
	Peak 1	Peak 2	Minimum		Peak 1	Peak 2	Minimum
phabs $N_{\rm H}[10^{22}/{\rm cm}^2]$	$1.35^{+0.02}_{-0.03}$	$1.38^{+0.03}_{-0.01}$	$1.21^{+0.04}_{-0.04}$		$1.28^{+0.04}_{-0.05}$	$1.22^{+0.6}_{-0.5}$	$1.20^{+0.04}_{-0.05}$
pcfabs $N_{\rm H}[10^{22}/{\rm cm}^2]$	$11.1^{+0.8}_{-0.5}$	$10.6^{+0.4}_{-0.2}$	$11.7^{+1.1}_{-1.1}$		$11.6^{+0.8}_{-0.8}$	$11.0^{+0.9}_{-1.0}$	$12.16^{+1.09}_{-0.89}$
covering fract.	$0.66^{+0.03}_{-0.03}$	$0.52^{+0.1}_{-0.02}$	$0.67^{+0.05}_{-0.05}$		$0.70^{+0.03}_{-0.04}$	$0.58^{+0.6}_{-0.7}$	$0.70^{+0.04}_{-0.05}$
blackbody kT [keV]	$0.52^{+0.03}_{-0.02}$	$0.58^{+0.01}_{-0.02}$	$0.50^{+0.02}_{-0.02}$		$0.54^{+0.03}_{-0.02}$	$0.59^{+0.03}_{-0.03}$	$0.52^{+0.03}_{-0.02}$
blackbody norm $[10^{-3}]^{\dagger}$	$7.0^{+1.0}_{-1.6}$	$2.3^{+0.6}_{-0.4}$	$8.1^{+1.7}_{-0.7}$		$12.3^{+1.7}_{-1.9}$	$8.9^{+1.6}_{-1.6}$	$10.1^{+1.6}_{-1.4}$
$E_{\rm cut}$ [keV]	$29.46^{+7.2}_{-3.2}$	$18.34^{+0.76}_{-0.4}$	$10.7^{+1.3}_{-0.9}$	compTT T_0 [keV]	$1.31^{+0.10}_{-0.07}$	$1.41^{+0.04}_{-0.05}$	$1.48^{+0.11}_{-0.07}$
Γ	$0.42^{+0.06}_{-0.04}$	$0.56^{+0.04}_{-0.02}$	$-0.13^{+0.09}_{-0.08}$	compTT kT [keV]	$7.67^{+1.39}_{-0.38}$	$11.91^{+9.06}_{-2.77}$	$6.79^{+0.75}_{-0.21}$
$A_{\rm pl}^{\dagger}$	$0.12^{+0.01}_{-0.01}$	$0.14^{+0.01}_{-0.00}$	$0.04^{+0.004}_{-0.004}$	compTT $\tau_{\rm p}$	$6.31^{+0.31}_{-0.40}$	$4.00^{+0.47}_{-0.45}$	$6.60^{+0.38}_{-0.62}$
				compTT norm †	$0.11^{+0.01}_{-0.01}$	$0.05^{+0.02}_{-0.01}$	$0.08^{+0.01}_{-0.01}$
$E_{\rm CRSF}$ [keV]	$66.6^{+0.9}_{-2.3}$	$55.5^{+0.5}_{-0.7}$	$52.8^{+2.9}_{-2.0}$		$57.9^{+8.7}_{-4.2}$	$57.7^{+2.0}_{-4.1}$	$51.0^{+4.9}_{-2.4}$
$\sigma_{\rm CRSF}$ [keV]	$19.2^{+3.6}_{-2.7}$	$11.4^{+0.3}_{-0.2}$	$9.3^{+2.5}_{-1.6}$		$13.5^{+15.5}_{-3.4}$	$14.9^{+2.9}_{-3.1}$	$9.0^{+4.6}_{-2.0}$
$\tau_{\rm CRSF}$ [keV]	$130.8^{+7.0}_{-19.6}$	$44.1^{+2.3}_{-3.3}$	$22.7^{+14.6}_{-7.3}$		$25.6^{+45.4}_{-12.3}$	$79.5^{+64.8}_{-40.2}$	$13.5^{+20.4}_{-4.7}$
$E_{\rm Fe\ K\alpha}$ [keV]	$6.41^{+0.01}_{-0.01}$	$6.41^{+0.01}_{-0.01}$	$6.42^{+0.01}_{-0.01}$		$6.41^{+0.01}_{-0.01}$	$6.41^{+0.01}_{-0.01}$	$6.42^{+0.01}_{-0.01}$
$E_{\rm Fe\ K\beta}$ [keV]	$7.16^{+0.05}_{-0.05}$	$7.08^{+0.06}_{-0.06}$	$7.09^{+014}_{-0.11}$		$7.16^{+0.04}_{-0.05}$	$7.09^{+0.06}_{-0.05}$	$7.12^{+0.14}_{-0.12}$
Eq. Width Kα/Kβ [eV]	$37^{+9}_{-6}/7^{+7}_{-7}$	$59^{+8}_{-9}/11^{+9}_{-9}$	$64^{+9}_{-9}/8^{+7}_{-8}$		$39^{+5}_{-6}/10^{+7}_{-7}$	$58^{+7}_{-4}/13^{+7}_{-8}$	$62^{+9}_{-8}/8^{+9}_{-8}$
$\rm Flux_{2-10\,keV}[10^{36}$ ergs/sec $]^{\ddagger}$	10.5	8.14	7.5				
$\rm C_{XIS1}/C_{PIN}$	0.98 / 1.1	0.97 / 1.04	0.99/1.16		1.04 / 1.23	0.99 / 1.19	1.08 / 1.23
$\chi^2_{\rm red.}$/dofs	1.17/436	1.19/423	1.11 / 527		1.20 / 438	1.16 / 423	1.26/ 430

Note. — † Units in Photons keV^{-1} cm^{-2} s^{-1}, ‡ unabsorbed flux

5.5 Discussion

I presented an analysis of the two *Suzaku* observations of the Be/X-Ray binary 1A 1118−61 during the peak of its outburst in 2009, January and ∼ 13 days later. A CRSF, detected with *RXTE* at ∼ 55 keV, could be observed in both observations, although the significance is lower in the second observation. An Fe Kβ line at 7.13 keV has been observed in addition to the strong Fe Kα line at 6.4 keV. The broad band continuum was modeled with the empirical `cutoffpl` model, including an additional 10 keV systematic component to improve the residuals. Softening of the power law index Γ between peak and decay had been observed in an earlier outburst and could be confirmed. The Comptonization model `compTT`, where the 10 keV component was not needed, has also been applied. The pulse profiles at lower energies changed from a two peaked to a single peaked profile between both observations. Phase resolved spectral analysis was performed for both observations and the same models as in the phase averaged analysis were applied.

5.5.1 Outburst behavior

The third observed outburst of 1A 1118−61 follows a pattern similar to the second outburst from 1992, i.e. a strong peak lasting ∼ 3 weeks and an elevated level of emission up to 6 weeks afterwards. The time between outbursts was in both cases ∼ 6200 days, corresponding to ∼ 17 years, indicating that this outburst could be periodic on very long time scales. The proposed orbital periods varied from ∼ 350 days (Corbet, 1986) up to ∼ 58 days (Reig et al., 1997). The most recent determination of the orbital period of 24 days was established by Staubert et al. (2010) using the delay in pulse arrival time of *RXTE* monitoring observations throughout this outburst. Using this method on the light curves showed that *Suzaku* is in full agreement with the *RXTE* results (Staubert, priv. comm). This period would put 1A 1118−61 in the wind accretor region on the "Corbet" diagram (Corbet, 1986), making it a very unique source for a Be system.

A very similar scenario was introduced by Villada et al. (1999), who monitored the $H\alpha/H\beta$ emission before and after the second outburst and proposed

that the optical companion, Hen $3-640$, has an extended large envelope where a weak interaction with the NS can occur. In this case there is no need for a high eccentricity of the orbit to provide an outburst close to the periastrion. In the scenario of Villada et al. (1999), the NS is orbiting the O star in an environment with gradually increasing density, until a steady accretion disk is created and the X-ray flux suddenly increases. The sudden increase in the accretion material would provide the torque on the NS to produce the observed changes in the pulse period. The surrounding material is then swept out in a short time and the system returns to quiescence. According to Villada et al. (1999), an interval of 17 years between the outbursts is a reasonable time scale to accumulate enough material between the outbursts.

5.5.2 Cyclotron features

In the outburst, a CRSF has been observed at $\sim 55\,\mathrm{keV}$ and the parameters are consistent with the *RXTE* data (Doroshenko et al., 2010b). For the second observation the CRSF can still be observed, although the significance is lower.

To estimate the magnetic field strength, I used the 12-B-12 method described in chapter 3, including the gravitational redshift of the neutron star. Assuming a typical neutron star mass of $1.4\,M_{\odot}$and NS radius of 10 km gives $z = 0.3$. For 1A 1118−61 the CRSF at $\sim 55\,\mathrm{keV}$ corresponds to a magnetic field of $\sim 6.4 \times 10^{12}\,\mathrm{Gauss}$, making it, together with the $\sim 50\,\mathrm{keV}$ line of A 0535+26, one of the strongest observed magnetic fields on an accreting neutron star in a binary system.

A possible feature in the residuals at $\sim 120\,\mathrm{keV}$ could indicate the existence of a first harmonic line, as observed in multiple sources, such as 4U 0115+63 (Heindl et al., 1999), 4U 1907+09 (Cusumano et al., 1998; Makishima et al., 1999) and Vela X−1 (Makishima et al., 1999; Kreykenbohm et al., 2002). Including a `gabs` line at this energy does not significantly improve the fit, though a ^{153}Gd instrumental line at $\sim 150\,\mathrm{keV}$, which is due to electron-capture (Kokubun et al., 2007), as well as possible systematic uncertainties in the background weaken the significance of the detection further.

The interpretation of the CRSF line for the second observation is more challenging. When leaving all line parameters independent in the `cutoffpl` model, the centroid energy declines to $\sim 47\,\mathrm{keV}$ in the second observation. This contradicts the behavior found in other Be-Binaries, such as V 0332+53, 4U 0115+63, and X 0331+53, where Tsygankov et al. (2006) and Nakajima et al. (2006, 2010) found a negative correlation between the CRSF centroid energy and the luminosity of the source. Staubert et al. (2007) found a positive CRSF−luminosity correlation in the low mass X-ray binary Her X−1 and an detailed explanation of the two scenarios is discussed in their paper. The type of correlation seems to depend on whether the observed luminosity is above or below the Eddington luminosity. When the luminosity is above the Eddington luminosity, the infalling protons start to interact before they are part of the accretion column and a "shock front" region, where the CRSF most likely occurs, is created. With increasing luminosity, the proton interaction occurs farther away from the NS surface, where the magnetic field is lower and therefore the observed CRSF is seen at lower energies.

Below the Eddington luminosity, the proton interaction does not occur above the accretion column but is part of it. When the luminosity increases, the accretion "pressure" increases as well and the region where the CRSF is created is pressed closer to the NS surface, where the magnetic field is higher. This results in a positive CRSF-luminosity correlation, as observed here as well as in, e.g., Her X−1. The flux levels (Tab. 1) obtained for both observations showed that the first observation is most likely above, and the second observation is definitely below the Eddington luminosity of the system, and that the potentially observed anti-correlation is expected.

Leaving the CRSF parameters free in the `compTT` model led to a different conclusion. The width became very broad $\sim 25 - 30\,\mathrm{keV}$ and the CRSF became a part of the continuum spectrum, changing the overall `compTT` parameters. In this case the centroid energy actually was very similar to the energy observed during the outburst, but I did not succeed in constraining the parameters properly for a detailed analysis. Freezing the CRSF parameters to the values obtained from the `cutoffpl` model resulted in unacceptable residuals throughout the whole

spectrum. When freezing the energy and the width of the CRSF parameters to the outburst values, the residuals became acceptable and the observed optical depth became 27.9 ± 2. As discussed above, the results of the `cutoffpl` descriptions allow for a more straight forward interpretation of the cyclotron line parameters within current ideas.

5.5.3 Continuum comparison

When comparing both observations, changes in the broad band continuum parameters were observed. During the 1974 outburst Ives et al. (1975) observed a harder spectrum in the peak compared to later observation. Looking at the `cutoffpl` model, the present outburst showed a similar behavior with a very hard spectrum (power law index $\Gamma = 0.35$) at the luminosity peak, and a much softer power law index of $\Gamma \sim 1$ in the second observation. Note also that the cutoff/folding energy increased for the observation with declining luminosity. A similar behavior has been observed in a number of different HMXB transients, such as A 0535+26 (Caballero, 2009), V 0332+53 (Mowlavi et al., 2006) and EXO 2030+375 (Reynolds et al., 1993). This is in contrast to EXO 2030+375, where the observed folding energy increases with lower luminosity. Soong et al. (1990) interpreted this parameter in phase resolved results and concluded that the folding energy reflects a change of the viewing angle on the accretion column, which allows a deeper look into the emission region and therefore directly correlates with the observed electron plasma temperature. The change observed in the phase averaged observations follows a similar reasoning, and at lower luminosities the emission region is closer to the NS, where the observed plasma temperatures are expected to be higher.

A comparison of `compTT` parameters between *Suzaku* and *RXTE* showed consistent results for the spectral parameters in the outburst (Doroshenko et al., 2010b) . In contrast to the *RXTE* results, the observed column density $N_{\rm H}$ is higher and consistent with the results obtained by the `cutoffpl` model. The main difference between these results and the *RXTE* data lies in the use of a combined Galactic and intrinsic column density and the additional need of a low

energy black body, so that these values cannot be compared directly. Note that the *RXTE*/PCA instrument used in Doroshenko et al. (2010b) did not provide usable data below 3.5 keV and therefore a partial covering, as well as a black body component were not necessary. Both, the black body temperature for the low energy excess and the photon seed temperature in the `compTT` model decreased by $\sim 1/3$ between outburst and the second observation, indicating a correlation between both parameters. A possible explanation is that the source of the `compTT` seed photons is the same as the soft excess modeled by the black body component. The observed change in the optical thickness indicates the the observed material is optically thick in the outburst and gets optically thinner for the second observation.

Although an increase in the plasma temperature of the `compTT` model was observed after the outburst, i.e., in principal consistent with the interpretation of the `cutoffpl` parameters, one has to be careful with a direct interpretation of the spectral parameter. The optical depth τ and the electron plasma temperature kT_e show a very strong negative correlation (e.g. Wilms et al., 2006), and the best-fit values cannot be used directly for interpretation. Defining the Compton y parameter:

$$y = \frac{4kT_\mathrm{e}}{m_\mathrm{e}c^2}\max(\tau, \tau^2), \tag{5.1}$$

can help in the physical interpretation. Reynolds & Nowak (2003) used the Compton y parameter in the description of accretion disk coronae around black holes. A value of $y \approx 1$ or slightly higher means that the average emitted photon energy increases by an "amplification factor", $A(y) \approx \exp(\mathrm{y})$, and is refered to as "unsaturated inverse Comptonization". For $y \gg 1$ the average photon energy reaches the thermal energy of the electrons. This case is called the "saturated inverse Comptonization". Using kT and τ_p results in $y = 2.13 \pm 0.2$ for the outburst data and $y = 1^{+9}_{-0.7}$ for the second observation. Typical calculated values of y-parameters are smaller than 1, e.g., ~ 0.5 for Cyg X−1 (Reynolds & Nowak, 2003), ~ 0.2 for 4U 2206+54 (Torrejón et al., 2004), and ~ 0.6 for XB 1832−330 (Parmar et al., 2001). Note that the second observation is very badly constrained due to the large error bars on the electron plasma temperature and the optical depth and therefore cannot be used for interpretation. The calculated y parameter for the outburst

indicates that the system is in, or very close, to a "saturated inverse Comptonization" state.

5.5.4 Fe lines

In both observations an Fe Kα and Fe Kβ emission line has been observed, where the Fe Kα− Fe Kβ normalization ratio of 12% is consistent with neutral material. The Fe Kα EQWs were 51 ± 4 eV and 46 ± 10 eV for the first and second observation, respectively, while at the same time the $5 - 7$ keV power law flux dropped from $6.50 \pm 0.01 \times 10^{-10}$ ergs cm^{-2} s^{-1} to $1.23 \pm 0.01 \pm \times 10^{-10}$ ergs cm^{-2} s^{-1}. The relative constant EQWs imply that the Fe line emitting region is relatively close to the source of ionizing flux, so that the observed Fe line intensity adapts quickly to the changing incident flux. The Fe line normalization was $1.79 \pm 0.06 \times 10^{-3}$ photons cm^{-2} s^{-1} and $3.15 \pm 0.3 \times 10^{-4}$ photons cm^{-2} s^{-1} for the respective observations. The ratios between Fe normalization and power law flux were consistent in both observations, 2.75 ± 0.10 and $2.56 \pm 0.27 \times 10^6$ photons/ergs, reflecting the two calculated EQWs. Using the continuum flux difference and the time between observations, the calculated change in power law flux was $\sim 0.415 \pm 0.001 \times 10^{-10}$ ergs cm^{-2} s^{-1} per day in the 12.7 day period between the observations. A linear decrease could be assumed using the BAT data of Fig. 5.1. For the second observation, the Fe normalization was manually increased in XSPEC until the resulting EQW matched the upper limit of the measured EQW. This value corresponds to an Fe normalization of $\sim 3.9 \times 10^{-4}$ photons cm^{-2} s^{-1}, assuming the measured continuum given above for the second observation. Together with the previously calculated constant of 2.56×10^6, a matching power law flux of ~ 1.52 could be calculated. Using this flux difference, together with the rate of change in the $5 - 7$ keV energy range, one can then determine a maximum time delay which would still preserve the observed EQW within errors. The calculated upper limit to the delay between the Fe and X-ray emission region is ~ 0.7 days. Note that these eestimates are very crude and uncertainties from the orbital motion or from line of sight assumptions are not taken into account here.

Table 5.3 Pulse fractions for 1A 1118−61

Energy [keV]	Outburst	2nd Obs
$1-3$	1.05	1.24
$3-5$	1.08	1.40
$5-12$	1.25	1.20
$12-20$	1.70	1.34
$20-40$	1.85	1.30

5.5.5 Phase resolved description

1A 1118−61 shows a similar energy and luminosity pulse profile dependency as many other sources, e.g. 4U 0115+63 (Tsygankov et al., 2007), V 0332+53 (Tsygankov et al., 2006) and A 0535+26 (Caballero, 2009). In the outburst observation, the observed broad double peaked structure at lower energies changed to a single peak profile above 10 keV, where the main peak (P1) broadened slightly with increased energy and the secondary peak (P2) weakened. For the second observation, the pulse profile changed significantly. There was still a dominant primary peak at P1, although it is narrower in the lowest energy band. The secondary peak is only marginally indicated between $5-12$ keV (see Fig. 5.6) and absent in the other energy bands. On the other hand, between $3-12$ keV a small peak or extended shoulder could be observed preceding the primary peak.

To confirm the disappearance of the second peak, pulse fractions of the total counts of the P1/P2 regions were calculated for the indicated energy bands. The pulse fraction was defined as ($\mathrm{P1_{countrate}}-\mathrm{P2_{countrate}}$) / $\mathrm{P2_{countrate}}$ where the P1 and P2 regions are indicated in Fig. 5.5 and 5.6. Table 5.3 shows that the pulse fraction increases towards higher energies in the outburst data, typical for a weakening of the second pulse. In the second observation the values do not vary for the different energy bands, and the small peak in the $5-12$ keV band shows only a marginal smaller pulse fraction than in the other energy bands.

Tsygankov et al. (2007) described similar profiles and proposed that a misalignment of the rotational and magnetic axes of the neutron star leads to the case where one accretion column is observed whole, whereas the second accretion column is partially screened by the NS surface so that only the softer photons, which

are created in the higher regions of the accretion column, are observed. When the overall luminosity, and therefore accretion rate, decreases, the column height decreases and even the soft photons from the second pole are shielded. This behavior is in contrast to the variation observed in the cyclotron line production region, where the line forming region is closer to the NS surface at higher luminosities.

For a more physical picture gravitational effects, such as light bending, have to be taken into account when discussing pulse profiles (Meszaros & Nagel, 1985a; Kraus et al., 2003). For a canonical NS with a mass of $1.4 M_{\odot}$ and a radius of 10 km the visible surface of a NS is 83%. With this increased surface visibility the pulsed flux from both hot spots is visible over a longer part of the pulse phase, and parts of the accretion column of the second peak are still visible, although that hot spot is on the far side of the NS. With decreasing luminosity, the hot spot size decreases and the visible fraction of the second accretion column is not observed anymore.

Pulse profile deconvolution methods have been developed by Kraus et al. (2003) and Sasaki et al. (2010), among others, and have been applied to multiple sources, e.g. EXO 2030+375 (Sasaki et al., 2010) and A 0535+26 (Caballero, 2009). With this method it will be possible to establish a better picture of the system and it would allow determination of the positions of the hot spots with respect to the rotation axis. However, at this moment these deconvolution methods are rather difficult to constrain due to the large number of free parameters, such as accretion geometry, magnetic field alignment or equation of state of the accreting material and the application on this data will be left for future work.

This chapter is a reprint of the published publication: Suchy, Slawomir; Pottschmidt, Katja; Rothschild, Richard E.; Wilms, Jrn; Frst, Felix; Barragan, Laura; Caballero, Isabel; Grinberg, Victoria; Kreykenbohm, Ingo; Doroshenko, Victor; Santangelo, Andrea; Staubert, Rdiger; Terada, Yukikatsu; Iwakari, Wataru; Makishima, Kazuo, "Suzaku Observations of the HMXB 1A 1118-61", The Astrophysical Journal, 2011, Vol. 733, 15

Chapter 6

GX301-2

6.1 Introduction

The High Mass X-ray Binary (HMXB) system GX 301−2 was discovered in 1969 April during a balloon experiment (Lewin et al., 1971; McClintock et al., 1971). The system consists of an accreting neutron star (NS) fed by the surrounding stellar wind of the B type emission line companion Wray 977 (Jones et al., 1974). A recent luminosity estimate derived from atmospheric models puts its distance at ~ 3 kpc (Kaper et al., 2006), the value utilized in this paper. The orbital period was established to be ~ 41 days (White et al., 1978a) using *Ariel* 5 observations and was refined with the *Burst And Transient Source Experiment (BATSE)* to ~ 41.5 days with an eccentricity of ~ 0.46 (Koh et al., 1997). Doroshenko et al. (2010a) discussed a possible orbital evolution and determined an orbital period of 41.482 ± 0.001 d, assuming no change in orbital period. Kaper et al. (2006) determined that the mass of the companion was in the range $39\,M_{\odot} < M < 53\,M_{\odot}$ and the radius of Wray 977 was R_{*} $\sim$62 $R_{\odot}$, obtained by fitting atmosphere models.

The X-ray flux is highly variable throughout an individual binary orbit but follows a distinct pattern when averaged over multiple orbits (see Figure 6.1). Shortly before the periastron passage, the X-ray luminosity increases drastically in the energy band above ~ 5 keV, as seen in *Rossi X-ray Timing Explorer (RXTE)*/ All Sky Monitor (ASM) data (Leahy, 2002). The NS passes closest to the companion at a distance of $\sim 0.1R_{*}$ (Pravdo et al., 1995). Shortly after the periastron

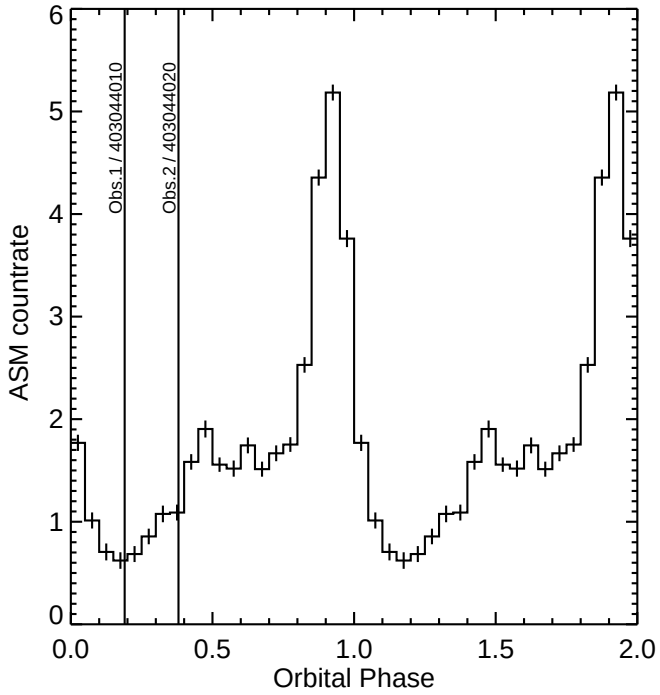

Figure 6.1 *RXTE*/ASM 1.5−12 keV light curve folded with the orbital period of 41.48 days. The two lines indicate the times of the orbital phase when the *Suzaku* observations were performed. The profile shows the strong flux increase during the pre-periastrion flare at orbital phase ~ 0.9. For clarity, two binary orbits are shown.

passage, $\phi_{\rm orb} \sim 0.2$, the X-ray luminosity dips for a short period of time. Leahy (2002) demonstrated that neither a simple spherical wind model nor a circumstellar disk model around Wray 977 are sufficient to describe the observed variations in the folded *RXTE*/ASM data. An additional stream component is able to account for the sudden increase in X-ray luminosity, as the NS passes through the stream shortly before periastron and accretes more material. This model also explains a slightly higher X-ray luminosity around $\phi_{\rm orb} \sim 0.5$, when the NS passes through the accretion stream a second time.

Pulsations with a period of ~ 700 s were discovered in the *Ariel-5* observations (White et al., 1976), making GX 301−2 one of the slowest known pulsars. The pulse period has varied drastically throughout the last ~ 20 years (Pravdo & Ghosh, 2001; Evangelista et al., 2010). Prior to 1984, the pulse period stayed

relatively constant at 695 s−700 s and then spun up between 1985 and 1990 to $\sim$ 675 s. From 1993 until the beginning of 2008, the change in the spin reversed again, showing a decline. *Fermi*/Galactic Burst Monitor (GBM) data[1] have revealed that GX 301−2 experienced another spin reversal and briefly spun-up with the pulse period decreasing from $\sim$ 687 s to $\sim$ 681 s between May 2008 and October 2010. Since October 2010, the pulse period has shown only small variations around $\sim$ 681 s.

Most recently, Göğüş et al. (2011) discovered a peculiar 1 ks dip in the luminosity of GX 301−2, where the pulsations disappeared for one spin cycle during the dip. Several such dips have been previously observed in Vela X-1 (Kreykenbohm et al., 1999, 2008), where it is assumed that the accretion on the NS was interrupted for a short period of time.

The pulse phase average spectrum of GX 301−2 is described using a power law with a high energy cutoff. The continuum does not show a strong variation in the intrinsic parameters (Γ, $E_{\rm cut}$, and $E_{\rm fold}$) throughout the orbit (Mukherjee & Paul, 2004), as seen in two data sets from *RXTE*, taken in 1996 and 2000, sampling most phases of the binary orbit. One of the major characteristics of the X-ray spectrum of GX 301−2 is the high and strongly variable column density of its line-of-sight absorber throughout the orbit, indicative of a clumpy stellar wind ($N_{\rm H} = 10^{22} - 10^{24}$ cm^{-2}). In addition to the high column density, a very bright Fe Kα emission line can be observed. This line has shown a strong correlation with the observed luminosity, indicating that the line is produced by local clumpy matter surrounding the neutron star (Mukherjee & Paul, 2004). Kreykenbohm et al. (2004) used the *RXTE* data set from 2000 to perform phase resolved spectroscopy and showed that an absorbed and partially covered pulsar continuum (power law with Fermi-Dirac cutoff) as well as a reflected and absorbed pulsar continuum were consistent with the data.

A cyclotron resonance scattering feature (CRSF) at $\sim$ 35 keV was first discovered with *Ginga* (Mihara, 1995). Orlandini et al. (2000) found systematic deviations from a power law continuum at $\sim$ 20 and $\sim$ 40 keV in *BeppoSAX*,

[1] http://www.batse.msfc.nasa.gov/gbm/science/

where the former could not be confirmed as a CRSF due to the proximity of the continuum cutoff. Kreykenbohm et al. (2004) excluded the existence of a CRSF at $\sim 20\,\mathrm{keV}$ and showed that the CRSF centroid energy varies between 30–38 keV over the pulse rotation of the NS. Furthermore, they showed that the CRSF centroid energy and width are correlated.

6.2 Observation and Data Reduction

Suzaku observed GX 301−2 on 2008 August 25 with an exposure time of $\sim 10\,\mathrm{ks}$ (ObsID 403044010; hereafter Obs. 1). The observation was cut short by a set of target of opportunity observations and was continued on 2009 January 5, acquiring an additional $\sim 60\,\mathrm{ks}$ exposure time (ObsID 403044020; Obs. 2). Both main instruments, the X-ray Imaging Spectrometer (XIS; Mitsuda et al., 2007) and the Hard X-ray Detector (HXD; Takahashi et al., 2007) were used in these observations. A detailed description of the instruments is provided in chapter 2. The two observations correspond to orbital phases of 0.19 (Obs. 1) and 0.38 (Obs. 2), where Obs. 1 falls into the lowest flux part of the binary orbit (see Figure 6.1). The $2-10\,\mathrm{keV}$ absorbed flux was $1.6\times10^{-10}\,\mathrm{erg\,cm^{-2}\,s^{-1}}$ for Obs. 1 and $\sim 8\times10^{-10}\,\mathrm{erg\,cm^{-2}\,s^{-1}}$ for Obs. 2 (see Table 1 for details). Both observations were performed using the HXD nominal pointing to enhance the sensitivity of the HXD detectors.

To minimize possible pile-up, the XIS instruments were operated with the 1/4 window option with a readout time of 2 s. Data were taken in both 3×3 and 5×5 editing modes, which were extracted individually with the *Suzaku* FTOOLS version 16 as part of HEASOFT 6.9. The unfiltered XIS data were reprocessed with the most recent calibration files available and then screened with the standard selection criteria as described by the *Suzaku* ABC guide[2]. The response matrices (RMFs) and effective areas (ARFs) were weighted according to the exposure times of the different editing modes. The XIS data were then grouped with the number of channels per energy bin corresponding to the half width half maximum of the

[2]http://heasarc.gsfc.nasa.gov/docs/suzaku/analysis/abc/

spectral resolution, i.e. grouped by 8, 12, 14, 16, 18, 20, and 22 channels starting at 0.5, 1, 2, 3, 4, 5, 6, and 7 keV, respectively (M. A. Nowak, 2010, private communication). The XIS spectral data were used in the energy range of $2 - 10$ keV for reasons described below.

The PIN data were grouped by a factor of 5 below and by a factor of 10 above 50 keV for Obs. 1. In Obs. 2 the channels were grouped by 3 throughout the whole energy range. GSO data were extracted and binned following the *Suzaku* ABC guide. The PIN data energy range of 15–60 keV and the GSO data energy range of $50 - 90$ keV were used for the phase averaged analysis. Due to the short exposure times, no GSO data were extracted in Obs. 1 and in the phase resolved analysis of Obs. 2.

6.2.1 XIS Responses

GX 301−2 is a source with very large and highly variable photoelectric absorption in the line of sight as well as a very strong Fe Kα emission line. For spectral modeling, the calculated responses of the XIS detectors showed a 'leakage' emission level (Matsumoto et al., 2006), which stemmed from the instrument characteristics. That is, a small fraction of an event charge cloud is registered at energies below the peak energy, creating a 'low energy tail' in the spectrum. This 'tail' is about three orders of magnitude weaker than the intensity of the peak count rate of the measured photon. The response to the Fe line is therefore described as a Gaussian plus a constant at lower energies, approximately three orders of magnitude below the peak value and extending to below 1 keV. Due to the strong Fe Kα line and the very strong absorption in this source, the constant level response of the Fe line extends above the measured flux below 2 keV. This results in significant residuals below ~ 2 keV, which seem to be stronger for the BI spectrum then for that of the FI CCD. Figure 6.2 shows the phase averaged spectrum from the second observation of GX 301−2 and the best fit models using the HEASOFT generated XIS responses.

Together with the *Suzaku* Guest Observer Facility (GOF), which provided an experimental response parameter file where the 'low energy tail' is ignored, we

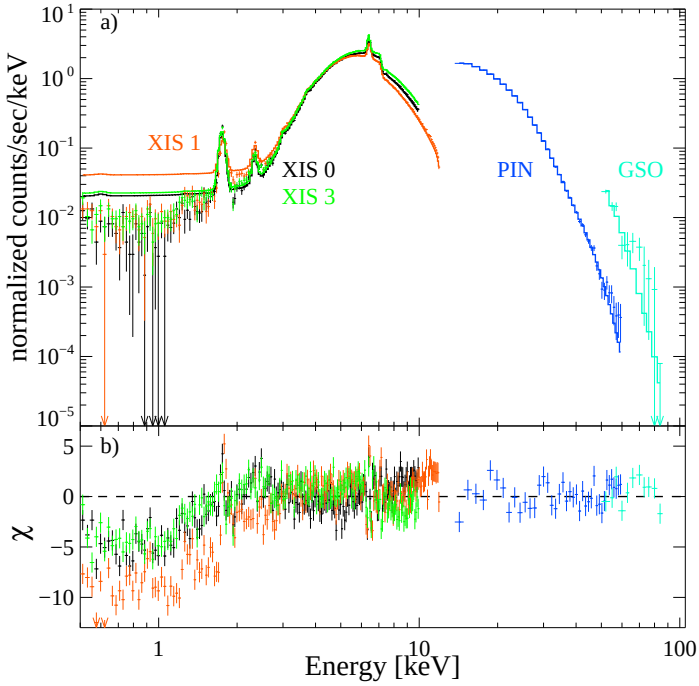

Figure 6.2 (a) Best fit models of the *Suzaku* GX 301−2 second observation for the 3 individual XIS instruments, and the two HXD instruments. At lower energies, one clearly sees the constant level in the modeled flux discussed in the text. (b) shows that the residuals below ~ 2 keV are very pronounced.

studied this behavior in more detail. This new response for all three instruments was applied to the individual XIS spectra. Due to the fact that the new response completely excluded the missing 'tail', I now observed an excess of the data with respect to the model below $\sim$ 2 keV. The introduction of additional power law and/or black body components could improve the fits at lower energies. Due to the fact that the true level of the tail is not known, these additional components cannot be interpreted physically, and we decided to use the original response matrix and confine the selected XIS energy range to above 2 keV.

6.3 Phase averaged spectrum

6.3.1 Spectral modeling

Phase averaged broad band spectra in the 2–60 keV (Obs. 1) and 2–90 keV (Obs. 2) energy ranges were obtained. From the technical description of the XIS instruments[3], it is known that small discrepancies, e.g., in fitted power law slope, have been observed between FI and BI XIS instruments. A difference of ~ 0.05 in the power law index has been observed in calibration data and was also observed here. When modeling the FI and BI instruments with a common power law index, the residuals of the BI instrument show a systematic deviation. However, only the FI or BI instruments could be modeled together with the HXD instruments. Due to this fact and the higher sensitivity of the FI XIS instruments above 2 keV, we concentrated our discussion on the results obtained with the two FI instruments. Each data set, FI and BI, was modeled individually with the HXD data to compare the differences in the continuum. We found that when using the FI and BI instruments individually with the HXD instruments, in both observations the best fit spectral values are consistent with each other within error bars, indicating that the usage of the HXD reduced the observed discrepancies in the power law parameters.

The continuum model for pulsars can so far only be modeled with empirical models, consisting of a `powerlaw` with a cutoff at higher energies, which is typical for this kind of source (Coburn, 2001). The three empirical models described in chapter 3 are widely used: the simple high energy cutoff (`highecut`) and the Fermi-Dirac cutoff (`fdcut`, Tanaka, 1986) both are used in combination with a simple power law component. The negative-positive exponential powerlaw model `NPEX` (Mihara, 1995) is a slightly more complicated model including the power law component. For the data analyzed in this work, the best results have been obtained with the `fdcut` model. For the Obs. 1 and Obs. 2 FI data sets the best fit χ's were 260 and 542 with 245 and 267 degrees of freedom (dof), respectively (see Figure 6.3 and 6.4). Replacing the smoother Fermi-Dirac cutoff with the `highecut` model in

[3] http://heasarc.nasa.gov/docs/suzaku/prop_tools/suzaku_td/

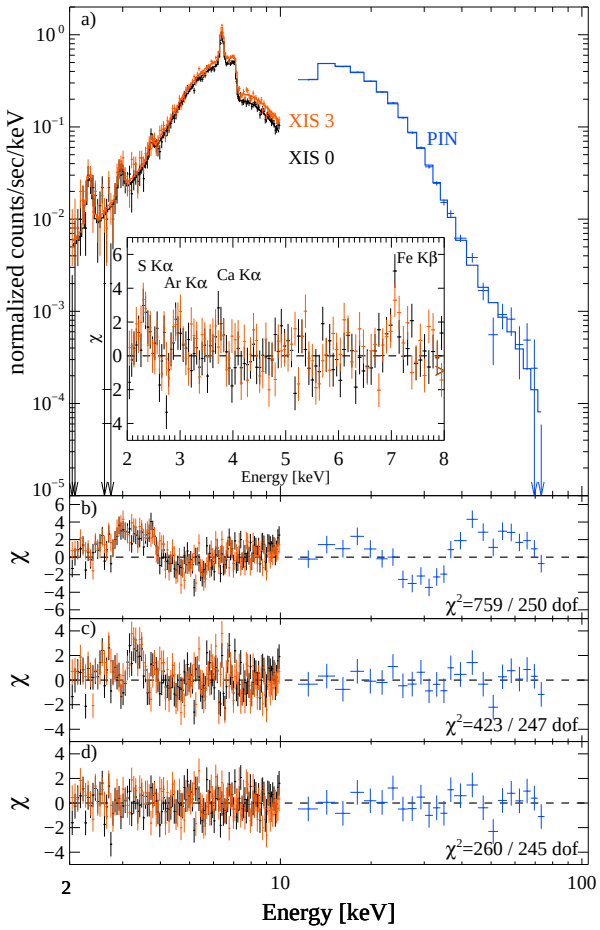

Figure 6.3 Data and best fit model for Obs. 1. a) shows the data and the best fit model. The inset shows the residual for the different emission lines observed in XIS data, where the Fe Kα line is already included in the model. b) shows the best fit residuals without partial covering and the CRSF. c) has only the CRSF added, and d) has both componenst included.

Obs. 2, resulted in slightly worse residuals ($\Delta\chi^2 \approx 15$) compared to the best fit results of the FD-cutoff model (Figure 6.3 d) and an emission line-like residual at ~ 35 keV, which is most likely due to the sharp break of the power law at the cutoff energy in this model. In comparison, the NPEX model shows even worse residuals ($\Delta\chi^2 \approx 200$) and only results in reasonable fits when the exponential curvature at higher energies is independent in the partially and fully covered components.

The best fit cutoff energy is very close to that of the observed CRSF feature (see below) and these two parameters are rather strongly correlated (see Figure 6.5). To avoid a degeneracy of the CRSF values due to a changing cutoff

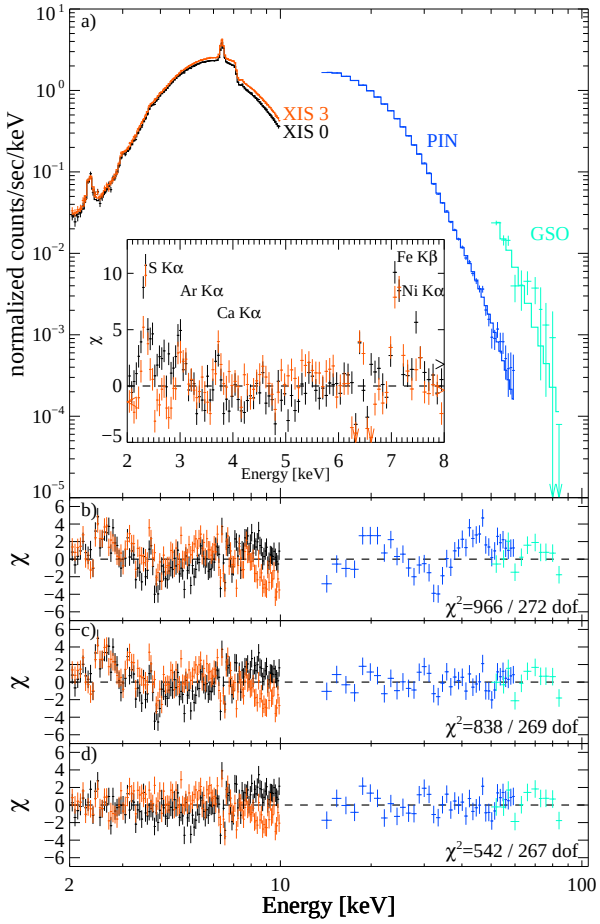

Figure 6.4 Same as Figure 6.3 for Obs. 2. In this case b) shows the residuals without partial covering and the CRSF, c) has only the CRSF added and d) has both components included.

energy, $E_{\rm cut}$ was frozen in all the fits to the best fit value from the Obs. 2 FI spectrum (29.2 keV).

Previous observations of GX 301−2 indicated the existence of clumps in the stellar wind (Kreykenbohm et al., 2004; Mukherjee & Paul, 2004), which were modeled using partial covering absorption in addition to fully covered photoelectric absorption of the smooth stellar wind. In the present analysis, the low energy portion of the spectrum also required a partial covering component (Figure 6.3b and 6.4b), which was modeled using the `TBnew` model (Wilms et al., 2011, in prep.)[4], an updated version of the existing `TBabs` model (Wilms et al., 2000). In

[4]http://pulsar.sternwarte.uni-erlangen.de/wilms/research/tbabs/

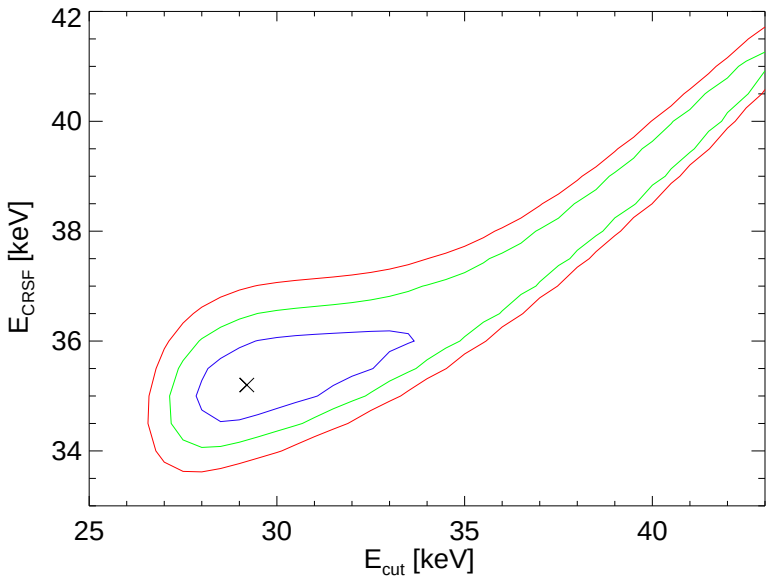

Figure 6.5 Contour plots of E_{CRSF} vs E_{cut}. The different contours indicate the 1, 2, and 3 sigma contours for the FI spectrum of Obs. 2. The X indicates the best fit values for both parameters: $E_{\mathrm{cut}} = 29.2\,\mathrm{keV}$ and $E_{\mathrm{CRSF}} = 35.2\,\mathrm{keV}$.

addition, a non-relativistic, optically-thin Compton scattering component `cabs` was included, as is necessary for column densities $N_{\mathrm{H}} > 5 \times 10^{22}$ cm^{-2}, where the plasma becomes Compton thick and part of the emission is scattered out of the line of sight. The N_{H} values from `TBabs` and from the `cabs` component were set equal and treated as one model component for the smooth stellar wind ($N_{\mathrm{H,1}}$ = `TBabs1*cabs1`) and a second component for the clumpy partial coverer ($N_{\mathrm{H,2}}$ = `TBabs2*cabs2`). The $N_{\mathrm{H,1}}$ and $N_{\mathrm{H,2}}$ column densities were left independent of each other. For spectral fitting the abundances of Wilms et al. (2000) and the cross-sections (Verner et al., 1996) were used in all data sets.

Both observations show residuals to the continuum in the $35 - 40\,\mathrm{keV}$ energy range, which we interpret as the previously observed CRSF (Mihara, 1995; Kreykenbohm et al., 2004). Modeling these residuals with an absorption line with a Gaussian optical depth (`gabs`) improved the residuals significantly in both observations (see Figures 6.3 and 6.4). The best fit values of $E_{\mathrm{CRSF}} = 42.5^{+3.2}_{-6.0}\,\mathrm{keV}$ and $35.2^{+1.4}_{-0.9}\,\mathrm{keV}$ for Obs. 1 and Obs. 2, respectively, are consistent within 90% confidence intervals. The widths of the CRSFs, $\sigma_{\mathrm{CRSF}} = 9.5^{+1.6}_{-2.8}\,\mathrm{keV}$ (Obs. 1) and $7.8^{+1.1}_{-0.9}\,\mathrm{keV}$ (Obs. 2), are also consistent within errors. An increase of σ_{CRSF} with

higher centroid energy, as previously observed in *RXTE* data (Kreykenbohm et al., 2004), could not be detected, although the best fit values hint at such a behavior. Table 6.1 shows the best fit values for the continuum with a `gabs` CRSF line where the given errors are 90% confidence values. To calculate the significance of the CRSF in the first and weaker observation, the null hypothesis approach was applied, where 10,000 spectra were created with Monte Carlo simulations using the best fit parameters without the CRSF. Gaussian uncertainties were used for the individual model parameters. Each model was fitted with and without the CRSF line to compare how much an inclusion of the line actually improves the fit. In $\sim 99.6\%$ of all fits, no CRSF feature was observed with a larger optical depth than the observed lower limits of $\tau = 10.3$, making the existence of the feature significant with $\sigma \sim 3$. Including the CRSF in the real data, the best fit improved by a $\Delta\chi^2 = 100$. A similar improvement of χ^2 was only observed in $\sim 0.1\%$ ($\sigma \sim 3.3$) of the simulated spectra, concluding that the observed line in the first observation is indeed real. For the second observation, the line was even more pronounced, where the exclusion of the CRSF increased the χ^2 by ~ 200.

Table 6.1. PHASE AVERAGED CONTINUUM PARAMETERS WITH THE GABS MODEL COMPONENT FOR BEST FIT SPECTRUM

Parameter	403044010 [10 ks]		403044020 [60 ks]	
	FI	BI	FI	BI
$N_{\rm H,1}[10^{22}$ cm$^{-2}]$	$16.6^{+3.5}_{-3.3}$	16.6 (frozen)	$20.9^{+3.5}_{-3.3}$	20.9 (frozen)
Abund Ca	1.55 (frozen)	1.55 (frozen)	$1.55^{+0.39}_{-0.18}$	$1.98^{+0.41}_{-0.49}$
Abund Fe	1.17 (frozen)	1.17 (frozen)	$1.17^{+0.04}_{-0.03}$	$1.04^{+0.03}_{-0.04}$
$N_{\rm H,2}[10^{22}$ cm$^{-2}]$	$76.9^{+3.9}_{-3.1}$	76.9 (frozen)	$28.4^{+1.0}_{-1.0}$	28.4 (frozen)
Γ	$0.83^{+0.08}_{-0.06}$	$0.82^{+0.09}_{-0.08}$	$0.96^{+0.06}_{-0.04}$	$0.98^{+0.03}_{-0.03}$
$A_{\rm PL,1}$ $[10^{-3}]^1$ fully covered	$1.68^{+0.67}_{-0.50}$	$1.38^{+0.20}_{-0.20}$	$1.1^{+1.1}_{-0.5}$	$4.70^{+0.91}_{-0.79}$
$A_{\rm PL,2}$ $[10^{-3}]^1$ part. covered	$92.5^{+16.1}_{-10.0}$	$90.0^{+16.2}_{-8.1}$	$215.5^{+25.1}_{-8.9}$	$266.4^{+17.9}_{-15.5}$
$E_{\rm cut}$ [keV]	29.2 (frozen)	29.2 (frozen)	$29.2^{+13.5}_{-2.1}$	29.2 (frozen)
$E_{\rm fold}$ [keV]	$10.3^{+3.1}_{-3.0}$	$8.3^{+2.0}_{-1.4}$	$5.7^{+0.4}_{-2.5}$	$5.6^{+0.2}_{-0.2}$
$E_{\rm CRSF}$ [keV]	$42.5^{+3.2}_{-6.0}$	$39.7^{+3.7}_{-3.9}$	$35.2^{+1.4}_{-0.9}$	$34.9^{+0.9}_{-0.5}$
$\sigma_{\rm CRSF}$ [keV]	$9.5^{+1.6}_{-2.8}$	$8.6^{+2.0}_{-2.1}$	$7.8^{+1.1}_{-0.9}$	$7.4^{+0.5}_{-0.5}$
$\tau_{\rm CRSF}$	$29.3^{+17.7}_{-19.0}$	$18.9^{+14.8}_{-9.7}$	$12.0^{+37.7}_{-4.5}$	$10.6^{+1.8}_{-1.4}$
$\rm Flux^4_{2-10\,keV}$ absorb.	$1.61^{+0.04}_{-0.15}$	$1.63^{+0.03}_{-0.07}$	$7.98^{+0.00}_{-1.42}$	$9.04^{+0.04}_{-0.06}$
$\rm Flux^4_{2-10\,keV}$ unabsorb.	$16.3^{+2.0}_{-1.1}$	$16.0^{+0.8}_{-0.7}$	$31.8^{+1.3}_{-0.2}$	$35.9^{+1.0}_{-0.4}$
$C_{\rm XIS3}/C_{\rm PIN}/C^5_{\rm GSO}$	$0.93^{+0.02}_{-0.02}/1.18^{+0.04}_{-0.04}$ / –	–/ $1.12^{+0.07}_{-0.06}$ / –	$0.951^{+0.003}_{-0.003}/1.31^{+0.02}_{-0.02}/1.39^{+0.12}_{-0.12}$	– / $1.17^{+0.02}_{-0.02}/1.27^{+0.11}_{-0.11}$
χ^2/dof	260 / 245	145 / 130	542 / 267	328 / 150

Note. — (1)Units are ph keV^{-1} cm^{-2} s^{-1}, (2) Units are ph cm^{-2} s^{-1}, (3) Values of EQWs are determined relative to the abs. continuum, Absorbed and unabsorbed flux units are [10^{-10} erg sec^{-1} cm^{-2}], (5) Values of C are with respect to XIS 0 for the FI fits and XIS 1 for the BI fits.

The CRSF can alternatively be described with the Lorenzian shaped `cyclabs` XSPEC model (Mihara et al., 1990). `Cyclabs` is described by the centroid energy $E_{\rm CRSF}$, the width $\sigma_{\rm CRSF}$, and the resonance depth $\tau_{\rm CRSF}$, similar to the `gabs` parameters. The best fit continuum parameters are consistent with the best fit values determined with the `gabs` component. The `cutoff` energy with a best fit value of $E_{\rm cut} = 31.2^{+5.1}_{-2.9}$ keV is consistent with the value obtained with the `gabs` model. The observed centroid energies of $E_{\rm CRSF} = 35.0^{+3.0}_{-2.3}$ keV and $31.6^{+1.0}_{-0.5}$ keV are of the order of $10 - 20\%$ lower than the energies obtained with the `gabs` model. This discrepancy stems from a different calculation of the line centroid energy and is described in detail in Nakajima et al. (2010). The width $\sigma_{\rm CRSF} = 11.2^{+3.8}_{-3.0}$ keV and $12.3^{+1.7}_{-1.3}$ keV for Obs. 1 and Obs. 2, respectively, is bigger than with the `gabs` model. The χ^2 / dof values of 260 / 245 and 548 / 267 for the two observations using the `cyclabs` model and thus were not a better fit when compared to the `gabs` model. For the final discussion I use the values determined by the `gabs` model.

Several emission features were observed in the residuals of the fits in both observations and were subsequentially modeled with Gaussian emission lines (see Figures 6.3 and 6.4, inlay). The width of each line was set equal to that of the Fe Kα emission line, while the intensities were left to vary independently. Energies were loosely constrained around the expected values of neutral material to avoid runaway of the line energies.

A constant (`const`) was applied, taking small instrumental differences in the overall flux normalization into account. The constant was fixed at 1 for XIS 0 and was left free for the other instruments. $C_{\rm XIS3}$, $C_{\rm PIN}$ and $C_{\rm GSO}$ in Table 1 are the cross calibration constants with respect to XIS 0 for FI fits and with respect to XIS 1 for the BI fits.

The final model had the form: `const`*$N_{\rm H,1}$ (`PL1`+ $N_{\rm H,2}$*`PL2`)* `fdcut`*`gabs`+ 6×`Gaussians`, where the power law indices of `PL1` and `PL2` are set to be equal to each other. The individual power law normalizations were independent and were used to calculate the fraction of the partial covering.

Table 6.1 and 6.2 summarize the best fit values for both observations and for the individual FI / BI data sets. For the interpretation we will concentrate on

Table 6.2. Best fit line parameters for the phase averaged spectra of GX 301−2

Parameter	403044010 [10 ks]		403044020 [60 ks]	
	FI	BI	FI	BI
$E_{\rm S\ K\alpha}$ [keV]	$2.33^{+0.01}_{-0.02}$	$2.31^{+0.03}_{-0.03}$	$2.33^{+0.01}_{-0.01}$	$2.34^{+0.01}_{-0.01}$
$I_{\rm S\ K\alpha}[10^{-5}]^2$	$2.34^{+0.61}_{-0.64}$	$2.44^{+0.96}_{-0.89}$	$5.36^{+0.50}_{-0.50}$	$4.24^{+0.68}_{-0.67}$
$\rm EQW^3_{S\ K\alpha}$ [eV]	860^{+1534}_{-585}	1109^{+1313}_{-947}	671^{+491}_{-172}	965^{+612}_{-445}
$E_{\rm Ar\ K\alpha}$ [keV]	$2.96^{+0.03}_{-0.03}$	$3.02^{+0.06}_{-0.05}$	$3.00^{+0.01}_{-0.02}$	$3.04^{+0.02}_{-0.02}$
$I_{\rm Ar\ K\alpha}[10^{-5}]^2$	$1.72^{+0.62}_{-0.69}$	$1.00^{+0.94}_{-0.48}$	$2.74^{+0.55}_{-0.54}$	$4.53^{+0.94}_{-0.88}$
$\rm EQW^3_{Ar\ K\alpha}$ [eV]	179^{+502}_{-164}	110^{+308}_{-110}	38^{+29}_{-21}	64^{+38}_{-37}
$E_{\rm Ca\ K\alpha}$ [keV]	$3.73^{+0.05}_{-0.04}$	$3.76^{+0.07}_{-0.06}$	$3.70^{+0.02}_{-0.01}$	$3.71^{+0.03}_{-0.03}$
$I_{\rm Ca\ K\alpha}[10^{-5}]^2$	$1.71^{+0.77}_{-0.83}$	$2.45^{+1.33}_{-1.35}$	$4.72^{+0.95}_{-0.99}$	$4.95^{+1.68}_{-1.71}$
$\rm EQW^3_{Ca\ K\alpha}$ [eV]	69^{+140}_{-69}	100^{+154}_{-100}	14^{+10}_{-8}	14^{+14}_{-14}
$E_{\rm Fe\ K\alpha}$ [keV]	$6.399^{+0.007}_{-0.006}$	$6.410^{+0.010}_{-0.010}$	$6.409^{+0.003}_{-0.001}$	$6.424^{+0.003}_{-0.002}$
$\sigma_{\rm Fe\ K\alpha}$ [eV]	13^{+22}_{-2}	< 31	< 5	< 7
$I_{\rm Fe\ K\alpha}[10^{-4}]^2$	$7.16^{+0.36}_{-0.22}$	$6.96^{+0.63}_{-0.63}$	$19.20^{+0.29}_{-0.30}$	$22.9^{+0.61}_{-0.58}$
$\rm EQW^3_{Fe\ K\alpha}$ [eV]	241^{+53}_{-35}	230^{+58}_{-52}	133^{+27}_{-4}	142^{+10}_{-10}
$E_{\rm Fe\ K\beta}$ [keV]	$7.06^{+0.03}_{-0.03}$	$7.04^{+0.04}_{-0.04}$	$7.09^{+0.01}_{-0.01}$	$7.09^{+0.02}_{-0.02}$
$I_{\rm Fe\ K\beta}[10^{-4}]^2$	$1.19^{+0.29}_{-0.35}$	$1.54^{+0.59}_{-0.60}$	$2.65^{+0.27}_{-0.25}$	$4.50^{+0.53}_{-0.56}$
$\rm EQW^3_{Fe\ K\beta}$ [eV]	43^{+33}_{-29}	56^{+53}_{-51}	21^{+7}_{-5}	32^{+9}_{-10}
$E_{\rm Ni\ K\alpha}$ [keV]	–	–	$7.46^{+0.02}_{-0.02}$	$7.51^{+0.11}_{-0.06}$
$I_{\rm Ni\ K\alpha}[10^{-4}]^2$	–	–	$1.57^{+0.25}_{-0.25}$	$0.67^{+0.62}_{-0.62}$
$\rm EQW^3_{Ni\ K\alpha}$ [eV]	–	–	15^{+9}_{-7}	$5.7^{+13.4}_{-5.7}$

Note. — (1)Units are ph keV^{-1} cm^{-2} s^{-1}, (2) Units are ph cm^{-2} s^{-1}, (3) Values of EQWs are determined relative to the abs. continuum, Absorbed and unabsorbed flux units are [10^{-10} erg sec^{-1} cm^{-2}], (5) Values of C are with respect to XIS 0 for the FI fits and XIS 1 for the BI fits.

the FI data for both observations, for reasons mentioned above.

6.3.2 Spectral results

The best fit spectral parameters were generally consistent with previous observations, with the exception of the cutoff energy. With a value of $29.2^{+13.5}_{-2.1}$ keV, $E_{\rm cut}$ was significantly higher than the ~ 20 keV value measured in previous *RXTE* (Mukherjee & Paul, 2004) and *BeppoSAX* (La Barbera et al., 2005) observations, although these observations used slightly different spectral models for the cutoff energy. Kreykenbohm et al. (2004) also used the Fermi–Dirac cutoff, resulting in cutoff energies of $10 - 15$ keV. The folding energy for Obs. 1, $E_{\rm fold} = 10.3^{+3.1}_{-3.0}$ keV, is consistent with values obtained for a similar orbital phase with *BeppoSAX* (La Barbera et al., 2005). In Obs. 2, the value of $E_{\rm fold} = 5.7^{+0.4}_{-2.5}$ keV is consistent with the *RXTE* data for the pre-periastron flare and the periastron passage (Kreykenbohm et al., 2004).

The observed column densities for the absorption due to the smooth stellar wind ($N_{\rm H,1}$) were consistent between both observations. A larger difference could be observed in the column density associated with the absorption due to the clumped wind ($N_{\rm H,2}$), where the best fit value of Obs. 1 is almost a factor three larger than that of Obs. 2. In addition to the H column density in the `TBnew` model, the relative Ca and Fe abundances were also left independent in Obs. 2. The best fit values are measured from the Ca and Fe K edges at 4.1 keV and 7.1 keV, respectively, and were slightly higher than solar abundances: $1.55^{+0.39}_{-0.18}$ for Ca and $1.17^{+0.04}_{-0.03}$ for Fe. For the first observation, the Ca and Fe abundances could not be well constrained and were fixed to 1.55 for Ca and 1.17 for Fe.

The partial covering fractions can be calculated from the measured normalization values of the two power law components, $A_{\rm PL1}$ and $A_{\rm PL2}$:

$$\text{Cvr. Frac.} = \frac{A_{\rm PL2}}{A_{\rm PL1} + A_{\rm PL2}}. \tag{6.1}$$

The factor is almost unity in both observations due to the dominance of the $A_{\rm PL2}$ value. Similar large covering fractions have been observed in *XMM-Newton* data (Fürst et al., 2011b) and in the *RXTE* data (Mukherjee & Paul, 2004), indicating

that the covering fraction does not change significantly for different parts of the orbit. The spectrum softened slightly from $\Gamma = 0.83^{+0.08}_{-0.06}$ for Obs. 1 to $0.96^{+0.06}_{-0.04}$ for Obs. 2.

The Fe Kα line was detected at $6.409^{+0.003}_{-0.001}$ keV (Obs. 2), which is, given the instrumental gain systematics, consistent with neutral Fe. In addition, the following lines have also been observed in both observations: S Kα line, Ar Kα line, Ca Kα line, Fe Kβ line, and the Ni Kα line, all with energies consistent with neutral material (e.g. Kaastra & Mewe, 1993). Note that the Ni Kα line was not detected in the fainter first observation. The observed line intensities are summarized in table 6.2 with 90% confidence errors. The values are consistent between the FI and BI instruments. The widths of the lines were set to be equal to the Fe Kα width within each observation, which was found to be 13^{+22}_{-2} eV for Obs. 1 and had an upper limit of 5 eV in Obs. 2 (FI values). The Compton shoulder to the Fe Kα line, as observed by the *Chandra* observatory (Watanabe et al., 2003), was not significantly detected in either observation. The observation of Watanabe et al. (2003) was performed in the pre-periastron phase, where the luminosity was higher than in the two *Suzaku* observations. A Compton shoulder has also been observed with *XMM-Newton* in data taken during another pre-periastron flare (Fürst et al., 2011b).

6.4 Phase resolved analysis

Barycentric and binary corrected light curves for different energy bands were extracted for both observations using the orbital parameters from Koh et al. (1997) with an updated orbital period and periastron time t_0 determined by Doroshenko et al. (2010a). Due to the strong variability of the pulse period on short time scales, individually determined pulse periods were used for each observation. An accurate pulse period could be established for Obs. 2, but not for Obs. 1 due to its short duration of 10 ks. For the second observation the calculated pulse period had a value of $P = 685.4 \pm 0.9$ s. The *Fermi*/GBM instrument measures the pulse period of GX 301−2 on a regular basis, resulting in values of $P = 687.28$ s for Obs. 1 and

$P = 685.75\,\mathrm{s}$ for Obs. 2 (Finger, 2011, priv. comm). To create the pulse profiles, the *Fermi*/GBM-provided pulse periods and epoch times for each observation were used.

We studied the energy dependent pulse profiles for Obs. 1 and Obs. 2. Both pulse profiles are very similar, showing a double peak shape where the main peak (P1) is broader below 10 keV. The second peak (P2) stays rather constant in width, but increases its relative intensity toward higher energies. As an example, the pulse profile for Obs. 2 in different energy bands is shown in Figure 6.6. Comparing these pulse profiles with previous *RXTE* and *BeppoSAX* data showed that the general shape is consistent through all parts of the orbit.

The data of the longer Obs. 2 were divided into 10 equally spaced phase bins and individual spectra were extracted for the XIS and PIN instruments. Figure 6.6 shows the individual phase bins in the lowest panel. This division resulted in an exposure time in each phase bin of $\sim 5 - 6\,\mathrm{ks}$ for each individual instrument. No GSO data were used in this analysis due to the reduced exposure time per phase bin. For spectral analysis, the phase averaged model was applied to all phase bins, resulting in best fit values summarized in Table 6.3 and 6.4, as well as Figure 6.7. Again the cutoff energy was frozen to the phase averaged value of 29.2 keV to avoid the previously discussed degeneracy with E_{CRSF}.

The two absorbing components, $N_{\mathrm{H},1}$ from the smooth stellar wind and $N_{\mathrm{H},2}$ from the partial coverer vary between 20 and $40{\times}10^{22}$ cm^{-2}, but show an anti-correlated trend throughout the first peak. Although the error bars are rather big, one can see an indication that $N_{\mathrm{H},1}$ follows the flux in P1, whereas the $N_{\mathrm{H},2}$ value dips at the same time.

In contrast to Kreykenbohm et al. (2004), the power law index Γ is varying strongly throughout the pulse. The values are 0.9–1.3 throughout the first peak and drop suddenly to 0.6–0.8 for the second peak (Figure 6.7). Measuring the second peak to be significantly harder than the first peak supports the behavior seen in the pulse profile, where the intensity of P2 increases at higher energies, becoming similar to the intensity in P1. Power law normalizations are relatively small and badly constrained for the first power law component. The partially covered power

Table 6.3. Phase resolved spectral parameter from Obs. 2 for FI data.

Parameter	PB1	PB2	PB3	PB4	PB5
$N_{\rm H,1}[10^{22}/{\rm cm}^2]$	$19.2^{+10.2}_{-7.7}$	$20.0^{+7.9}_{-6.4}$	$36.1^{+4.6}_{-7.4}$	$20.2^{+23.6}_{-20.2}$	$32.4^{+8.3}_{-11.3}$
$N_{\rm H,2}[10^{22}/{\rm cm}^2]$	$32.6^{+5.0}_{-1.9}$	$30.9^{+4.9}_{-5.4}$	$21.3^{+13.8}_{-4.5}$	$25.0^{+21.0}_{-20.6}$	$18.7^{+9.3}_{-3.6}$
Γ	$1.22^{+0.08}_{-0.11}$	$1.30^{+0.04}_{-0.04}$	$0.93^{+0.04}_{-0.04}$	$0.91^{+0.03}_{-0.04}$	$1.20^{+0.04}_{-0.04}$
$A_{\rm PL,1}[10^{-2}]^1$ fc.	$0.97^{+3.28}_{-0.70}$	$1.35^{+3.13}_{-0.90}$	$10.12^{+8.47}_{-7.27}$	$0.29^{+25.73}_{-0.28}$	$8.69^{+24.37}_{-7.55}$
$A_{\rm PL,2}[10^{-2}]^1$ pc.	$24.4^{+4.1}_{-3.4}$	$44.8^{+4.9}_{-4.3}$	$17.4^{+6.6}_{-8.0}$	$27.4^{+2.2}_{-25.9}$	$41.1^{+77.1}_{-22.5}$
$E_{\rm fold}$ [keV]	$7.4^{+14.1}_{-2.3}$	$6.13^{+0.38}_{-0.35}$	$5.6^{+0.4}_{-0.3}$	$5.5^{+0.5}_{-0.4}$	$5.9^{+0.7}_{-0.6}$
$E_{\rm CRSF}$ [keV]	$38.7^{+9.3}_{-5.7}$	$29.8^{+1.6}_{-1.2}$	$32.1^{+1.9}_{-1.4}$	$34.6^{+3.1}_{-2.3}$	$38.0^{+2.8}_{-2.4}$
$\sigma_{\rm CRSF}$ [keV]	$10.3^{+3.7}_{-2.1}$	$5.1^{+1.7}_{-1.1}$	$6.4^{+1.2}_{-0.9}$	$7.3^{+1.4}_{-1.1}$	$6.3^{+1.3}_{-1.1}$
$\tau_{\rm CRSF}$	$33.4^{+75.1}_{-16.7}$	$3.5^{+1.5}_{-0.9}$	$6.7^{+2.4}_{-1.5}$	$8.4^{+4.7}_{-2.4}$	$8.3^{+6.0}_{-3.4}$
$I_{\rm Fe\ K\alpha}[10^{-3}]^2$	$1.97^{+0.09}_{-0.09}$	$1.82^{+0.10}_{-0.10}$	$1.86^{+0.14}_{-0.08}$	$1.89^{+0.13}_{-0.07}$	$1.72^{+0.09}_{-0.08}$
$\rm Flux^3_{2-10\,keV}$	$4.93^{+0.03}_{-0.08}$	$7.77^{+0.08}_{-0.16}$	$10.03^{+4.42}_{-0.61}$	$11.27^{+0.39}_{-3.37}$	$10.93^{+4.37}_{-0.90}$
$\rm C_{XIS3}/C^4_{PIN}$	0.94 / 1.15	0.94 / 1.15	0.95 / 1.19	0.94 / 1.21	0.94 / 1.21
χ^2/dof	233 / 243	288 / 243	353 / 243	312 / 243	253 /243
χ^2/dof no CRSF	241 / 246	307 / 246	391 / 246	341 / 246	273 / 246

Note. — (1) Units are ph keV^{-1} cm^{-2} s^{-1} fc = fully covered, pc = partially covered component, (2) Units are ph cm^{-2} s^{-1}, (3) Units are 10^{-10} erg cm^{-2} sec^{-1} , (4) Values of C are with respect to XIS 0 for the FI fits.

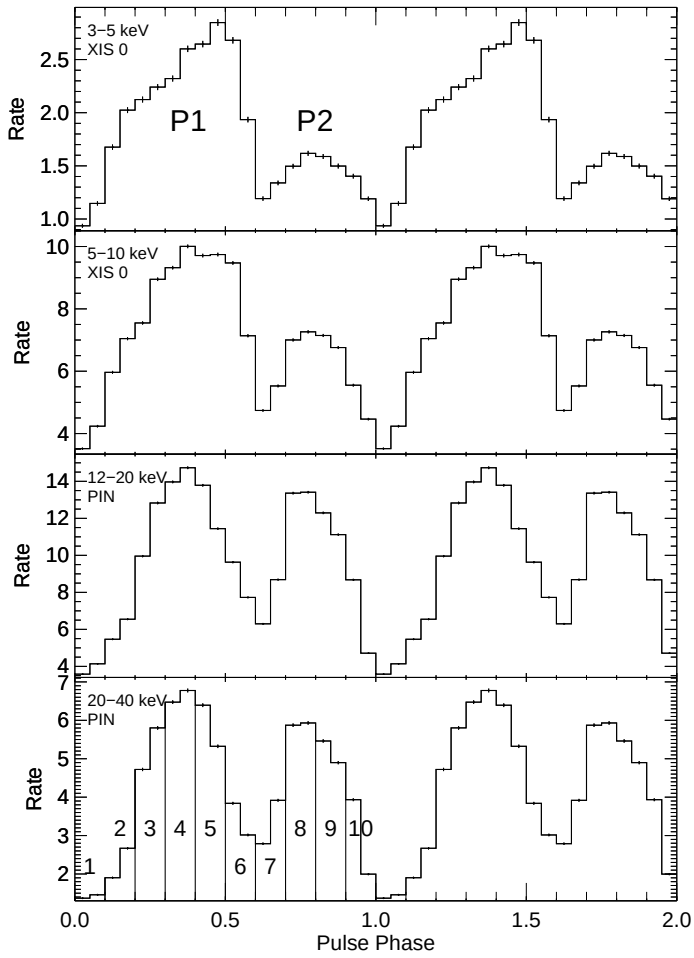

Figure 6.6 Pulse profiles for different energy bands for Obs. 2. The two peaks are indicated in the top panel. The bottom pannel shows the selection of phase bins which were used for phase resolved spectroscopy.

law normalization seems to follow the flux, showing a higher value throughout the first peak. The folding energy does not vary significantly throughout the orbit and shows values between 5 and 6 keV (not shown in Figure 6.7)

The CRSF energy varies between 30–40 keV (Figure 6.8), similar to the values observed in the *RXTE* data (Kreykenbohm et al., 2004). Table 6.3 and 6.4 shows that the addition of the CRSF in the individual spectra improved the χ^2 for most of the phase bins, except in phase bin 6, which falls in the gap between both P1 and P2. Phase bins 1 and 7, also minima in the pulse profile, only show a small improvement in the best fit when the CRSF was included. The CRSF energy is not

Table 6.4. Same as table 6.3

Parameter	PB6	PB7	PB8	PB9	PB10
$N_{\rm H,1}[10^{22}/{\rm cm}^2]$	$22.8^{+7.9}_{-7.3}$	$25.3^{+4.4}_{-4.7}$	$12.2^{+6.5}_{-4.6}$	$21.4^{+7.9}_{-7.3}$	$24.6^{+5.4}_{-5.5}$
$N_{\rm H,2}[10^{22}/{\rm cm}^2]$	$26.7^{+5.0}_{-4.1}$	$32.7^{+4.1}_{-2.8}$	$35.2^{+4.0}_{-2.8}$	$29.5^{+3.9}_{-3.9}$	$31.6^{+2.6}_{-2.8}$
Γ	$1.07^{+0.10}_{-0.22}$	$0.74^{+0.05}_{-0.05}$	$0.56^{+0.04}_{-0.04}$	$0.67^{+0.05}_{-0.05}$	$1.15^{+0.06}_{-0.06}$
$A_{\rm PL,1}[10^{-2}]^1$ fc.	$1.92^{+4.56}_{-1.44}$	$2.03^{+1.53}_{-1.00}$	$0.16^{+0.09}_{-0.27}$	$0.83^{+1.74}_{-0.57}$	$2.36^{+2.62}_{-1.33}$
$A_{\rm PL,2}[10^{-2}]^1$ pc.	$27.7^{+3.9}_{-4.3}$	$10.8^{+2.0}_{-2.0}$	$10.6^{+1.0}_{-1.0}$	$11.3^{+1.4}_{1.4}$	$19.3^{+3.0}_{-2.7}$
$E_{\rm fold}$ [keV]	$4.1^{+5.0}_{-0.9}$	$4.5^{+0.8}_{-0.6}$	$5.0^{+0.5}_{-0.4}$	$4.4^{+0.3}_{-0.3}$	$5.0^{+0.4}_{-0.3}$
$E_{\rm CRSF}$ [keV]	$38.3^{+22.9}_{-8.2}$	$35.4^{+4.1}_{-3.0}$	$35.7^{+1.9}_{-1.5}$	$31.1^{+1.4}_{-1.0}$	$27.5^{+1.1}_{-0.8}$
$\sigma_{\rm CRSF}$ [keV]	$15.1^{+15.0}_{-6.0}$	$8.4^{+1.6}_{-1.2}$	$8.1^{+0.9}_{-0.7}$	$6.7^{+0.9}_{-0.7}$	$4.2^{+1.1}_{-0.8}$
$\tau_{\rm CRSF}$	$30.5^{+30.0}_{-19.0}$	$17.0^{+10.3}_{-5.2}$	$21.8^{+6.0}_{-3.8}$	$11.4^{+2.8}_{-1.9}$	$3.9^{+1.2}_{-0.9}$
$I_{\rm Fe\ K\alpha}[10^{-3}]^2$	$1.76^{+0.12}_{-0.11}$	$1.87^{+0.12}_{-0.11}$	$2.16^{+0.11}_{-0.11}$	$2.11^{+0.11}_{-0.11}$	$2.07^{+0.10}_{-0.10}$
$\rm Flux^3_{2-10\,keV}$	$7.76^{+7.04}_{-3.52}$	$6.56^{+0.05}_{-0.62}$	$8.47^{+0.17}_{-0.20}$	$7.62^{+0.10}_{-0.22}$	$4.89^{+0.05}_{-0.16}$
$\rm C_{XIS3}/C^4_{PIN}$	0.94 / 1.19	0.95 / 1.16	0.95 / 1.14	0.94 / 1.10	0.94 / 1.11
χ^2/dof	303 / 243	283 / 243	292 / 243	264 / 243	247 / 243
χ^2/dof no CRSF	305 / 246	291 / 246	344 / 246	297 / 246	270 / 246

Note. — (1) Units are ph keV^{-1} cm^{-2} s^{-1} fc = fully covered, pc = partially covered component, (2) Units are ph cm^{-2} s^{-1}, (3) Units are 10^{-10} erg cm^{-2} sec^{-1} , (4) Values of C are with respect to XIS 0 for the FI fits.

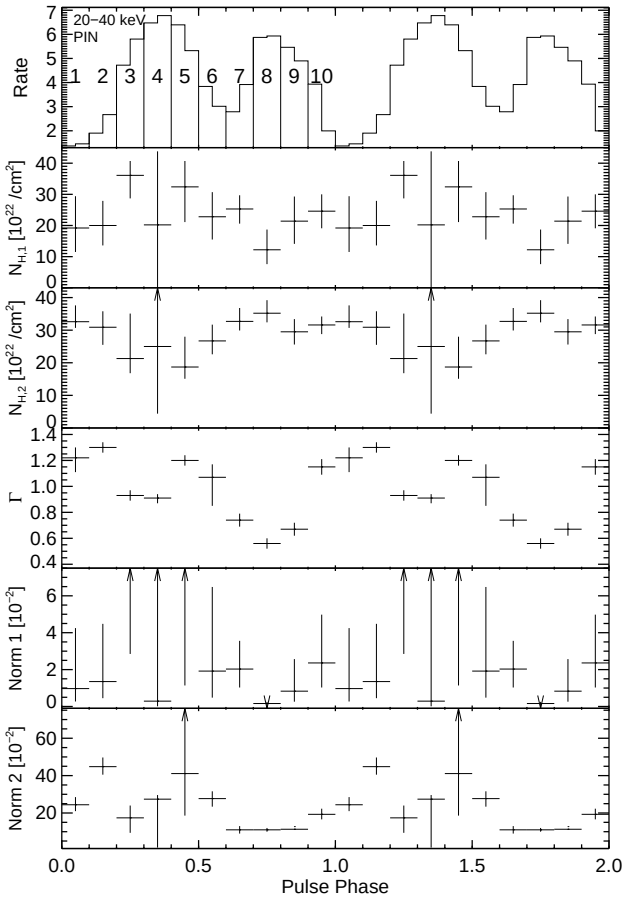

Figure 6.7 Phase resolved spectral parameters for Obs. 2. Top panel shows the $20 - 40\,\mathrm{keV}$ pulse profile, where the individual phase bins are numbered. Units of power law normalization are ph keV^{-1} cm^{-2} s^{-1}. For clarity, two pulses are shown.

very well constrained in phase bins 1 and 6 due to the lack of sufficient statistics. For the geometrical discussion below, these two phase bins are ignored. In all other phase bins the addition of the CRSF improves the fit. The energy changes very smoothly throughout the pulse and does not follow explicitly the observed flux in each phase bin. The CRSF energy increases during the main peak and reaches the maximum at the falling flank of P1. During P2 the CRSF energy decreases until it reaches a minimum at the dip between P2 and P1.

To estimate the significance of the CRSF in the phase resolved analysis, again the null hypothesis method was applied in two out of the 8 remaining phase bins, which are good representatives of all data points. Phase bin 2 is a good example for a shallow CRSF, whereas phase bin 5 is an example for a phase bin

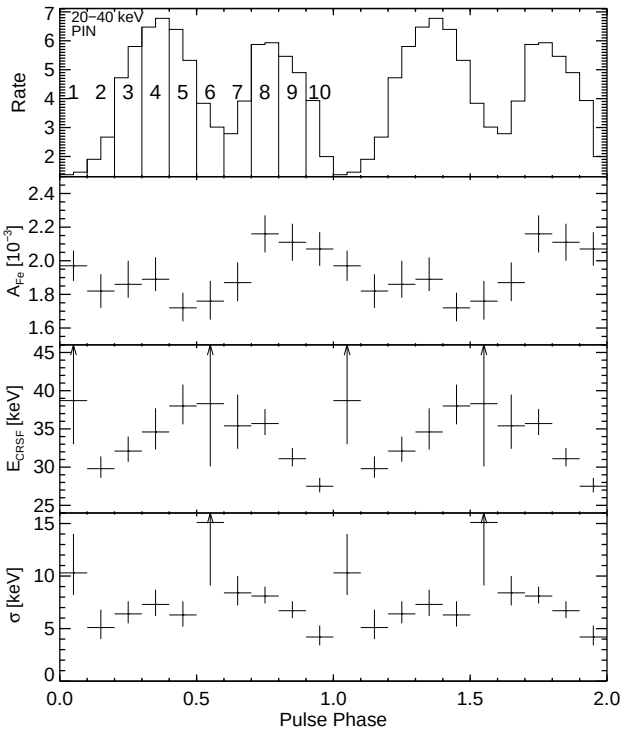

Figure 6.8 Same as Figure 6.7 for the CRSF and Fe normalization. Top panel shows the $20-40$ keV pulse profile, where the individual phase bins are numbered. The intensity of the Fe line is units of ph cm^{-2} s^{-1}. For clarity, two pulses are shown.

with a higher flux. Similarly as with the phase averaged data, 10,000 spectra were simulated and modeled without and with the CRSF. The interpretation of the observed feature as being due to stochastic fluctuations with a depth similar to the observed values could be ruled out with a probability of over 99% ($\sigma \sim 3$) in both phase bins. This leads to the conclusion that the CRSF can be observed with sufficient significance to allow the interpretation below.

6.5 Discussion

6.5.1 Phase averaged continuum

In both observations very strong absorption can be observed. $N_{\mathrm{H},1}$, which is the absorption due to the smooth stellar wind, is consistent within both observations. $N_{\mathrm{H},2}$, the absorption from the partial coverer, is significantly stronger in

the first observation, establishing the existence of an additional component in the line of sight. Leahy & Kostka (2008) used *RXTE*/ASM and PCA data to show that a stellar wind and a stream model component can describe the observed count rate throughout the orbit and that the increase of the column density at orbital phase ~ 0.2 is mainly due to the stream component. The findings in both *Suzaku* observations are supportive of this theoretical picture.

GX 301−2 shows very strong luminosity variability on very short time scales (Kreykenbohm et al., 2004; Fürst et al., 2011b), where the column density increases to up to 50% in periods of lower activity. Both *RXTE* and *XMM-Newton* data showed a much higher column density in the pre-periastron flare than in the two data points observed with *Suzaku*. One possible explanation is that the wind is indeed so variable and clumpy that these variations are just not properly predictable, especially in times of high activity, such as the pre-periastron flare. Leahy & Kostka (2008) investigated *RXTE*/PCA $N_{\rm H}$ values of the absorbed component from archival observations for different parts of the orbit and found no increased column density in the pre-periastron flare. Observations throughout one full binary orbit could help to understand the variations in $N_{\rm H}$ on time scales of days.

The observed luminosity dependence of the power law index Γ and the folding energy is similar to other sources, such as V0332+53 (Mowlavi et al., 2006) and 4U0115+63 (Tsygankov et al., 2007). The power law index Γ shows a hardening for the first observation, whereas the folding energy $E_{\rm fold}$ is slightly higher when compared to Obs. 2. Soong et al. (1990) observed the $E_{\rm fold}$ variation in Her X-1 phase resolved *HEAO-1* data and concluded that the parameter is dependent on the viewing angle of the accretion column and can be used to describe the plasma temperature of the system. In the case of GX 301−2 the smaller $E_{\rm fold}$ value in Obs. 2 could indicate a lower plasma temperature which can be interpreted that the X-ray emission region is further up in the accretion column (Basko & Sunyaev, 1976) (see also Section 5.2).

The softening of the power law index Γ with increased luminosity is also in agreement with the basic model of the accretion column that the plasma temperature decreases with increased height. With increased luminosity, the rate of

accreted material would increase and the amount of soft photons created by the lateral walls of the relatively taller column would increase, leading to a softer spectrum, as is observed.

For the second observation the abundances for Fe and Ca were left independent and a slight overabundance was observed. Taking into consideration that the abundances used in Wilms et al. (2000) are derived from the interstellar medium (ISM) a small overabundance from an evolved star may be expected.

6.5.2 Variations in the CRSF parameters

In both observations the CRSF was clearly observed and the `gabs` absorption component improved the overall fit significantly. Using the $E_{\rm CRSF}$ values obtained in the phase averaged spectra and the **12-B-12** formula discussed in chapter 3, the calculated magnetic field has a strength of $4.76^{+0.36}_{-0.67} \times 10^{12}$ G (Obs. 1) and $4.10^{+0.15}_{-0.10} \times 10^{12}$ G (Obs. 2) which is consistent within errors for both observations.

The CRSF parameters are consistent with previous results using *RXTE* data and are lower than the observed *BeppoSAX* (La Barbera et al., 2005) and *INTEGRAL* (Doroshenko et al., 2010b) values of $45 - 50$ keV. These observations were obtained during pre-periastron outburst, where the luminosity of the source is much higher than in the two *Suzaku* observations presented in this paper. A luminosity dependence of the phase-averaged CRSF centroid energy is observed in multiple other sources, where an anti-correlation between CRSF and luminosity was observed in V 0332+53 and 4U 0115+63 (Tsygankov et al., 2006; Mihara et al., 2007), and a positive correlation was observed in Her X-1 (Staubert et al., 2007). Klochkov et al. (2011) have confirmed, from pulse to pulse variability studies, such correlations for V 0332+53, 4U 0115+63 and Her X-1, and also found an anti-correlation for A 0535+26. Although the CRSF values are consistent with a single value in both *Suzaku* observations, a hint of an anti-correlation can be seen in the data. Compared with the *BeppoSAX* and *INTEGRAL* data, the CRSF centroid energy might have a positive correlation. Parallel to the CRSF-luminosity correlation, Klochkov et al. (2011) also observed in pulse to pulse data of four sources that the power law index Γ shows an opposite luminosity dependence than

the E_{CRSF}. In the *Suzaku* observations discussed here, Γ is observed to soften with increased luminosity, another indication that a possible negative CRSF-luminosity correlation exists.

The two opposite scenarios seem to depend on the luminosity, i.e., if the observed luminosity is below or above a critical luminosity (CL) which can be derived from the Eddington luminosity of a system (Becker & Wolff, 2007). The CL is of order $\sim 10^{37}\,\mathrm{erg\,s^{-1}}$, but depends also on the accretion geometry (spherical or disc) as well as the height and diameter of the accretion column.

Above the CL, the infalling proton density becomes so large that the protons begin to interact and decelerate, creating a radiation pressure dominated shock region above the magnetic pole. This region of increased density is most likely the region where the CRSF is created (Basko & Sunyaev, 1973). With increasing luminosity, the shock region moves higher up in the accretion column, where a smaller local magnetic field value results in a lower observed CRSF centroid energy, as is observed in V 0332+53 or 4U 0115+63. The observed CRSF-luminosity dependence as well as the Γ-luminosity dependence in GX 301−2 is very similar to the scenario described here.

Below the CL, the accreting matter slows down via hydrodynamical shock, 'Coulomb friction' or nuclear collision (Basko & Sunyaev, 1973; Braun & Yahel, 1984). With increasing accretion rate, the luminosity increases and the deceleration region is pushed closer to the NS surface, where the magnetic fields are higher. This would result in a positive CRSF-luminosity correlation, as observed in Her X-1 and A 0535+26.

With a distance of 3 kpc, the intrinsic unabsorbed $2-10\,\mathrm{keV}$ luminosity of $\sim 2\times10^{35}\,\mathrm{erg\,s^{-1}}$ is significantly below the typical CL of $\sim 10^{37}\,\mathrm{erg\,s^{-1}}$. Although it has been observed that sources with similar luminosities can show the opposite correlation (Klochkov et al., 2011) due to individual critical luminosity values, the large luminosity difference compared to CL puts this source in the same regime as Her X-1 and A 0535+26 and at odds with the notion of a well-defined CL. The observed variation in Γ and possibly in E_{CRSF} would then stem from another mechanism.

6.5.3 Emission lines

The existence of multiple fluorescence emission lines, especially at lower energies, where the absorption is very dominant, indicates that the source of the emission originates from a region where the column density is not very large, i.e. the outer layers of the stellar wind in our line of sight (Fürst et al., 2011b). If the emission lines would be embedded deeper in the stellar wind, the lines, especially at lower energies would have to be significantly stronger, to be detected at all. On the other hand, if the line emitting region is in the outer layers of the wind, the incident soft X-ray flux would be drastically reduced, making the equivalent width very large, as observed in the low energy emission lines (Table 1). A possible explanation would be that the emission region is very large for the lines, and may be spread over the entire surface of the stellar wind.

The most dominant line emission stems from the Fe Kα transition at 6.4 keV. The observed energies in both observations are consistent with the emission in neutral material. The ratio of the intensities of Fe Kβ/Fe Kα for both observations, $0.16^{+0.05}_{-0.04}$ for Obs. 1 and $0.14^{+0.01}_{-0.01}$ for Obs. 2, is consistent with the fluorescing material being neutral or only slightly ionized (Kaastra & Mewe, 1993). The equivalent widths (EQW) of the two Fe Kα lines show that the intensity relative to the continuum is reduced by a factor of ~ 2 in the second observation. Based on emission line widths, Endo et al. (2002) estimated in *ASCA* data that the Fe emission originates within 10^{10} cm of the continuum emission source. Fürst et al. (2011b) use *XMM-Newton* pulse by pulse observations to observe a correlation with increased flux of the source, showing that the Fe emission region is not far from the X-ray source. In the *Suzaku* observation, however, the Fe Kα line flux does not directly follow the observed luminosity. The increase in absorbed $2-10$ keV luminosity is a factor of ~ 5, whereas the increase in the fluorescence line intensities is only $2-3$. This difference in intensity change indicates that the distance between continuum and fluorescence emission lines is large, especially when compared to the proposed ~ 0.3 lt-s from Endo et al. (2002). In the 6 months' time between the two observations, however, the overall emission geometry could have changed, accounting for the difference in the fluorescence intensities. If the

emission originates from a confined region in the stellar wind, observations taken during two different orbital phases would each yield a different distance to this region.

In addition to the strong Fe Kα line, many other emission lines are observed in the XIS spectra in both observations. The observed intensities of these lines show the same behavior, where the flux for the second observation is $\sim 50\%$ or less compared to the first observation, although the observed uncertainties for the different lines, especially for S Kα and Ar Kα, are very large. Furthermore, the S Kα line falls into an energy regime where calibration uncertainties have been previously observed (e.g., Suchy et al., 2011b), so that a detailed analysis is not possible at this time.

6.5.4 Pulse profiles

Historically, GX 301−2 shows very strong pulse to pulse variations and an intensive flaring behavior on very short time scales (Kreykenbohm et al., 2004; Fürst et al., 2011b), e.g., throughout the pre-periastron flare. The observations obtained here do not show such flaring behavior, and only show the regular pulsation throughout the observation. A pulse period could only be established for Obs. 2 of the *Suzaku* data, which was consistent with *Fermi*/GBM data. With the GBM pulse period for the first observation, pulse profiles for both observations could be produced for different energy bands. The two peaked pulse profiles show a similar behavior for both observations, where the second peak is getting strong at higher energies. This behavior is in contrast to many similar sources, such as 4U 0115+63 (Tsygankov et al., 2007), V 0332+53 (Tsygankov et al., 2006), 4U 1909+07 (Fürst et al., 2011a), and 1A1118−61 (Suchy et al., 2011b), where the pulse profile turns into a single peak profile at higher energies. A reduction in the intensity of the second pulse has also been observed in *BeppoSAX* data for different parts of the orbit (La Barbera et al., 2005).

6.5.5 Geometrical constraints using a simple dipole model

The phase resolved analysis of the second observation showed strong variations in several spectral parameters throughout the pulse profile. As previously observed by Kreykenbohm et al. (2004), the CRSF centroid energy varies by $\sim 30\%$ where the highest energy is detected at the peak and the falling flank of P1. Such behavior has been observed in multiple other sources, e.g., Vela X-1 (La Barbera et al., 2003), 4U 0352+309 (Coburn, 2001), and Her X-1 (Klochkov et al., 2008b). In chapter 3. I discussed a simple model based on the changes in the viewing angle throughout the pulse and thus probing different heights of the accretion column.

A simple approach to derive a possible geometry for the neutron star and the magnetic field uses the variation in the observed magnetic field throughout the pulse phase. In this case the very smooth and sinusoidal variation (Figure 6.9) can be modeled as a simple dipole where the total magnetic moment μ is calculated from the phase averaged CRSF energy value.

The variation of the CRSF energy is then fitted by changing the geometrical angles of the system until a best fit converges. Chapter 3.5 discusses the model in detail, introducing the three free parameters: Θ, the viewing angle between line of sight and the NS spin axis, the inclination angle α of the magnetic moment with respect to the spin axis, and the angle β, indicating the 'lag' of the B-field plane with respect to the ephemeris, i.e., the observed shift in pulse phase (see also Figure 3.8) The best fit values for β were either $-4.6°$ or $175.4°$, depending on the starting values of the fit (see Appendix A), where the latter value is equivalent to the former when the dipole polarity is flipped. α and Θ angles showed a very strong interdependence, and the best fit Θ/α pairs were: $-14.6°/67°$, $14.6°/113°$, $67°/-14.6°$, and $113°/14.6°$. All best fit values have a $\chi^2 \approx 4$ with 7 dof. These pairs do show a degeneracy of $0 \pm 14.6°$ and $90 \pm 23°$, which can be explained with a geometrical symmetry, when calculating the magnetic field for each individual phase bin. The first and last two pairs can be each treated as the same geometry, rotated by 180 degrees. Figure 6.9 shows the calculated magnetic field values from the CRSF centroid energies and the theoretical values for B from the best fit angles for a simple dipole model with $\Theta = -14.6°$, $\alpha = 67°$ and $\beta = -4.6°$.

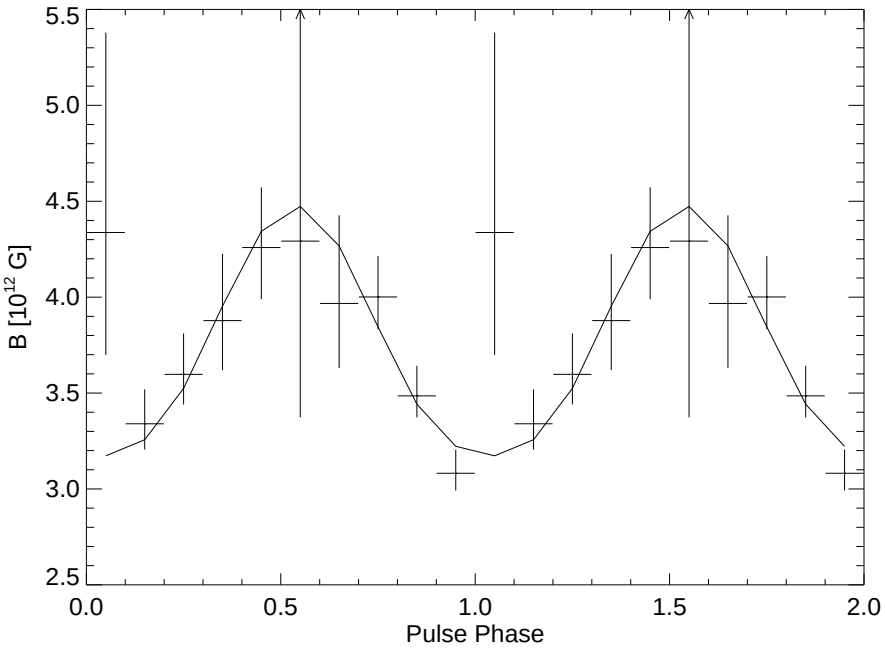

Figure 6.9 Calculated phase resolved magnetic fields from the CRSF energy and the best fit for a simple magnetic dipole model.

The phase resolved energy and width of the CRSF show a strong correlation, where the width varies in phase with the CRSF energy (Figure. 7). Kreykenbohm et al. (2004) observed a similar correlation, where the magnetic pole was observed under different viewing angles Φ, where Φ is the angle between the line of sight and the magnetic axis. Meszaros & Nagel (1985b) showed that the anisotropic velocity field of the electrons in the accretion column leads to a fractional line width of:

$$\frac{\sigma_{\rm CRSF}}{E_{\rm CRSF}} \approx \sqrt{8{\rm ln}2\frac{kT_{\rm e}}{m_{\rm e}c^2}}|{\rm cos}\Phi| = k|{\rm cos}\Phi|. \qquad (6.2)$$

The $\sigma_{\rm CRSF}/E_{\rm CRSF}$ ratios vary in the 0.16 – 0.24 range, corresponding to variations of $\pm$20% throughout the pulse phase. The two outliers with large errors in phase bins 1 and 6 were ignored. The variation of Φ can be estimated as $\Theta - \alpha$ and $\Theta + \alpha$ throughout one pulse phase, where the magnetic pole rotates around the NS spin axis, tilted by Θ with respect to the line of sight.

Using the average ratio of 0.2, we calculated the values of k for the two geometries with $\Theta = -14.6^\circ$ ($k = 0.21$) and $\Theta = 67^\circ$ ($k = 0.51$). For each geometry, we used the variation of the $\sigma_{\rm CRSF}/E_{\rm CRSF}$ ratio ($\pm$0.04) to calculate the variation in Φ, resulting in values of $\Phi = 15^\circ \pm 25^\circ$ and $\Phi = 67^\circ \pm 5^\circ$. These

variations are smaller than the values expected from the the geometrical discussion, but show a similar behavior, where the variation of the angle is larger for the smaller value of Φ. From Equation 4, we were also able to estimate a possible plasma temperature for the two geometries from the calculated values of k. The plasma temperature of $kT \sim 4\,\mathrm{keV}$ for $\Theta = 15^\circ$ is very similar to the observed folding energy E_{fold}, which is an indication of the plasma temperature (Burderi et al., 2000, and references therein). The value of $kT \sim 24\,\mathrm{keV}$ for the $\Theta = 67^\circ$ geometry is much larger and is not consistent with the observed E_{fold}. Assuming that the NS spin axis is aligned with the inclination of the binary system, a value of $\Theta = 15^\circ$ would put the inclination at $i \sim 75^\circ$, a value which is only marginally above the upper limit of 72°, as determined by Kaper et al. (2006).

The strong Fe line was detected in all 10 phase bins. The measured line flux did not change significantly throughout the pulse phase, while the $2 - 10\,\mathrm{keV}$ flux varied by more than a factor of 2. From this we conclude that the distance to the Fe fluorescence region is greater than $\sim$ 700 lt-s ($\sim 2 \times 10^{13}\,\mathrm{cm}$), from the NS. This is in conflict with the conclusion of Endo et al. (2002) that the emission region must be closer than $10^{10}\,\mathrm{cm}$ from the NS, based upon the width of the emission lines measured by ASCA. Their assumption is that the emission region is close to the NS and that the material free falls onto the NS surface, encountering much faster velocities, which caused the observed broadening of the lines. The smaller measured Fe Kα line width in the phase averaged spectra is more consistent with the assumption that the line broadening is due to the terminal velocity of $300 - 400\,\mathrm{km}$ of the line driven wind (Parkes et al., 1980).

The material in Chapter 6 was accepted for publication in the following publication: Suchy, Slawomir; Fuerst, Felix; Pottschmidt, Katja; Caballero, Isabel; Kreykenbohm, Ingo; Wilms, Joern; Markowitz, Alex; Rothschild, Richard E.,"Broadband spectroscopy using two Suzaku observation of the HMXB GX 301-2", The Astrophysical Journal, 2011, accepted.

Chapter 7

Summary and Outlook

7.1 Summary

In this dissertation I presented a detailed study of the three high mass X-ray binaries Cen X-3, 1A 1118−61, and GX 301−2. Sources like these give us a unique opportunity to study matter under extreme conditions, i.e., very high magnetic fields and extreme temperatures, which can not be recreated on earth. I used the spectra and light curves in these sources to derive information about the geometry of the accretion above the magnetic poles of the neutron star.

One of the main goals of this study was to better understand cyclotron resonance scattering features (CRSFs), which are the only direct method to measure the magnetic fields of a neutron star. Up to this date, only $\sim$ 17 sources have shown a CRSF, making the general understanding of these features rather challenging. Together with my collaborator in Germany, we discovered a CRSF in the transient binary 1A 1118−61, which indicates one of the highest known magnetic fields in an accreting X-ray pulsar.

As shown in early work by Araya-Góchez & Harding (2000) and later by Schönherr et al. (2007), CRSFs are very sensitive to changes in the physical conditions surrounding the emission region in the accretion column. Another factor playing into the variations of the line parameters is the angle under which the accretion column is observed. I showed that by using the variation of the CRSF throughout the rotation of the neutron star (GX 301−2), it is possible to derive

some geometrical constraints about the orientation of magnetic poles of the system. In other cases (Cen X-3), the asymmetric change in the CRSF energy indicates that the magnetic field can not be described by a simple dipole and that a more complex geometry has to be introduced.

Luminosity dependences of the CRSFs has been observed in multiple sources, and another candidate was added in the transient 1A 1118−61 throughout its outburst. Peculiar in this source was that the observed decrease of the CRSF centroid energy contradicts the behavior observed in other Be-Binaries, where a negative correlation was observed. A negative correlation indicates that the observed luminosities are below the Eddington luminosity of this system, which not the case during the peak of the outburst.

In all sources, the Fe Kα emission line could be observed. I used the observed variation in the Fe emission line 1A 1118−61 to estimate the distance of the Fe fluorescence region to the continuum emission region. Although not very robust, I found that the distance in 1A 1118−61 is < 0.7 days. In comparison, in GX 301−2 I could not recreate the results of Endo et al. (2002) and Fürst et al. (2011b), who put the emission region within 0.3 lt-s of the continuum emission region.

As part of this thesis, I also studied pulse profile variations for these three sources. All three sources showed a change in the pulse profiles, which were dependent on the luminosity and energy range. Where Cen X-3 and 1A 1118−61 showed a simpler pulse profile at higher energies, i.e., changed from a two peaked profile to a one peaked profile, GX 301−2 showed the opposite behavior. The behavior that one of the pulse profiles is dominant, while the other one decreases can be described by geometrical constraints, where one of the magnetic poles is more visible throughout the neutron star rotation, while the second pole is partially covered by the neutron star.

The change of the pulse profile with luminosity is also observed in multiple sources. When comparing the pulse profiles of Cen X-3 with earlier results by Nagase et al. (1992), where the luminosity was a factor of two smaller, I observed a simpler pulse profile. The secondary peak, which was very pronounced in the

Nagase observation, was only marginally visible in this data set. In contrast, 1A 1118−61 showed a more complex profile at higher luminosity, which could be interpreted as the change from a pencil- to fan-beam pattern. More recently Sasaki et al. (2010), among others, used a phase deconvolution method to distinguish the emission from the individual magnetic poles. From their examples, the observed peak emissions stem from both magnetic poles simultaneously, and need to be better disentangled before an interpretation can be attempted.

7.2 Future Work

So far only $\sim$ 17 sources with observed CRSFs are known. To develop a better understanding, this basis has to be further expanded, and more physical models have to be applied to the available data. Many of the known CRSF sources are transients and can only be observed when their activity increases. These transitions also generate the wide range of luminosities necessary to test the luminosity dependence processes. Future satellite mission with large effective areas and good energy resolution can be used to achieve better detections of sources in quiescence, and help to extend the knowledge of accreting X-ray pulsars. In addition, satellites with a large field of view can be used to monitor transient sources and help to discover new transients, possible new candidates for sources with CRSFs.

Theoretical work on a physical interpretation of the continuum (Becker & Wolff, 2007) and the CRSF (Schönherr et al., 2007; Schwarm, 2010) can be used for a better interpretation of the observations. Results from the pulse deconvolution technique by Sasaki et al. (2010) has also to be included to develop a more consistent picture. A systematic study of archival data of known CRSF sources can be used to develop a more consistent picture of the accretion column and the neutron star geometry.

Bibliography

Araya R.A., Harding A.K., 1999, ApJ 517, 334

Araya-Góchez R.A., Harding A.K., 2000, ApJ 544, 1067

Arnaud K.A., 1996, In: G. H. Jacoby & J. Barnes (ed.) Astronomical Data Analysis Software and Systems V, Vol. 101. Astronomical Society of the Pacific Conference Series, p. 17

Arons J., Lea S.M., 1976, ApJ 210, 792

Ash T.D.C., Reynolds A.P., Roche P., et al., 1999, MNRAS 307, 357

Audley M.D., Nagase F., Kelley R.L., Vrtilek S.D., 2001, In: H. Inoue & H. Kunieda (ed.) New Century of X-ray Astronomy, Vol. 251. Astronomical Society of the Pacific Conference Series, p.336

Baade W., Zwicky F., 1934, Physical Review 46, 76

Bardeen J., Stephen M.J., 1965, Physical Review 140, 1197

Basko M.M., Sunyaev R.A., 1973, Ap&SS 23, 117

Basko M.M., Sunyaev R.A., 1976, MNRAS 175, 395

Baym G., Pethick C., Pikes D., 1969a, Nat 224, 674

Baym G., Pethick C., Pines D., 1969b, Nat 224, 673

Becker P.A., Wolff M.T., 2005a, ApJ, Lett. 621, L45

Becker P.A., Wolff M.T., 2005b, ApJ 630, 465

Becker P.A., Wolff M.T., 2007, ApJ 654, 435

Bhattacharya D., Srinivasan G., 1995, In: W. H. G. Lewin, J. van Paradijs, & E. P. J. van den Heuvel (ed.) X-ray Binaries., p.495

Bhattacharya D., Wijers R.A.M.J., Hartman J.W., Verbunt F., 1992, A & A 254, 198

Bildsten L., Chakrabarty D., Chiu J., et al., 1997, ApJS 113, 367

Bisnovaty-Kogan G.S., Kazhdan Y.M., Klypin A.A., et al., 1979, SvA 23, 201

Blondin J.M., 1994, ApJ 435, 756

Blondin J.M., Kallman T.R., Fryxell B.A., Taam R.E., 1990, ApJ 356, 591

Blondin J.M., Stevens I.R., Kallman T.R., 1991, ApJ 371, 684

Boggs S.E., Lin R.P., Feffer P.T., et al., 1998, Advances in Space Research 21, 1015

Boldt E., 1987, In: A. Hewitt, G. Burbidge, & L. Z. Fang (ed.) Observational Cosmology, Vol. 124. IAU Symposium, p.611

Bondi H., Hoyle F., 1944, MNRAS 104, 273

Bradt H.V., Rothschild R.E., Swank J.H., 1993, A&AS 97, 355

Braun A., Yahel R.Z., 1984, ApJ 278, 349

Burderi L., Di Salvo T., Robba N.R., et al., 2000, ApJ 530, 429

Burnard D.J., Klein R.I., Arons J., 1990, ApJ 349, 262

Caballero I., 2009, Ph.D. thesis, IAAT University of Tuebingen

Caballero I., Kraus U., Postnov K., et al., 2008, In: Proceedings of the 7th INTEGRAL Workshop. 8 - 11 September 2008 Copenhagen, Denmark., p.110.

Caballero I., Kretschmar P., Santangelo A., et al., 2007, A & A 465, L21

Castor J.I., Abbott D.C., Klein R.I., 1975, ApJ 195, 157

Chevalier C., Ilovaisky S.A., 1975, IAU Circ. 2778, 1

Clark G.W., Minato J.R., Mi G., 1988, ApJ 324, 974

Clark G.W., Woo J.W., Nagase F., et al., 1990, ApJ 353, 274

Coburn W., 2001, Ph.D. thesis, UC San Diego

Coburn W., Heindl W.A., Gruber D.E., et al., 2001, ApJ 552, 738

Coburn W., Heindl W.A., Rothschild R.E., et al., 2002, ApJ 580, 394

Coe M.J., Payne B.J., 1985, Ap&SS 109, 175

Coe M.J., Roche P., Everall C., et al., 1994, A & A 289, 784

Comastri A., Setti G., Zamorani G., Hasinger G., 1995, A & A 296, 1

Corbet R.H.D., 1986, MNRAS 220, 1047

Córdova F.A.D., 1995, In: W. H. G. Lewin, J. van Paradijs, & E. P. J. van den Heuvel (ed.) X-ray Binaries., p.331

Cusumano G., di Salvo T., Burderi L., et al., 1998, A & A 338, L79

Davidson K., Ostriker J.P., 1973, ApJ 179, 585

Day C.S.R., Stevens I.R., 1993, ApJ 403, 322

Day C.S.R., Tennant A.F., 1991, MNRAS 251, 76

de Loore C., Giovannelli F., van Dessel E.L., et al., 1984, A & A 141, 279

DeCesar M., T. B.P., K. P., et al., 2011, ApJ, in prep.

Doroshenko V., Santangelo A., Suleimanov V., et al., 2010a, A & A 515, A10

Doroshenko V., Suchy S., Santangelo A., et al., 2010b, A & A 515, L1

Elsner R.F., Lamb F.K., 1977, ApJ 215, 897

Endo T., Ishida M., Masai K., et al., 2002, ApJ 574, 879

Espinoza C.M., Lyne A.G., Stappers B.W., Kramer M., 2011, MNRAS 414, 1679

Evangelista Y., Feroci M., Costa E., et al., 2010, ApJ 708, 1663

Eyles C.J., Skinner G.K., Willmore A.P., Rosenberg F.D., 1975, Nat 254, 577

Fabian A.C., 1975, MNRAS 173, 161

Ferrigno C., Becker P.A., Segreto A., et al., 2009, A & A 498, 825

Forman W., Jones C., Cominsky L., et al., 1978, ApJS 38, 357

Freeman P.E., Lamb D.Q., Wang J.C.L., et al., 1999, ApJ 524, 772

Friend D.B., Abbott D.C., 1986, ApJ 311, 701

Fürst F., Kreykenbohm I., Suchy S., et al., 2011a, A & A 525, 73

Fürst F., Suchy S., Kreykenbohm I., et al., 2011b, A & A 535, 9

Fürst F., Wilms J., Rothschild R.E., et al., 2009, Earth and Planetary Science Letters 281, 125

Gehrels N., Chincarini G., Giommi P., et al., 2004, ApJ 611, 1005

Geppert U., Urpin V., 1994, MNRAS 271, 490

Ghosh P., Lamb F.K., 1978, ApJ, Lett. 223, L83

Ghosh P., Lamb F.K., 1979a, ApJ 232, 259

Ghosh P., Lamb F.K., 1979b, ApJ 234, 296

Giacconi R., Branduardi G., Briel U., et al., 1979, ApJ 230, 540

Giacconi R., Gursky H., Kellogg E., et al., 1971a, ApJ, Lett. 167, L67

Giacconi R., Gursky H., Paolini F.R., Rossi B.B., 1962, Physical Review Letters 9, 439

Giacconi R., Kellogg E., Gorenstein P., et al., 1971b, ApJ, Lett. 165, L27

Göğüş E., Kreykenbohm I., Belloni T.M., 2011, A & A 525, L6

Gruber D.E., Heindl W.A., Rothschild R.E., et al., 2001, ApJ 562, 499

Haberl F., White N.E., 1990, ApJ 361, 225

Haberl F., White N.E., Kallman T.R., 1989, ApJ 343, 409

Haigh N.J., Coe M.J., Steele I.A., Fabregat J., 1999, MNRAS 310, L21

Hameury J.M., Bonazzola S., Heyvaerts J., 1980, A & A 90, 359

Harding A.K., 1994, In: S. Holt & C. S. Day (ed.) The Evolution of X-ray Binariese, Vol. 308. American Institute of Physics Conference Series, p.429

Harding A.K., Daugherty J.K., 1991, ApJ 374, 687

Harding A.K., Kirk J.G., Galloway D.J., Meszaros P., 1984, ApJ 278, 369

Harrison F.A., Boggs S.E., Bolotnikov A.E., et al., 2000, In: J. E. Truemper & B. Aschenbach (ed.) Society of Photo-Optical Instrumentation Engineers (SPIE) Conference Series, Vol. 4012. Society of Photo-Optical Instrumentation Engineers (SPIE) Conference Series, p.693

Hasinger G., Bergeron J., Mainieri V., et al., 2002, The Messenger 108, 11

Heindl W., Coburn W., Kreykenbohm I., Wilms J., 2003, The Astronomer's Telegram 200, 1

Heindl W.A., Coburn W., Gruber D.E., et al., 1999, ApJ, Lett. 521, L49

Heindl W.A., Coburn W., Gruber D.E., et al., 2001, ApJ, Lett. 563, L35

Herold H., 1979, Phys. Rev. D 19, 2868

Hertzsprung E., 1911, Publikationen des Astrophysikalischen Observatoriums zu Potsdam 63

Hewish A., Bell S.J., Pilkington J.D.H., et al., 1968, Nat 217, 709

Hua X.M., Titarchuk L., 1995, ApJ 449, 188

Hutchings J.B., Cowley A.P., Crampton D., et al., 1979, ApJ 229, 1079

Iaria R., Di Salvo T., Robba N.R., et al., 2005, ApJ, Lett. 634, L161

Iben, Jr. I., 1991, ApJS 76, 55

Iben, Jr. I., Tutukov A.V., 1985, ApJS 58, 661

Illarionov A.F., Sunyaev R.A., 1975, A & A 39, 185

Isenberg M., Lamb D.Q., Wang J.C.L., 1998, ApJ 505, 688

Ives J.C., Sanford P.W., Bell Burnell S.J., 1975, Nat 254, 578

Jahoda K., Markwardt C.B., Radeva Y., et al., 2006, ApJS 163, 401

Jahoda K., Swank J.H., Giles A.B., et al., 1996, In: Siegmund O.H., Gummin M.A. (eds.) Society of Photo-Optical Instrumentation Engineers (SPIE) Conference Series, Vol. 2808. Society of Photo-Optical Instrumentation Engineers (SPIE) Conference Series, p.59

Janot-Pacheco E., Ilovaisky S.A., Chevalier C., 1981, A & A 99, 274

Jansen F., Parmar A.N., 2001, In: H. Inoue & H. Kunieda (ed.) New Century of X-ray Astronomy, Vol. 251. Astronomical Society of the Pacific Conference Series, p.10

Jones C.A., Chetin T., Liller W., 1974, ApJ, Lett. 190, L1

Kaastra J.S., Mewe R., 1993, A&AS 97, 443

Kaper L., van der Meer A., Najarro F., 2006, A & A 457, 595

Katz J.I., 1976, ApJ 206, 910

Keller C., 1995, Cell Mole Life Sci 51, 710

Kelley R.L., Mitsuda K., Allen C.A., et al., 2007, PASJ 59, 77

Kendziorra E., Kretschmar P., Pan H.C., et al., 1994, A & A 291, L31

Kendziorra E., Mony B., Kretschmar P., et al., 1992, In: C. R. Shrader, N. Gehrels, & B. Dennis (ed.) NASA Conference Publication, Vol. 3137. NASA Conference Publication, p. 217

King A., 1995, In: W. H. G. Lewin, J. van Paradijs, & E. P. J. van den Heuvel (ed.) X-ray Binaries., p.419

Kiraly P., Meszaros P., 1988, ApJ 333, 719

Kirk J.G., Galloway D.J., 1981, MNRAS 195, 45P

Kirk J.G., Stoneham R.J., 1982, MNRAS 201, 1183

Kirsch M.G., Briel U.G., Burrows D., et al., 2005, In: Siegmund O.H.W. (ed.) Society of Photo-Optical Instrumentation Engineers (SPIE) Conference Series, Vol. 5898. Society of Photo-Optical Instrumentation Engineers (SPIE) Conference Series, p.22

Klochkov D., Santangelo A., Staubert R., Ferrigno C., 2008a, A & A 491, 833

Klochkov D., Santangelo A., Staubert R., Rothschild R.E., 2011, ArXiv e-prints

Klochkov D., Staubert R., Postnov K., et al., 2008b, A & A 482, 907

Knoll G.F., 2000, Radiation Detection and Measurment, Third Edition, John Wiley & Sons

Koh D.T., Bildsten L., Chakrabarty D., et al., 1997, ApJ 479, 933

Kohmura T., Kitamoto S., Torii K., 2001, ApJ 562, 943

Kokubun M., Makishima K., Takahashi T., et al., 2007, PASJ 59, 53

Kraus U., Blum S., Schulte J., et al., 1996, ApJ 467, 794

Kraus U., Nollert H.P., Ruder H., Riffert H., 1995, ApJ 450, 763

Kraus U., Zahn C., Weth C., Ruder H., 2003, ApJ 590, 424

Kretschmar P., 1996, Ph.D. thesis, Univ. of Tübingen

Kreykenbohm I., Coburn W., Wilms J., et al., 2002, A & A 395, 129

Kreykenbohm I., Kretschmar P., Wilms J., et al., 1999, A & A 341, 141

Kreykenbohm I., Mowlavi N., Produit N., et al., 2005, A & A 433, L45

Kreykenbohm I., Wilms J., Coburn W., et al., 2004, A & A 427, 975

Kreykenbohm I., Wilms J., Kretschmar P., et al., 2008, A & A 492, 511

Krzeminski W., 1974, ApJ, Lett. 192, L135

Kubota A., Done C., Davis S.W., et al., 2010, ApJ 714, 860

Kulkarni A.K., Romanova M.M., 2008, MNRAS 386, 673

La Barbera A., Burderi L., Di Salvo T., et al., 2001, ApJ 553, 375

La Barbera A., Santangelo A., Orlandini M., Segreto A., 2003, A & A 400, 993

La Barbera A., Segreto A., Santangelo A., et al., 2005, A & A 438, 617

Lada C.J., 2006, ApJ, Lett. 640, L63

Lai D., 2001, Reviews of Modern Physics 73, 629

Lamb F.K., Pethick C.J., Pines D., 1973, ApJ 184, 271

Lamb R.C., Markert T.H., Hartman R.C., et al., 1980, ApJ 239, 651

Latal H.G., 1986, ApJ 309, 372

Leahy D.A., 1991, MNRAS 250, 310

Leahy D.A., 2002, A & A 391, 219

Leahy D.A., Kostka M., 2008, MNRAS 384, 747

Lemaitre G., Vallarta M.S., 1933, Physical Review 43, 87

Lewin W.H.G., McClintock J.E., Ryckman S.G., Smith W.B., 1971, ApJ, Lett. 166, L69

Leyder J., Walter R., Lubinski P., 2009, The Astronomer's Telegram 1949, 1

Maisack M., Grove J.E., Kendziorra E., et al., 1997, A & A 325, 212

Makishima K., Mihara T., Ishida M., et al., 1990, ApJ, Lett. 365, L59

Makishima K., Mihara T., Nagase F., Tanaka Y., 1999, ApJ 525, 978

Mangano V., 2009, The Astronomer's Telegram 1896, 1

Mangano V., Baumgartner W.H., Gehrels N., et al., 2009, GRB Coordinates Network 8777, 1

Marshall F.E., Boldt E.A., Holt S.S., et al., 1980, apj 235, 4

Matsumoto H., Nakajima H., Yamaguchi H., et al., 2006, In: Society of Photo-Optical Instrumentation Engineers, Proc. SPIE, Vol. 6266. Presented at the Society of Photo-Optical Instrumentation Engineers (SPIE) Conference

McBride V.A., Wilms J., Coe M.J., et al., 2006, A & A 451, 267

McClintock J.E., Ricker G.R., Lewin W.H.G., 1971, ApJ, Lett. 166, L73

Mészáros P., 1992, High-energy radiation from magnetized neutron stars., University of Chicago Press, Chicago, IL (USA)

Meszaros P., Meyer F., Pringle J.E., 1977, Nat 268, 420

Meszaros P., Nagel W., 1985a, ApJ 298, 147

Meszaros P., Nagel W., 1985b, ApJ 299, 138

Mihara T., 1995, Ph.D. thesis, Univ. of Tokyo

Mihara T., Makishima K., Kamijo S., et al., 1991, ApJ, Lett. 379, L61

Mihara T., Makishima K., Ohashi T., et al., 1990, Nat 346, 250

Mihara T., Terada Y., Nakajima M., et al., 2007, Prog. Theor. Phys. Suppl. 169, 191

Miralda-Escude J., Paczynski B., Haensel P., 1990, ApJ 362, 572

Mitsuda K., Bautz M., Inoue H., et al., 2007, PASJ 59, 1

Motch C., Pakull M.W., Janot-Pacheco E., Mouchet M., 1988, A & A 201, 63

Mowlavi N., Kreykenbohm I., Shaw S.E., et al., 2006, A & A 451, 187

Mukherjee U., Paul B., 2004, A & A 427, 567

Nagase F., Corbet R.H.D., Day C.S.R., et al., 1992, ApJ 396, 147

Nagel W., 1981a, ApJ 251, 288

Nagel W., 1981b, ApJ 251, 278

Nakajima M., Mihara T., Makishima K., 2010, ApJ 710, 1755

Nakajima M., Mihara T., Makishima K., Niko H., 2006, ApJ 646, 1125

Orlandini M., dal Fiume D., Frontera F., et al., 2000, Advances in Space Research 25, 417

Orlandini M., Fiume D.D., Frontera F., et al., 1998, ApJ, Lett. 500, L163

Ostriker J.P., Gunn J.E., 1969, ApJ 157, 1395

Pacini F., 1967, Nat 216, 567

Parkes G.E., Culhane J.L., Mason K.O., Murdin P.G., 1980, MNRAS 191, 547

Parmar A.N., Oosterbroek T., Sidoli L., et al., 2001, A & A 380, 490

Parmar A.N., White N.E., Stella L., 1989a, ApJ 338, 373

Parmar A.N., White N.E., Stella L., et al., 1989b, ApJ 338, 359

Petterson J.A., 1978, ApJ 224, 625

Popham R., Sunyaev R., 2001, ApJ 547, 355

Porter J.M., Rivinius T., 2003, PASP 115, 1153

Postnov K.A., Yungelson L.R., 2006, Living Reviews in Relativity 9, 6

Pottschmidt K., 2002, Ph.D. thesis, Univ. of Tübingen

Pottschmidt K., Kreykenbohm I., Wilms J., et al., 2005, ApJ, Lett. 634, L97

Pottschmidt K., Rothschild R.E., Gasaway T., et al., 2006, In: AAS/High Energy Astrophysics Division #9, Vol. 38. Bulletin of the American Astronomical Society, p.384

Pravdo S.H., Day C.S.R., Angelini L., et al., 1995, ApJ 454, 872

Pravdo S.H., Ghosh P., 2001, ApJ 554, 383

Pringle J.E., Rees M.J., 1972, A & A 21, 1

Raichur H., Paul B., 2010, MNRAS 401, 1532

Ray A., 2004, ArXiv Astrophysics e-prints

Reig P., Fabregat J., Coe M.J., 1997, A & A 322, 193

Reynolds A.P., Parmar A.N., White N.E., 1993, ApJ 414, 302

Reynolds C.S., Nowak M.A., 2003, Phys. Rep. 377, 389

Ritz S., 2007, In: S. Ritz, P. Michelson, & C. A. Meegan (ed.) The First GLAST Symposium, Vol. 921. American Institute of Physics Conference Series, p.3

Rivers E., Markowitz A., Pottschmidt K., et al., 2010, ApJ 709, 179

Rodes-Roca J.J., Torrejón J.M., Kreykenbohm I., et al., 2009, A & A 508, 395

Rosenberg H., 1910, Astronomische Nachrichten 186, 71

Rothschild R.E., Blanco P.R., Gruber D.E., et al., 1998, ApJ 496, 538

Rothschild R.E., Wilms J., Tomsick J., et al., 2006, ApJ 641, 801

Rutledge R.E., Bildsten L., Brown E.F., et al., 2007, ApJ 658, 514

Santangelo A., del Sordo S., Segreto A., et al., 1998, A & A 340, L55

Santangelo A., Segreto A., Giarrusso S., et al., 1999, ApJ, Lett. 523, L85

Sasaki M., Klochkov D., Kraus U., et al., 2010, A & A 517, A8

Schandl S., Meyer F., 1994, A & A 289, 149

Schatzman E.L., Praderie F., King A.R., 1993, The Stars, Springer-Verlag Berlin Heidelberg

Schönherr G., 2007, Ph.D. thesis, Univ. of Tübingen

Schönherr G., Wilms J., Kretschmar P., et al., 2007, A & A 472, 353

Schreier E., Levinson R., Gursky H., et al., 1972, ApJ, Lett. 172, L79+

Schwarm F., 2010, *Master's thesis*, Univ. of Erlangen-Nurnberg

Shakura N., Postnov K., Kochetkova A., Hjalmarsdotter L., 2011, ArXiv e-prints

Shakura N.I., 1973, SvA 16, 756

Shapiro S.L., Lightman A.P., Eardley D.M., 1976, ApJ 204, 187

Shapiro S.L., Salpeter E.E., 1975, ApJ 198, 671

Shrader C.R., Sutaria F.K., Singh K.P., Macomb D.J., 1999, ApJ 512, 920

Skinner G.K., Bedford D.K., Elsner R.F., et al., 1982, Nat 297, 568

Soderberg A.M., Berger E., Page K.L., et al., 2008, Nat 453, 469

Soong Y., Gruber D.E., Peterson L.E., Rothschild R.E., 1990, ApJ 348, 641

Srinivasan G., 1989, A & A Rev. 1, 209

Srinivasan G., Bhattacharya D., Muslimov A.G., Tsygan A.J., 1990, Current Science 59, 31

Starrfield S., Sparks W.M., Truran J.W., 1985, ApJ 291, 136

Staubert R., Pottschmidt K., Doroshenko V., et al., 2010, A & A

Staubert R., Shakura N.I., Postnov K., et al., 2007, A & A 465, L25

Stevens I.R., 1988, MNRAS 232, 199

Suchy S., Fürst F., Pottschmidt K., et al., 2011a, ApJ, accepted

Suchy S., Pottschmidt K., Rothschild R.E., et al., 2011b, ApJ 733, 15

Suchy S., Pottschmidt K., Wilms J., et al., 2008, ApJ 675, 1487

Sunyaev R.A., Shakura N.I., 1986, Soviet Astronomy Letters 12, 117

Takahashi T., Abe K., Endo M., et al., 2007, PASJ 59, 35

Takeshima T., Dotani T., Mitsuda K., Nagase F., 1991, PASJ 43, L43

Tanaka Y., 1986, In: Radiation Hydrodynamics in Stars and Compact Objects, ed. D. Mihalas & K.-H. A. Winkler, IAU Colloq. series 89, Vol. 255. Lecture Notes in Physics, Berlin Springer Verlag, p. 198

Taylor J.H., 1981, In: W. Sieber & R. Wielebinski (ed.) Pulsars: 13 Years of Research on Neutron Stars, Vol. 95. IAU Symposium, p.361

Thompson T.W.J., Rothschild R.E., 2009, ApJ 691, 1744

Titarchuk L., 1994, ApJ 434, 570

Titarchuk L., Hua X., 1995, ApJ 452, 226

Titarchuk L., Lyubarskij Y., 1995, ApJ 450, 876

Tjemkes S.A., van Paradijs J., Zuiderwijk E.J., 1986, A & A 154, 77

Torrejón J.M., Kreykenbohm I., Orr A., et al., 2004, A & A 423, 301

Trümper J., 1982, Advances in Space Research 2, 241

Trümper J., Pietsch W., Reppin C., et al., 1978, ApJ, Lett. 219, L105

Tsunemi H., Kitamoto S., Tamura K., 1996, ApJ 456, 316

Tsygankov S.S., Lutovinov A.A., Churazov E.M., Sunyaev R.A., 2006, MNRAS 371, 19

Tsygankov S.S., Lutovinov A.A., Churazov E.M., Sunyaev R.A., 2007, Astron. Lett. 33, 368

Urpin V., Geppert U., 1995, MNRAS 275, 1117

Verner D.A., Ferland G.J., Korista K.T., Yakovlev D.G., 1996, ApJ 465, 487

Villada M., Giovannelli F., Polcaro V.F., 1992, A & A 259, L1

Villada M., Rossi C., Polcaro V.F., Giovannelli F., 1999, A & A 344, 277

Watanabe S., Sako M., Ishida M., et al., 2003, ApJ, Lett. 597, L37

Weisskopf M.C., Tananbaum H.D., Van Speybroeck L.P., O'Dell S.L., 2000, In: J. E. Truemper & B. Aschenbach (ed.) Society of Photo-Optical Instrumentation Engineers (SPIE) Conference Series, Vol. 4012. Presented at the Society of Photo-Optical Instrumentation Engineers (SPIE) Conference, p.2

Wheaton W.A., Doty J.P., Primini F.A., et al., 1979, Nat 282, 240

White N.E., Kallman T.R., Swank J.H., 1983, ApJ 269, 264

White N.E., Mason K.O., Huckle H.E., et al., 1976, ApJ, Lett. 209, L119

White N.E., Mason K.O., Sanford P.W., 1978a, MNRAS 184, 67P

White N.E., Parkes G.E., Sanford P.W., et al., 1978b, Nat 274, 664

Wilms J., 1998, Ph.D. thesis, Univ. of Tübingen

Wilms J., Allen A., McCray R., 2000, ApJ 542, 914

Wilms J., Nowak M.A., Pottschmidt K., et al., 2006, A & A 447, 245

Winkler C., Courvoisier T.J.L., Di Cocco G., et al., 2003, A & A 411, L1

Wojdowski P.S., Liedahl D.A., Sako M., 2001, ApJ 547, 973

Wojdowski P.S., Liedahl D.A., Sako M., et al., 2003, ApJ 582, 959

Wolter H., 1952a, Annalen der Physik 445, 94

Wolter H., 1952b, Annalen der Physik 445, 286

Yahel R.Z., 1977, Ap&SS 51, 135

Yamaguchi H., Nakajima H., Koyama K., et al., 2006, In: Society of Photo-Optical Instrumentation Engineers (SPIE) Conference Series, Vol. 6266. Society of Photo-Optical Instrumentation Engineers (SPIE) Conference Series

Yamamoto T., Sugizaki M., Mihara T., et al., 2011, ArXiv e-prints

Zel'Dovich Y.B., Shakura N.I., 1969, SvA 13, 175

Zhao P., Jerius D.H., Edgar R.J., et al., 2004, In: K. A. Flanagan & O. H. W. Siegmund (ed.) Society of Photo-Optical Instrumentation Engineers (SPIE) Conference Series, Vol. 5165. Society of Photo-Optical Instrumentation Engineers (SPIE) Conference Series, p.482